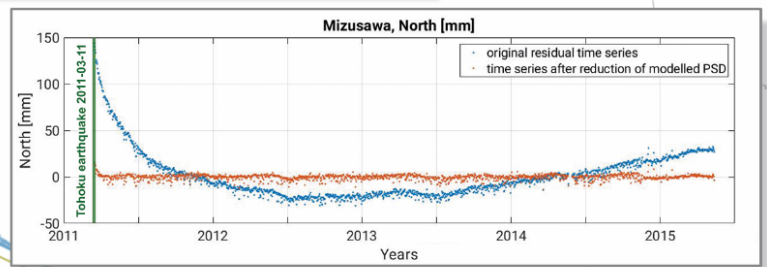
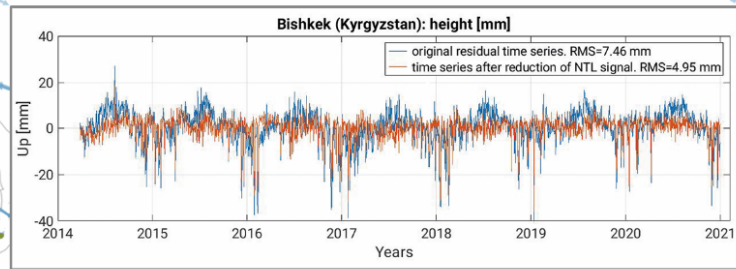
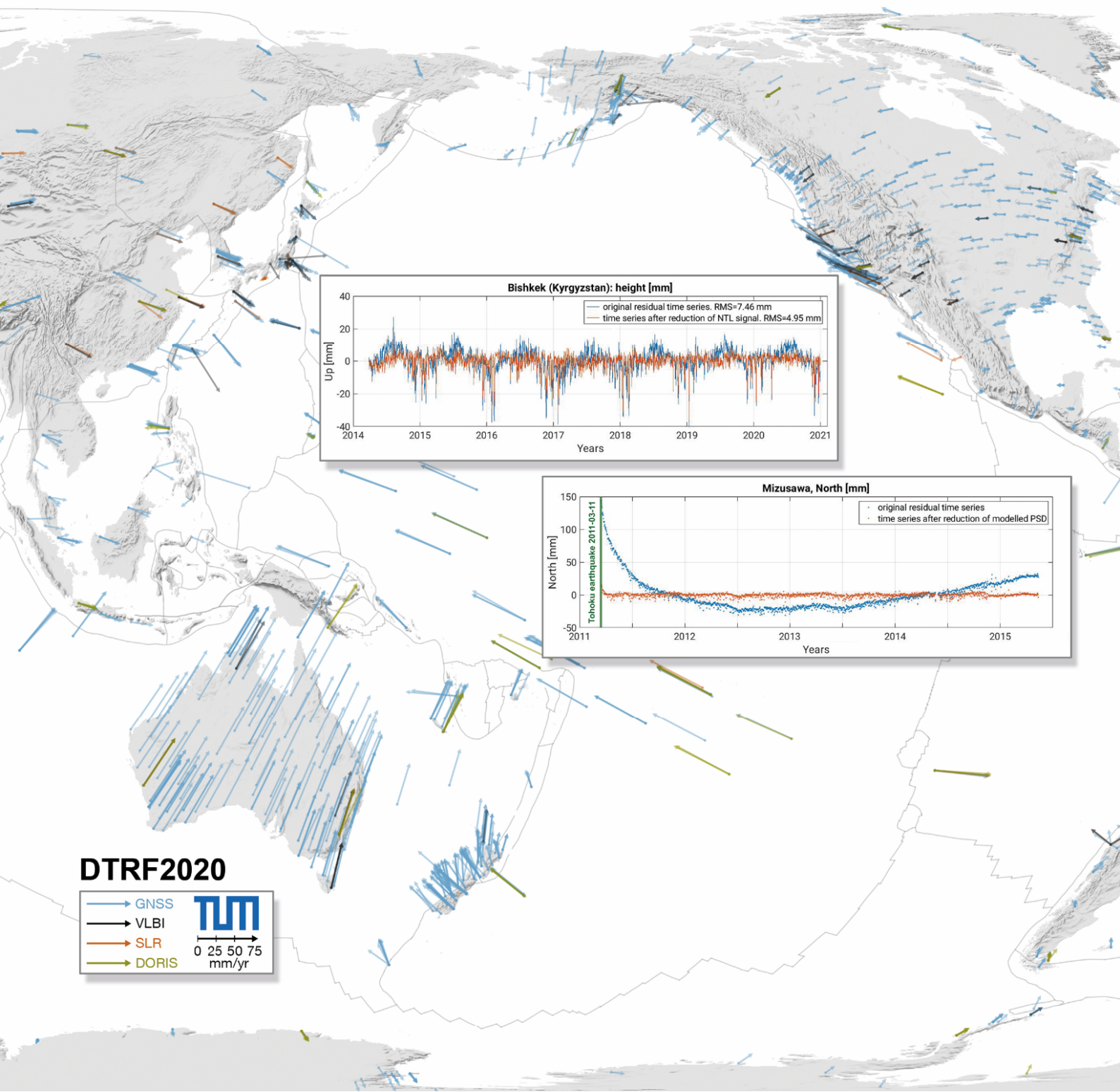
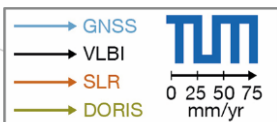


Annual Report 2022

Deutsches Geodätisches Forschungsinstitut
der Technischen Universität München
(DGFI-TUM)



DTRF2020



Front cover: DTRF2020 – DGFI-TUM’s new realization of the International Terrestrial Reference System (ITRS)

DGFI-TUM has been one of the three ITRS Combination Centers of the International Earth Rotation and Reference Systems Service (IERS) since 2001 and in this role is responsible for the realization of the ITRS alongside the IGN (France) and JPL/NASA (USA). As the fundamental coordinate system of the Earth, the ITRS provides the framework for referencing geodetic and astronomical observations. A highly accurate realization of the coordinate system, the so-called *Reference Frame*, is of paramount importance for various socially relevant applications. These include navigation, positioning and surveying, the realization of height systems and precise time systems, the calculation of spacecraft and satellite orbits, and the operation of early warning systems. Accurate and up-to-date reference frames also form the backbone for the scientific exploration of the Earth system by providing the reference for monitoring dynamic processes and effects of climate change, such as ice melt or sea level rise.

The DTRF2020 is the latest ITRS realization of DGFI-TUM. It was calculated in 2022 from the combination of up to 41 years of observation data from the four geodetic space techniques VLBI (Very Long Baseline Interferometry), SLR (Satellite Laser Ranging), GNSS (Global Navigation Satellite Systems), and DORIS (Doppler Orbitography and Radiopositioning Integrated by Satellite), pre-processed and analyzed in a major international effort coordinated by the Scientific Services of the International Association of Geodesy (IAG). For a global network of 1829 stations, the DTRF2020 contains high-precision coordinates and coordinate changes (indicated as colored arrows in the figure).

It is the only ITRS realization that accounts for station displacements caused by atmospheric, hydrologic, and oceanic mass redistributions (so-called Non-Tidal Loading, NTL). The upper panel shows the height variation of the station Bishkek (Kyrgyzstan) from which a clear seasonal NTL effect could be reduced using geophysical model data. Furthermore, for the first time, the DTRF2020 also considers post-seismic deformation of stations affected by earthquakes as visible in the lower panel for the station Mizusawa (Japan). There, a strong non-linear post-seismic signal was modeled by logarithmic and exponential functions and reduced from the North-component of the station motion.

The activities of the ITRS Combination Center are embedded in the scientific work of DGFI-TUM’s Research Area *Reference Systems*, see Section 1.4 of this report.

Technische Universität München
TUM School of Engineering and Design
Department Aerospace and Geodesy
Deutsches Geodätisches Forschungsinstitut (DGFI-TUM)

Arcisstr. 21
D - 80333 München

www.dgfi.tum.de

Contents

Preface	1
1 Research Area Reference Systems	7
1.1 Analysis of Space-Based Microwave Observations	10
1.2 Analysis of Satellite Laser Ranging Observations	14
1.3 Determination of Satellite Orbits	16
1.4 Determination of Reference Frames	19
2 Research Area Satellite Altimetry	30
2.1 Multi-Mission Analysis	30
2.2 Sea Surface	33
2.3 Inland Altimetry	47
3 Cross-Cutting Research Topics	52
3.1 Atmosphere	53
3.2 Regional Gravity Field	67
3.3 Standards and Conventions	73
4 Scientific Transfer	77
4.1 Functions in Scientific Bodies	77
4.2 Publications	82
4.3 Presentations	85
4.4 Participation in Meetings, Symposia, Conferences	93
4.5 Guests	97
4.6 Internet Portals	98
5 Projects	102
6 Personnel	103
6.1 Lectures and Courses at Universities	103
6.2 Academic Program Coordination and Study Advice	103
6.3 Lectures at Seminars, Schools, and Public Relations	104
6.4 Thesis Supervision	104
6.5 Conferral of Doctorates	105
6.6 Conferral of Venia Legendi	105
6.7 International Research Stays	105
6.8 Awards	106

Preface

The Institute

The Deutsches Geodätisches Forschungsinstitut (DGFI-TUM) is a research institute of the Technical University of Munich (TUM). It is part of the Chair of Geodetic Geodynamics within the Department of Aerospace and Geodesy of the TUM School of Engineering and Design.

DGFI-TUM conducts fundamental research in Space Geodesy with the goal of precisely measuring and investigating the geometric and physical properties of the Earth system and their changes over time. In close international and interdisciplinary cooperation, DGFI-TUM analyzes and combines observation data from all relevant geodetic space observing systems and complementary data sources. A central aspect of the institute's research has always been the precise determination of the geometric figure of the Earth and its temporal changes. For the solid Earth, this involves in particular the realization of terrestrial reference and height systems on a global and regional scale as well as of the celestial reference system. With respect to water surfaces, a focus of DGFI-TUM is on the precise determination of the changing sea level, the surface dynamics of the oceans and the water levels of inland waters using satellite altimetry.

DGFI-TUM is involved in the work of the United Nations Global Climate Observing System (GCOS) through its participation in major international research programs, including those of ESA and the Copernicus program, and actively contributes to the determination of the Essential Climate Variables (ECVs) through its research work. It is also a key player in the Global Geodetic Observing System (GGOS) of the International Association of Geodesy (IAG). The strategic orientation of DGFI-TUM is reflected in its organization into the two research areas *Reference Systems* and *Satellite Altimetry* (Fig. 1). The research areas are complemented by three overarching research topics that include the study of the state and dynamics of the atmosphere (with emphasis on ionospheric disturbances and space weather impacts), the determination of high-resolution regional gravity fields, and the enhancement of consistency in the analysis of geodetic data by establishing uniform standards and conventions in an international context.

As part of the Research Group Satellite Geodesy (Forschungsgruppe Satellitengeodäsie, FGS), DGFI-TUM is involved in scientific data processing of the Geodetic Observatories Wettzell (Germany) and AGGO (Argentina). In addition, it operates GNSS stations distributed worldwide.

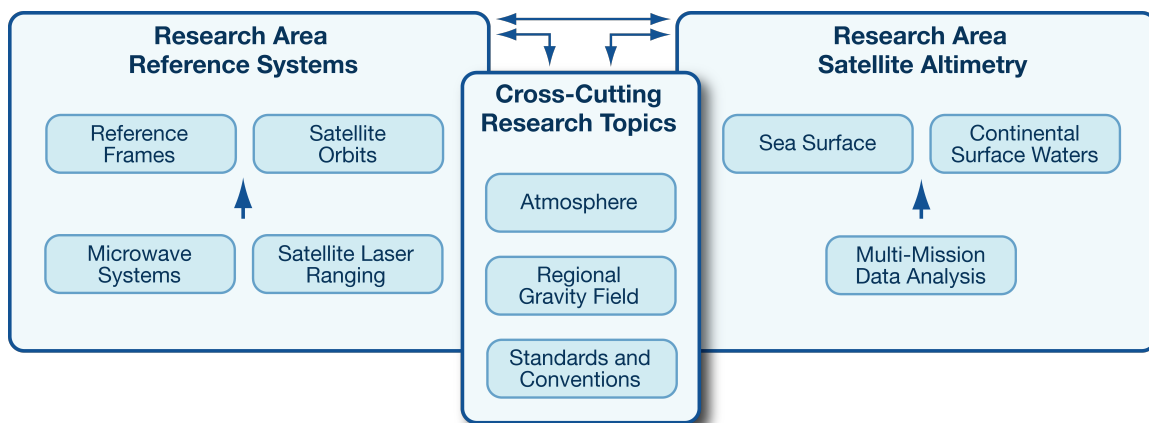


Figure 1: Research Areas of DGFI-TUM

National and international involvement

The institute looks back on a 70-year history. In 1952, it was established by the German Geodetic Commission (Deutsche Geodätische Kommission, DGK) as an independent research institution at the Bavarian Academy of Sciences and Humanities (BAdW) in Munich, and since 2015 it has been part of the TUM. Since its foundation, it has been continuously involved in significant national and international coordinated geodetic research activities and intensively networked with renowned research institutions around the world. The research direction of DGFI, which has shaped the institute, was and is the advancement of mathematical and physical geodesy. In the course of the institute's history, this has included geometric methods of astronomical geodesy, land surveying and satellite triangulation as well as dynamic methods of gravimetry and satellite geodesy.

Many of the research projects carried out at DGFI were of great importance for the scientific progress of geodesy. In the first decades after its foundation, geodetic-astronomical observations, triangulation and height measurements were among the essential works, including the IAG project for the readjustment of the European triangulation and the adjustment of the European levelling network. Later, the focus shifted to the geodetic use of artificial Earth satellites. DGFI was involved in the first worldwide network of satellite triangulation and played a leading role in the development of dynamic methods of satellite geodesy for the precise determination of satellite orbits, the Earth's gravity field, and point positions. With the further development of modern space geodetic techniques and the expansion of the worldwide geodetic infrastructure in the 1980s and 1990s, the expansion of the Geodetic Observatory in Wettzell, and in the course of DGFI's participation in the DFG Collaborative Research Center *Satellite Geodesy* (SFB 78), the further development of theories and methods for the definition and realization of terrestrial reference systems became a focus of the institute. Since satellite altimetry became operational as a geodetic observation technique in the mid-1990s, the observation and scientific analysis of water surface dynamics has complemented the research program.

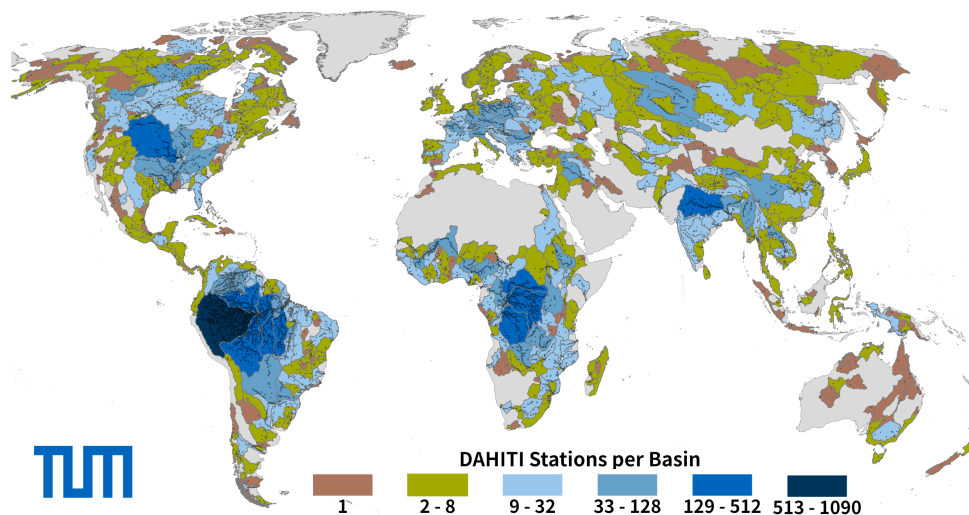
DGFI-TUM is committed in central positions in international scientific organizations, especially in the framework of the International Union of Geodesy and Geophysics (IUGG), the International Astronomical Union (IAU) and the International Association of Geodesy (IAG) (see Section 4.2). For many years, the Institute has been an important pillar of the IAG's Global Geodetic Observing System (GGOS). GGOS advocates for the implementation of geodetic infrastructures and analysis capabilities necessary for Earth system monitoring and global change research, and coordinates the generation of high quality scientific data products under predefined standards and conventions. DGFI-TUM provides the current GGOS Vice President, chairs one of the two GGOS Bureaus (Bureau of Products and Standards), and leads two of the three GGOS Focus Areas (FA Unified Height System; FA Geodetic Space Weather Research). In addition, the institute recognizes the outstanding importance of the IAG Scientific Services that form the backbone of the national and international spatial data infrastructure. Within this framework, DGFI-TUM operates data centers, analysis centers, and research centers. It performs leading and supporting functions in IAG commissions, projects, working and study groups and thus contributes to shaping the future direction of international geodetic research.

The institute participates in research programs of the European Union (EU) and the European Space Agency (ESA) and cooperates in United Nations (UN) activities. In this regard, DGFI-TUM is involved in the implementation of the UN resolution for a Global Geodetic Reference Frame (GGRF) and provides an IAG representative to the UN Committee of Experts on Global Geospatial Information Management (UN-GGIM) Working Group for the GGRF. Through its research, DGFI-TUM directly contributes to the monitoring and provision of Essential Climate Variables (ECVs) and thus supports the goals of the UN Global Climate Observing System (GCOS).

Research highlights of particular scientific and public interest

During the year 2022, several scientific results gained broad attention in the scientific community and in the public. The following activities and publications can be highlighted:

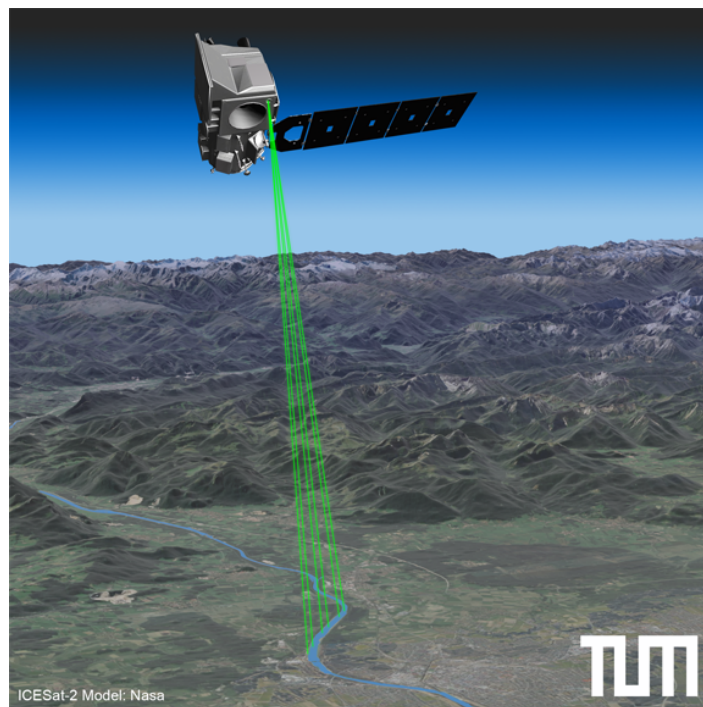
- DTRF2020: New realization of the International Terrestrial Reference System ITRS (cover page)** : As one of the three ITRS Combination Centers of the International Earth Rotation and Reference Systems Service (IERS), DGFI-TUM is responsible for contributing to the realization of the Earth-fixed coordinate system ITRS through an independent solution of the International Terrestrial Reference Frame (ITRF). DGFI-TUM's latest ITRF solution is the DTRF2020 computed in 2022, which contains highly precise coordinates and coordinate changes for a global network of 1829 stations. The DTRF2020 was combined from VLBI, SLR, GNSS, and DORIS observations from a period between 1980 and the end of 2020. It has unique features: The DTRF2020 is the only combined secular terrestrial reference frame that accounts for station displacements caused by atmospheric, hydrologic, and oceanic mass redistributions, and it is the first solution whose scale is realized from combining GNSS with VLBI data. Details are provided on the website of the ITRS Combination Centers at DGFI-TUM (dtrf.dgfi.tum.de) and in Section 1.4 of this report.
- Milestone for DAHITI:** For meanwhile 10,000 targets worldwide DGFI-TUM's Database for Hydrological Time Series of Inland Waters (DAHITI, dahiti.dgfi.tum.de) provides free hydrological information. For rivers, lakes, reservoirs and wetlands, parameters such as water level, surface extent, storage change and discharge are available from satellite data. With several thousand registered users and more than two hundred thousand downloads in recent years, DAHITI is a widely used data source for numerous applications in science and practice. GCOS lists DAHITI as an openly accessible data source for the ECV Lakes, through which time series of water level and surface extent are currently available for more than 1400 lakes and reservoirs. See Sections 2.3 and 4.6.



- Geocentric realization of regional Epoch Reference Frames:** Monitoring geophysical processes in the Earth system requires relating observations from different sources to a common reference. This reference is established by precise coordinate reference frames. Thereby, it is essential that the geodetic datum of the reference frame, i.e., its origin (defined at the Earth's center of mass), scale, and orientation, conform at all times to their conventional definition provided by the International Terrestrial Reference System (ITRS). Given the variable and inhomogeneous distribution and performance of observing stations of various geodetic space techniques, DGFI-TUM has developed a strategy to implement a stable

geocentric regional Epoch Reference Frame on a week-by-week, low-latency basis. Details can be found in the article *combination strategy for geocentric realization of regional epoch reference frames* (Journal of Geophysical Research, 2022, doi:[10.1029/2021JB023880](https://doi.org/10.1029/2021JB023880)) and in Section 1.4.

- **ICESat-2 River Surface Slopes (IRIS):** Estimation of river discharge or interpolation of water levels to specific positions requires knowledge of the water surface slope. DGFI-TUM has developed a method for determining time-varying and average water surface slopes (at reach scale) based on ICESat-2 laser altimeter observations. The method was validated using in situ data from 815 different river reaches in Europe and North America. It was then applied globally to create the global reach-scale water surface dataset IRIS, which can be easily applied together with the with the SWOT Mission River Database (SWORD). IRIS can be used to study river dynamics, estimate river discharge, and correct water level time series from satellite altimetry for shifting ground tracks. Details are provided in the articles *ICESat-2 river surface slope (IRIS): A global reach-scale water surface slope dataset* (Nature Scientific Data, 2023, doi:[10.1038/s41597-023-02215-x](https://doi.org/10.1038/s41597-023-02215-x)) and *ICESat-2 based river surface slope and its impact on water level time series from satellite altimetry* (Water Resources Research, 2022, doi:[10.1029/2022WR032842](https://doi.org/10.1029/2022WR032842)); see also Section 2.3.



- **Thin ice detection with Cryosat-2:** Dwindling sea ice and an increasing number of open water areas have a significant impact on sea ice dynamics in the Arctic Ocean. In addition to open water, areas that are partially frozen and covered by a thin layer of ice play an important role in the heat exchange between ocean and atmosphere and must be taken into account in climate modeling and predictions. DGFI-TUM and the Alfred Wegener Institute (AWI), Germany, have jointly developed a classification method to detect thin ice from space based on SAR altimeter radar data from ESA's Cryosat-2 mission. and compared the results are compared with MODIS thermal imagery and Sentinel-1 radar images. The new method also supports the development of improved waveform retracking algorithms that provide more reliable estimates of sea ice freeboard and sea level in the polar oceans. Details are provided in the article *Monitoring Arctic thin ice: a comparison between CryoSat-2 SAR altimetry data and MODIS thermal-infrared imagery* (The Cryosphere, 2023, doi:[10.5194/tc-17-809-2023](https://doi.org/10.5194/tc-17-809-2023)) and in Section 2.2.

- **Novel algorithm for regional gravity field modeling to support the IHRS:** A current major goal in geodesy is the realization of the International Height Reference System (IHRS). The IHRS has been developed in recent years in close international cooperation within the IAG under the lead of DGFI-TUM. It is based on a high-resolution geoid refinement. To ensure the highest possible precision in geoid determination, different types of gravity observations have to be optimally combined. DGFI-TUM has developed a novel method for the spectral combination of different observation types that are sensitive to different spectral bands. This is particularly advantageous when high-resolution terrestrial data do not have a large coverage over the study area. Methodology and results are documented in the article *Combination of different observation types through a multi-resolution representation of the regional gravity field using the pyramid algorithm and parameter estimation* (Journal of Geodesy, 2022, doi:[10.1007/s00190-022-01670-5](https://doi.org/10.1007/s00190-022-01670-5)); see Section 3.2.
- **Young researchers' prizes awarded to two doctoral candidates:** The *Young Scientist Award of the International Union of Radio Science (URSI)*, which recognizes international young scientists for innovative contributions and discoveries in multidisciplinary research related to URSI, was presented to **Randa Natras**. She received the award for developing a machine learning ensemble approach for ionosphere and space weather forecasting with uncertainty quantification. The award was presented at the 3rd URSI Atlantic / Asia-Pacific Radio Science Meeting 2022, held in Gran Canaria, Spain. **Julius Oelsmann** received the *2022 Outstanding Student and PhD candidate Presentation (OSPP) Award* of the European Geosciences Union (EGU) Division Climate: Past, Present and Future. He was awarded for his poster presentation 'The impact of continuous space and time-resolving vertical land motion on relative sea level change' at the EGU General Assembly 2022 in Vienna, Austria.

1 Research Area Reference Systems

Reference systems on Earth and in space form the fundamental framework for referencing geodetic and astronomical observations. Highly accurate realizations of these systems, the so-called reference frames, are of utmost importance for positioning and navigation on Earth and in the solar system as well as for the measurement of time. Theoretical and practical aspects of reference systems and their realization have been a central topic of DGFI-TUM for decades.

Research in this area is based on the geodetic space observation techniques Very Long Baseline Interferometry (VLBI), Satellite Laser Ranging (SLR), Global Navigation Satellite Systems (GNSS), and Doppler Orbitography and Radiopositioning Integrated by Satellite (DORIS). The scientific focus is on the development of refined analysis strategies and models for these observation techniques, as well as on the development of advanced methods for combining them. Key scientific outputs of DGFI-TUM include global and regional realizations of three-dimensional geodetic reference systems obtained from combining the techniques. Research activities also comprise the consistent realization of terrestrial and celestial reference systems including Earth orientation parameters, the realization of vertical reference systems, and the determination of precise satellite orbits.

An important prerequisite for the research on reference systems is the long-standing involvement of DGFI-TUM in international scientific organizations, in particular in the International Association of Geodesy (IAG) and the International Astronomical Union (IAU). The institute operates, mostly on the basis of long-term commitments, Operation and Data Centers, Analysis Centers and Combination Centers (Table 1.1).

Table 1.1: Long-term commitments of DGFI-TUM in international organizations related to the Research Area Reference Systems.

Organization	DGFI-TUM Commitments
International Earth Rotation and Reference Systems Service (IERS)	International Terrestrial Reference System (ITRS) Combination Center
International VLBI Service for Geodesy and Astrometry (IVS)	Analysis Center (AC), Combination Center (jointly with BKG)
International Laser Ranging Service (ILRS)	EUROLAS Data Center (EDC), Analysis Center (AC), Operations Center (OC)
International GNSS Service (IGS)	Regional Network Associate Analysis Center for SIRGAS (RNAAC-SIR)
International DORIS Service (IDS)	Associate Analysis Center (AAC)

In 2022, DGFI-TUM was significantly involved in the establishment of the **DFG Research Unit ‘Clock Metrology: A Novel Approach to TIME in Geodesy’**. The new Research Unit aims to improve geodetic reference frames by introducing time coherence as a new tie between geodetic space techniques to minimize systematic errors. DGFI-TUM will conduct the projects P7 (jointly with the Geodetic Observatory Wettzell) ‘The application of time in closure as a novel strategy towards error-free space-geodetic observations’ and P9 (jointly with GFZ Potsdam) ‘Novel clock technologies for combination on ground and in space: operation and simulation’.

The approval of the ESA mission 'GENESIS: co-location of geodetic techniques in space' by the ESA Council at Ministerial level in November 2022 marked another important milestone. Through carefully calibrated 'space-ties' the mission will allow for a significantly improved combination of geodetic space techniques. Details on the major impact this mission will have on future research can be seen in the white paper prepared with DGFI-TUM participation¹.

Enhancement of the DOGS software

As a fundamental backbone for the research in this area and the international contributions of DGFI-TUM, the institute operates and continuously expands its analysis and combination software DOGS (DGFI Orbit and Geodetic parameter estimation Software). In 2022, the three libraries DOGS-OC (Orbit Computation), DOGS-RI (Radio Interferometry) and DOGS-CS (Combination and Solution) were further developed. The following sections give an overview of improvements and new functions.

DOGS Orbit Computation (DOGS-OC): DOGS-OC is used for (i) the analysis of SLR and DORIS observations, (ii) the determination of precise (fully dynamic and reduced dynamic) orbits of near-Earth orbiting satellites, (iii) the simulation of modified/extended ground and space segments of SLR and DORIS, and (iv) the generation of normal equation (NEQ) systems for further processing with DOGS-CS (e.g., inversion to obtain a solution or combination with other NEQs). Next to the various research activities also the routine tasks as ILRS AC rely on DOGS-OC. In 2022, the following updates, improvements and new models have been implemented:

- new Earth's time-variable gravity field model EIGEN-GRGS.RL04.MEAN-FIELD²
- new ocean tide models FES2014³ and EOT20⁴,
- refined thermospheric density model NRLMSIS2.0⁵,
- handling and smoothing of observed geomagnetic storm and solar flux indices⁶,
- new Consolidated Laser Ranging Data (CRDv2, since 2022-08-01) format 2.0 for SLR observations (e.g., for full-rate data, normal points, calibration records, metadata),
- new Consolidated Prediction Format (CPFv2, since 2022-03-01) for orbit predictions
- station-dependent SLR measurement correction model for TOPEX/Poseidon,⁷
- improved computation of partial derivatives of DORIS station coordinates.

Numerous programmes in the DOGS-OC environment have been updated. Now the latest ITRS realizations ITRF2020 and DTRF2020 (Sect. 1.4) can already be used in the analysis of SLR and DORIS observations, including the respective corrections for periodic variations (ITRF2020), non-tidal loading (DTRF2020) and post-seismic deformation (both). Furthermore, the software package for the comparison of satellite orbits given on different time scales and in different reference frames has been further developed (Sect. 1.3).

¹Delva P., Altamimi Z., Blazquez A., Bloßfeld M., et al. (2023): *GENESIS: co-location of geodetic techniques in space*. Earth Planets Space, doi:[10.1186/s40623-022-01752-w](https://doi.org/10.1186/s40623-022-01752-w)

²Lemoine J.-M. et al. (2019): *CNES/GRGS RL04 Earth gravity field models, from GRACE and SLR data*. GFZ Data Services, doi:[10.5880/ICGEM.2019.010](https://doi.org/10.5880/ICGEM.2019.010)

³Lyard F. et al. (2021): *FES2014 global ocean tide atlas: design and performance*. Ocean Science, doi:[10.5194/os-17-615-2021](https://doi.org/10.5194/os-17-615-2021)

⁴Hart-Davis M.G., Piccioni G., Dettmering D., Schwatke C., Passaro M., Seitz F. (2021): *EOT20: a global ocean tide model from multi-mission satellite altimetry*. Earth System Science Data, doi:[10.5194/essd-13-3869-2021](https://doi.org/10.5194/essd-13-3869-2021)

⁵Emmert J.T. et al. (2021): *NRLMSIS 2.0: A Whole-Atmosphere Empirical Model of Temperature and Neutral Species Densities*. Earth and Space Science, doi:[10.1029/2020EA001321](https://doi.org/10.1029/2020EA001321)

⁶Matzka J. et al. (2021): *The Geomagnetic Kp Index and derived indices of geomagnetic activity*. Space Weather, doi:[10.1029/2020SW002641](https://doi.org/10.1029/2020SW002641)

⁷Zeithöfler J., Bloßfeld M., Rudenko S., Dettmering D., Seitz F. (2023): *Station-dependent satellite laser ranging measurement corrections for TOPEX/Poseidon*. Advances in Space Research, doi:[10.1016/j.asr.2022.09.002](https://doi.org/10.1016/j.asr.2022.09.002)

DOGS Radio Interferometry (DOGS-RI): DOGS-RI is used for the analysis of VLBI observations and enables i) to compute VLBI solutions consisting of estimates of antenna coordinates, the full set of Earth Orientation Parameters (EOP), quasar positions, troposphere and VLBI-specific (e.g., clock) parameters, and ii) to generate datum-free NEQs that can be further processed and solved with DOGS-CS or by external partners. In the context of DGFI-TUM's role as IVS AC (cf. Tab. 1.1), the SINEX (Solution INdependent EXchange) format is used for this purpose. The updates, improvements and new models in DOGS-RI in 2022 include:

- new IVS naming convention for the observation data files,
- modifications to handle IVS Intensive sessions,
- adaption of common routines with DOGS-OC,
- new ocean tide model EOT20⁴,
- use of different numbers of zonal tides for Earth rotation.

DOGS Combination and Solution (DOGS-CS): DOGS-CS is used to (i) process NEQ systems created by DOGS-OC/-RI or externally provided NEQ systems, (ii) accumulate satellite-specific or technique-specific NEQs into one multi-satellite/long-term technique-specific NEQ in the context of a terrestrial reference system (TRS) realization and EOP determination, (iii) combine NEQs of different techniques, and (iv) compute loose-constrained or minimum-constrained solutions. DOGS-CS can also be used to perform numerous other NEQ operations such as rescaling, constraining, introducing new parameters and transforming parameters. In 2022, the interfaces to the SINEX format were extended and the runtime stability increased.

As one example, Fig. 1.1 shows the usage of DOGS for the realization of a regional geocentric Epoch Reference Frame (ERF), see. Sect. 1.4 and Kehm (2022). SLR and VLBI observations are processed using DOGS-OC/-RI, GNSS observations are processed using the Bernese GNSS software. All NEQs are forwarded to DOGS-CS via the SINEX interface. Within DOGS-CS, the inter-technique combination, the datum realization as well as the solution of the epoch-wise reference frame are performed.

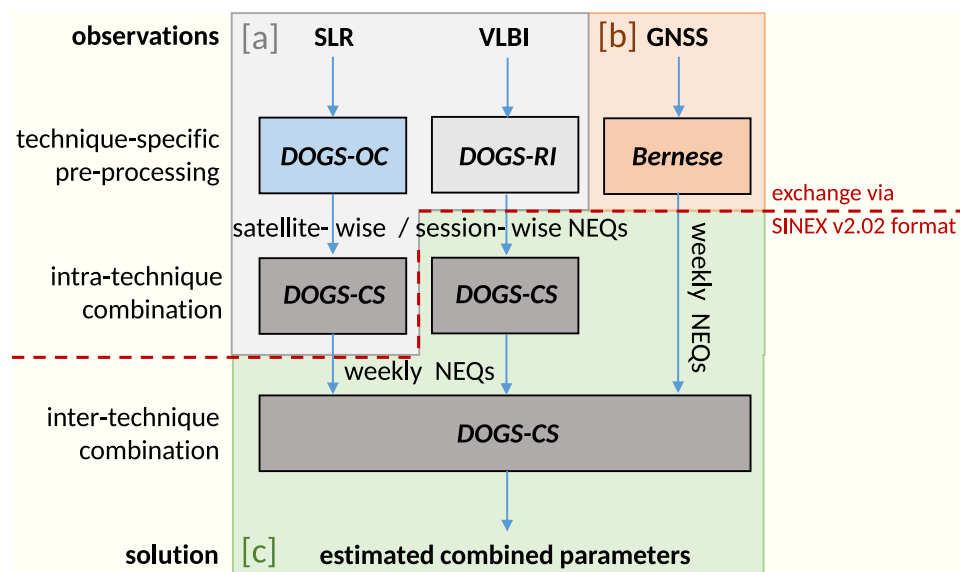


Figure 1.1: Using DOGS for the realization of a regional geocentric Epoch Reference Frame: [a] Processing of SLR and VLBI, [b] Processing of the SIRGAS GNSS network, [c] Inter-technique combination. Picture taken from Kehm (2022).

1.1 Analysis of Space-Based Microwave Observations

VLBI data analysis

DGFI-TUM has been an operational Analysis Center (AC) of the International VLBI Service for Geodesy and Astrometry (IVS) since 2008. Since 2018, VLBI data analysis is based on our in-house VLBI analysis software DOGS-RI (see previous section). The main task of each IVS AC is to provide datum-free normal equations (NEQs) for the so-called Rapid Turnaround VLBI sessions, which are scheduled twice a week. These NEQs are combined and solved by the IVS Combination Center, which is jointly operated by DGFI-TUM and the Federal Agency for Cartography and Geodesy (Bundesamt für Kartographie und Geodäsie, BKG). The solutions include both the EOP and the positions of the observing VLBI antenna reference points in the terrestrial reference system.

In 2022, two focal points were worked on. Firstly, the investigations on the reduction of non-tidal loading (NTL) signals in VLBI analysis were extended to a secular Terrestrial Reference Frame (TRF), following the work on the effects in single-session solutions in 2020/2021. On the one hand, this is important for the 2020 realization of the ITRS at DGFI-TUM, the DTRF2020 (see Sect. 1.4), which uses the data of different geodetic space techniques, and in which NTL is reduced at NEQ level. The corresponding relevant properties of NTL are discussed by Glomsda et al. (2022). In addition, the reduction of NTL in the determination of VLBI-only secular TRFs has been studied. The theoretical implications of reducing NTL at both the observation and the NEQ level of the estimation model were derived, and then different VLBI-only TRFs were calculated and compared. Accounting for NTL signals improves the long-term stability of such secular reference frames.

Secondly, the new generation of VLBI data provided by the VLBI Global Observing System (VGOS) antennas was analyzed. Unlike the old S/X-band system, VGOS provides observations from broadband microwave measurements with a common calibration of the ionospheric delay. DGFI-TUM recently compared the results of three years of simultaneous legacy and VGOS sessions between 2019 and 2021⁸. In general, there are fewer antennas per VGOS session, but since these antennas tend to be smaller and faster than their legacy counterparts, they collect more observations per unit time. In addition, the formal errors of the VGOS broadband measurements are usually smaller (Fig. 1.2). However, the global distribution of VGOS antennas is poor, as none of them were operational in the southern hemisphere until December 2021. Therefore, the first VGOS results, while promising, are not yet able to replace the legacy observations.

A subset of these VGOS sessions was already available for the 2020 realization of the ITRS, so DGFI-TUM had to deal with including them in the DTRF2020. The legacy and VGOS antenna networks are basically separate, except for three antennas that provide observations in both modes. But there are other ways to connect the networks. Initial investigations into this have already been carried out in connection with the 2017 continuous VLBI campaign, CONT17. As described by Kwak et al. (2022), one can use the available local ties between co-located legacy and VGOS antennas and combine the common EOP. For the DTRF2020, we have further combined the velocities of co-located antennas and included two types of special sessions with both legacy and VGOS antennas, i.e., the so-called mixed mode sessions and the local tie measurements based on short-baseline interferometry at the Onsala Space Observatory in Sweden⁹.

⁸Glomsda M., Seitz M., Angermann D. (2023): *Comparison of simultaneous VGOS and legacy VLBI sessions*. In: Armstrong K. et al. (Eds.), IVS 2022 General Meeting Proceedings

⁹Varenus E. et al. (2021): *Short-baseline interferometry local-tie experiments at the Onsala Space Observatory*. Journal of Geodesy, doi:[10.1007/s00190-021-01509-5](https://doi.org/10.1007/s00190-021-01509-5)

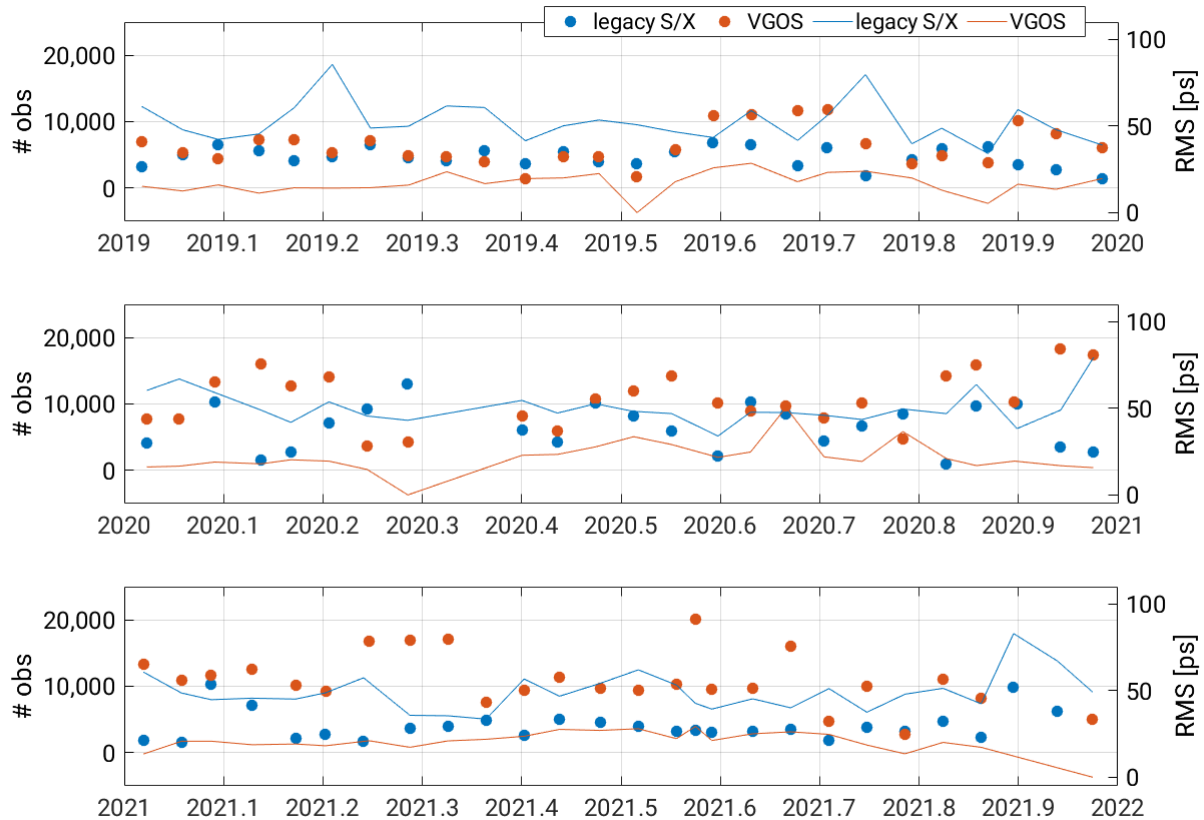


Figure 1.2: Number of observations (dots) and root-mean-square (RMS) error of the observation residuals (lines) per simultaneous – yet separately solved – legacy (blue) and VGOS (red) session.

In 2023, it is planned to routinely process the VGOS sessions, which will soon be scheduled once a week. An important research question in this context is how to combine the parameters estimated from legacy and VGOS observations. We aim to provide NEQs for the daily intensive sessions that contain fewer antennas (only 2–3) than the Rapid Turnaround sessions and can probably even be analyzed automatically. The Rapid Turnaround sessions will have to be reprocessed using the new (a priori) antenna positions of the 2020 ITRS realization.

DORIS data analysis

DGFI-TUM has been an Associate Analysis Center (AAC) of the International DORIS Service (IDS) since 2019. In this context, a major focus of DGFI-TUM is the determination and further improvement of precise orbits of Earth observation satellites. In 2022, strategies for treating orbit manoeuvres and mass changes were further developed and attitude data for Jason-3 (quaternions for the satellite main body and solar panel angles) from NASA’s Crustal Dynamics Data Information System (CDDIS) were processed and interpolated for a one-year time interval.

Two studies were conducted to quantify radial orbit errors of altimetry satellites and to improve the orbit of the TOPEX/Poseidon satellite (see Sect. 1.3). For these studies, as well as for the comparison of DGFI-TUM orbits with those of CNES, GFZ and NASA/GSFC, a database has been established which currently contains the orbits of nine altimetry satellites (in ITRF2014) using DORIS and, for some orbit solutions, also GNSS or SLR observations.

Currently, orbit perturbations caused by solar radiation pressure, Earth albedo and the upper thermosphere (due to coupling mechanisms between thermospheric density and solar radiation) are being investigated to reduce remaining β' (angle between ecliptic and orbital plane)-

dependent systematics, visible in the arcwise orbital RMS fits of DORIS (and, to a lesser extent, also SLR) observations. From Fig. 1.3 it is evident that higher DORIS (and SLR) residuals are obtained when the satellite orbits in the so-called ‘fixed’ mode, which means that the satellite is constantly oriented along the direction of flight (i.e. the yaw axis points perpendicular to the Earth ellipsoid and the roll axis points in the direction of flight).

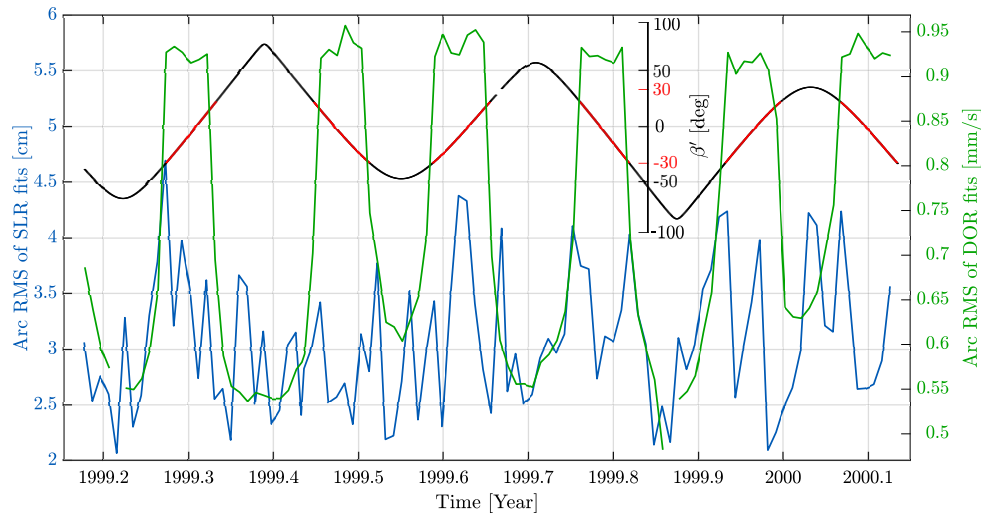


Figure 1.3: Arc-wise RMS of DORIS fits [mm/s] and SLR fits [cm] for TOPEX/Poseidon (orbits based on the nominal yaw-steering model). In addition, β' (angle between the ecliptic and the orbital plane) is shown. The red interval for β' indicates when the satellite flies in the yaw-fixed mode.

GNSS data analysis

DGFI-TUM contributes to several international GNSS-based initiatives such as (i) the IGS (International GNSS Service) Tide Gauge Benchmark Monitoring (TIGA), (ii) the IGS Multi-GNSS Experiment (MGEX), (iii) the ITRF densification in Latin America by SIRGAS, the Geodetic Reference System for the Americas, (iv) the determination of dense velocity fields and (v) the modeling of surface deformations. This contribution is achieved by installing and providing data from continuously operating GNSS stations, computing loosely constrained daily and weekly NEQs for regional GNSS networks, determining GNSS station velocities from cumulative solutions, and other activities.

One of the research objectives of DGFI-TUM in this context is the appropriate geodetic datum definition in regional networks. Typically, GNSS data analysis in regional networks introduces the satellite orbits, the satellite clock corrections and the EOP as known parameters. Station coordinate solutions are obtained by applying no-net-rotation and -translation conditions w.r.t. reference stations belonging to a global reference network, such as the ITRF or IGS TRF. Changes in the TRF or a degradation of the reference coordinates (e.g., due to coordinate extrapolation or decommissioning of fiducial stations) can create spurious artifacts in station-specific displacement time series of GNSS regional networks. These artificial effects can lead to a misinterpretation of GNSS results, e.g., surface kinematics, NTL signals, etc.

Fig. 1.4 shows the transformation parameters between weekly positions of the SIRGAS regional network and weekly global IGS coordinates in IGS14/IGb14. The rotations are negligible (below 0.01 mas), the translations are all well below 1.0 mm, respectively, when using all SIRGAS/IGS common stations (blue lines). All parameters are around zero when only the fiducial stations are used for the transformation (red lines). The scale based on all SIRGAS/IGS common stations presents fluctuations between -0.2 ppb in 2000 and 0.0 ppb in 2017. The jump evident at

the end of January 2017 is due to the update of the model to correct the z-PCOs (phase center offsets in z-direction) of GNSS antennas. This change affects the network scale and the height of the GNSS stations. Indeed, the scale values estimated using the fiducial stations only (red line in the uppermost panel in Fig. 1.4) present a bias of about -0.02 ppb between 2000 and 2017 (when the IGS14/IGb14 was officially adopted by IGS). Then, these values are close to zero until the end of 2020. Afterwards, they describe a negative drift. Given that the IGS14/IGb14 TRF solution contains GNSS data until February 2020, it is possible that this drift is caused by the extrapolation of IGS14/IGb14 station coordinates for operational TRF alignments in the IGS products generation (cf. Sánchez et al., 2022). To improve the reliability of the datum realization in regional networks, DGFI-TUM developed an innovative approach based on the combination of global GNSS NEQs (regionally densified) with SLR and VLBI NEQs to directly realize the geocentric origin, scale and orientation of the regional network in a single adjustment, see Sect. 1.4, Kehm (2022) and Kehm et al. (2022).

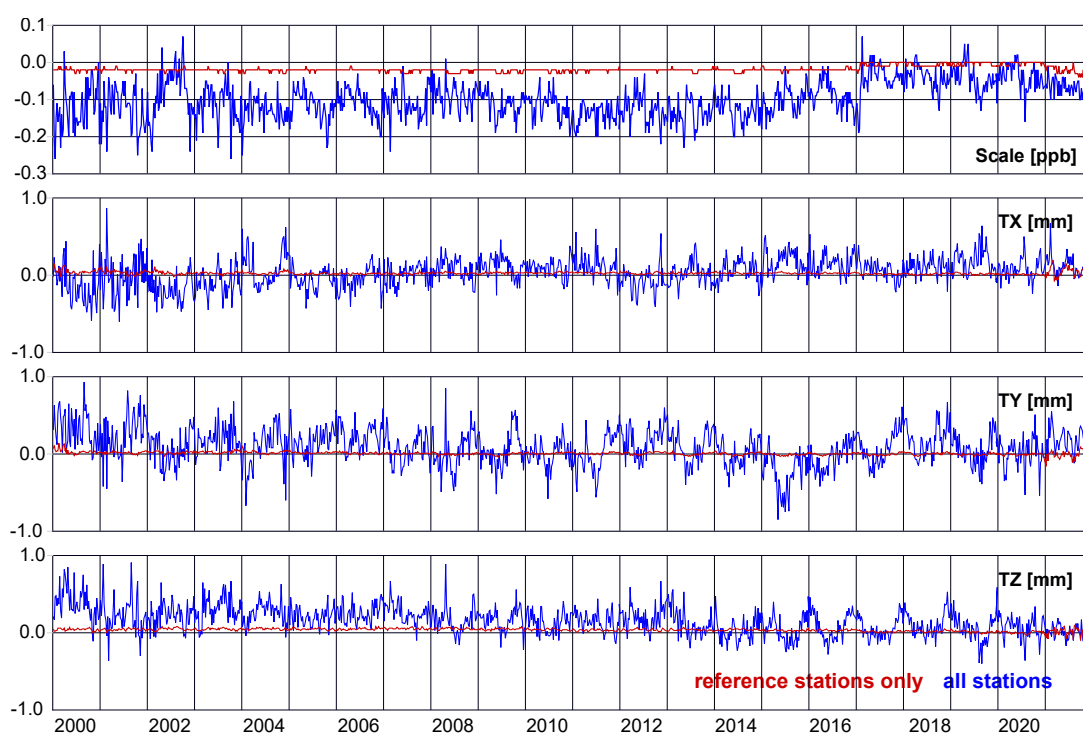


Figure 1.4: Differences in scale and translation parameters between SIRGAS weekly solutions and IGS weekly coordinates in IGS14/IGb14 using fiducial stations only (red lines) and all SIRGAS/IGS common stations (blue lines). The respective rotations are all close to zero.

GNSS results (station positions, velocities and time series) are used as input data for modeling the Earth's surface kinematics^{10,11} In 2022, DGFI-TUM developed a novel Bayesian approach to automatically and simultaneously detect discontinuities and trend changes in GNSS time series to estimate reliable vertical land motion signatures (Oelsmann et al., 2022). This is particularly needed to validate regional sea level changes inferred from satellite altimetry and tide gauge records (see also Sect. 2.2).

¹⁰Sánchez L., Völksen C., Sokolov A., Arenz H., Seitz F. (2018): *Present-day surface deformation of the Alpine region inferred from geodetic techniques*. Earth System Science Data, doi:10.5194/essd-10-1503-2018

¹¹Sánchez L. and Drewes H. (2020): *Geodetic monitoring of the Variable surface deformation in Latin America*. IAG Symposia, doi:10.1007/1345_2020_91

1.2 Analysis of Satellite Laser Ranging Observations

SLR data analysis

DGFI-TUM has been involved in the International Laser Ranging Service (ILRS) as an Analysis Center (AC) for many years. In 2022, several official contributions were routinely computed on a daily or weekly basis (cf. tab. 1.2), using SLR observations to LAsER GEOdynamic Satellites 1 and 2 (LA-1/-2) and to Etalon 1 and 2 (ET-1/-2). They are provided to the ILRS Combination Center at ASI (Agenzia Spaziale Italiana), which combines up to eight different AC solutions into a daily/weekly ILRS solution used e.g. by IERS (International Earth Rotation and Reference Systems Service) for the operational determination of EOP.

DGFI-TUM has also contributed to various ILRS reprocessing campaigns. One example is the continuation of the ILRS Station Systematic Error Monitoring Pilot Project (SSEM-PP), which will be operated continuously from 2022 under the name SSEM-X (cf. v230 solution in Tab. 1.2). Another example of reprocessing is the prototype processing of v70 solutions for 2020 and 2021 (v450), based on the new SLR terrestrial reference frame SLRF2020. This solution is used to (i) improve the SLRF2020 solution, which is an extended version of ITRF2020, and (ii) provide these solutions to the IERS to determine EOP aligned to ITRF2020.

Table 1.2: Routine and project-specific solutions computed by the DGFI-TUM ILRS AC during 2022.

ILRS code	description	file format
v170	daily LA-1/-2 and ET-1/-2 TRF and EOP solutions	SINEX
v70	weekly LA-1/-2 and ET-1/-2 TRF and EOP solutions	SINEX
v70-sp3c	weekly LA-1/-2 and ET-1/-2 orbit solutions	SP3C
—	daily orbit predictions for LA-1/-2 and ET-1/-2 and others	CPF(v2)
v230	weekly LA-1/-2 and ET-1/-2 TRF and EOP solutions (incl. biases)	SINEX
v450	prototype processing of v70 based on the new SLRF2020	SINEX

Besides the official contributions provided by DGFI-TUM to the ILRS Analysis Standing Committee, numerous other daily and weekly solutions are computed (cf. Tab. 1.3). According to the standards used for the v170 and v70 processing, DGFI-TUM continuously computes 10-satellite solutions. The six additional spherical satellites (compared to the ILRS standard solution with 4 satellites) are LARES (LAsER RELativity Satellite), LARES-2, Ajisai, Stella, Starlette, and Larets.

Table 1.3: Further solutions computed by the DGFI-TUM ILRS AC during 2022.

ILRS code	description	file format
—	daily 10-satellite TRF and EOP solutions	SINEX
—	weekly 10-satellite TRF and EOP solutions	SINEX
—	weekly GM solution based on 10 satellites	SINEX
—	weekly SH deg 1 solution based on 10 satellites	SINEX
—	weekly SH deg 2 solution based on 10 satellites	SINEX
—	weekly 10-satellite (reduced dynamic) orbit solutions	SP3C
—	daily orbit predictions for LARES, LARES-2, Ajisai, Stella, Starlette, Larets	CPF(v2)

These solutions are used to regularly determine various geophysical parameters such as the Earth's gravitational constant (GM; Fig. 1.5) or the Center of Mass (CM) of the Earth system (first-degree spherical harmonics; SH). The quality of weekly GM estimates has improved over

the years, and today GM can be reliably estimated on a weekly basis due to the numerous SLR targets tracked and combined. These solutions will be published soon. In addition, orbit predictions of these satellites are provided to the ILRS on a daily basis to help SLR stations acquire their targets more quickly and accurately.

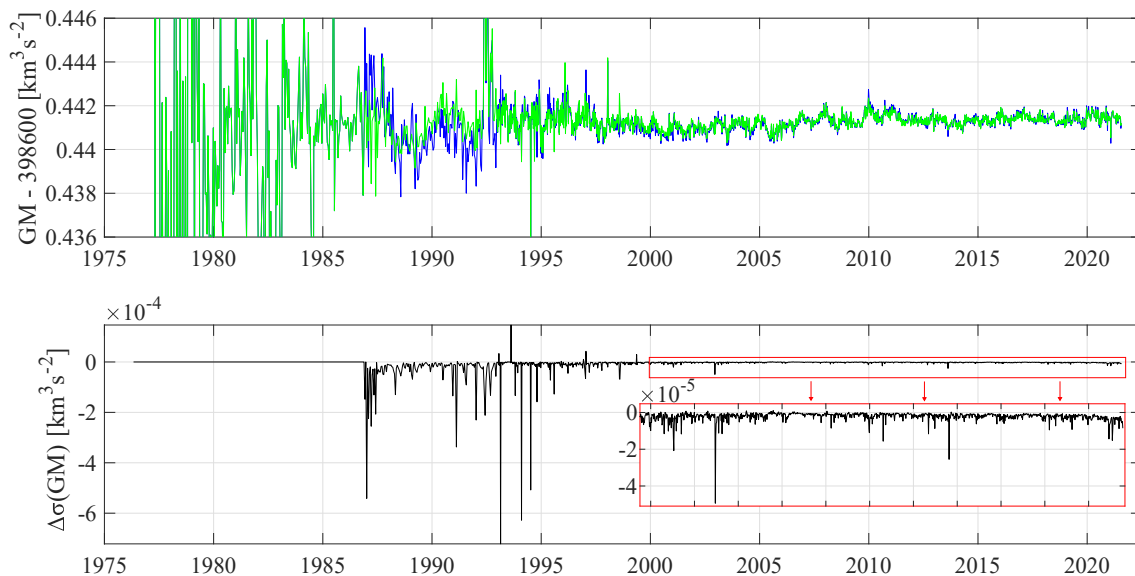


Figure 1.5: Upper panel: 15-/7-daily GM estimates based on 4-satellite (LA-1/-2, ET-1/-2) and 12-satellite (four satellites + LARES, LARES-2, Ajisai, Stella, Starlette, Larets, BLITS, Westpac) solutions. SLR observations to BLITS and Westpac were available only a few years in the past. Lower panel: Standard deviation (STD) differences of 15-/7-daily GM estimates (12-sat. solution – 4-sat. solution). The red box shows the zoom on the STD differences since 2000.

SLR data management

DGFI-TUM has operated the EUROLAS Data Center (EDC) since the founding of the ILRS in 1998. The EDC is one of two ILRS Data Centers (DC) worldwide (the other being the Crustal Dynamics Data Information System, CDDIS¹², operated by NASA). The EDC's role as ILRS Operation Center (OC) and as ILRS DC is to ensure the quality of the submitted SLR data. There is a daily and hourly data exchange with the NASA OC and CDDIS. All data and results are publicly available to the ILRS community via ftp (<ftp://edc.dgfi.tum.de>) and the dedicated website <https://edc.dgfi.tum.de>. For more details see Section 4.6.

The EDC maintains several mailing lists for the exchange of information, data and results. In 2022, 66168 Consolidated Prediction Format (CPFv1/v2) files from 104 satellites were provided to SLR stations. In addition, the EDC distributed SLR-Mails (47 messages in 2022), SLR-Reports (753 in 2022) and SLR-Urgent-Service-Mails (77 in 2022).

In 2022, 218299 pass segments of normal points (NPTv1/v2) were submitted by 40 SLR stations observing 113 different satellites. There were six new satellite missions tracked by SLR stations, namely ELSA-d (Target), Galileo-223, Galileo-224, LARES-2, SWOT and GLONASS-146. With Tsukuba, Japan, a new station was added to the ILRS network. In addition, the implementation and transition to the new official ILRS data format of the Consolidated Laser Ranging Data (CRDv2, since 2022-08-01) Format 2.0 and the Consolidated Prediction Format (CPFv2, since 2022-03-01) was completed.

¹²<https://cddis.nasa.gov/>

1.3 Determination of Satellite Orbits

Besides the determination of satellite orbits and orbit predictions of spherical satellites within the ILRS AC (Sect. 1.2), also non-spherical satellites are in the target of the DGFI-TUM orbit analysis. The main focus was on the altimetry satellites TOPEX/Poseidon and Jason-1/-2/-3.

Orbit determination for altimetry satellites

Reduced-dynamic orbits of TOPEX/Poseidon and Jason-1/-2/-3 were calculated from SLR observations for the entire duration of the respective satellite mission (for Jason-3 until October 2021). TOPEX/Poseidon orbits are based on a continuous and analytical SLR measurement correction function developed at DGFI-TUM⁷ to resolve optical phase center variations and effects related to the spacecraft and SLR tracking stations (e.g., range biases; RBs). In addition to the SLR-based orbits, also DORIS-based orbits (except for Jason-3) were calculated. The mean values of the RMS fits of the DORIS observations are 0.75 mm/s for TOPEX/Poseidon and 0.50 mm/s for Jason-1/-2.

In 2022, DGFI-TUM performed precise orbit determination (POD) tests for TOPEX/Poseidon (1992-2005), Jason-1 (2002-2013), Jason-2 (2008-2019) and Jason-3 (2016-2021) using the newly published 2020 ITRS realization ITRF2020. This realization includes annual and semi-annual variations as well as postseismic deformations of the SLR stations. Compared to previous ITRS realizations (ITRF2014, DTRF2014), the ILRS based its input solution on satellite- and station-specific long-term mean RBs derived from observations to LA-1/-2 and ET-1/-2 between 1993.0 and 2020.5. These corrections had been subtracted by the ILRS ACs at observation level. These POD tests did not use long-term mean RBs applied for ITRF2020, as these have not yet been published. Two cases were calculated for both the ITRF2020 and the SLRF2014: with and without the estimation of satellite-specific arc-wise RBs. Without the application of the long-term mean RBs, the ITRF2020 provides poorer orbit quality (Fig. 1.6, right) and worse results in the altimetry crossover analysis than the SLRF2014 when no SLR RBs are estimated. The estimate of arc-wise RBs absorbs this mis-modelling, so ITRF2020 performs slightly better than SLRF2014 (Fig. 1.6, left) by providing a smaller mean RMS fit (across all four satellites) of 1.7 versus 1.8 cm. Until the long-term mean RBs used to derive ITRF2020 are published, the only way to derive precise orbits and other products from SLR observations to altimetry satellites based on ITRF2020 is to estimate arc-wise RBs.

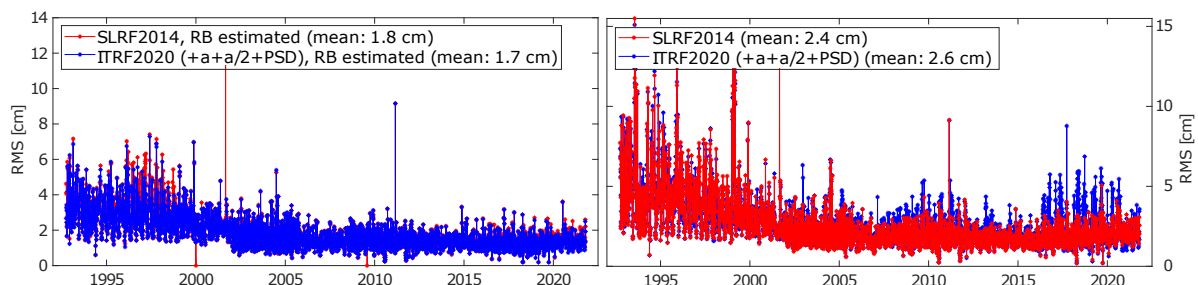


Figure 1.6: RMS fits of SLR observations of TOPEX/Poseidon, Jason-1/-2/-3 obtained using SLRF2014 (red) and ITRF2020 including annual and semi-annual (a , $a/2$) variations as well as post-seismic deformations (PSD) of SLR stations (blue) without (right) and with (left) the estimation of arc-wise RBs.

Radial errors of contemporary altimetry satellite orbits

Within the framework of the **DFG project MEPODAS** (Mitigation of the current errors in precise orbit determination of altimetry satellites), strategies are developed to minimize currently still existing POD errors of altimetry satellites, in particular, in radial direction. The knowledge of the exact distance of the altimetry satellite from the sea surface is crucial for the reliable determination of the sea level and its regional and global evolution (see Section 2). Over the past 30 years, significant progress has been made in improving orbit quality, increasing orbit accuracy in the radial direction from the decimeter to the centimeter and even sub-centimeter level.

SLR-based altimeter orbits calculated at DGFI-TUM were compared with external orbit solutions, especially in radial direction. To assess their accuracy, 33 orbit solutions from 11 altimetry satellites derived at six institutions using different observation techniques (SLR, DORIS, GPS, PRARE, Doppler, altimeter crossover) in technique-specific extended ITRF2014 realizations were studied¹³. In order to be able to calculate orbit differences over the length of the orbit file of the reference solution or over an arbitrary time span, different interpolation methods such as spline, Hermite, Newton and Lagrange interpolation have been implemented. Mean radial orbit differences of about -0.15 to -0.24 cm between the JPL IGS14 orbits of Jason-2/-3 and Sentinel-3A/-3B w.r.t. the CNES POE-F, GFZ PSO v02, and CPOD orbits were discovered and are currently being investigated. A jump in the RMS values of radial orbit differences between the CPOD and JPL IGS14 orbital solutions of Sentinel-3A/-3B was detected as of January 1, 2021, and can be attributed to the change in the background models used in the operational CPOD solutions since that date. Also clear periodic millimeter-level variations in the RMS and mean radial orbit differences caused by differences in NTL modeling and other effects are visible, cf. Sentinel-3A in Fig. 1.7.

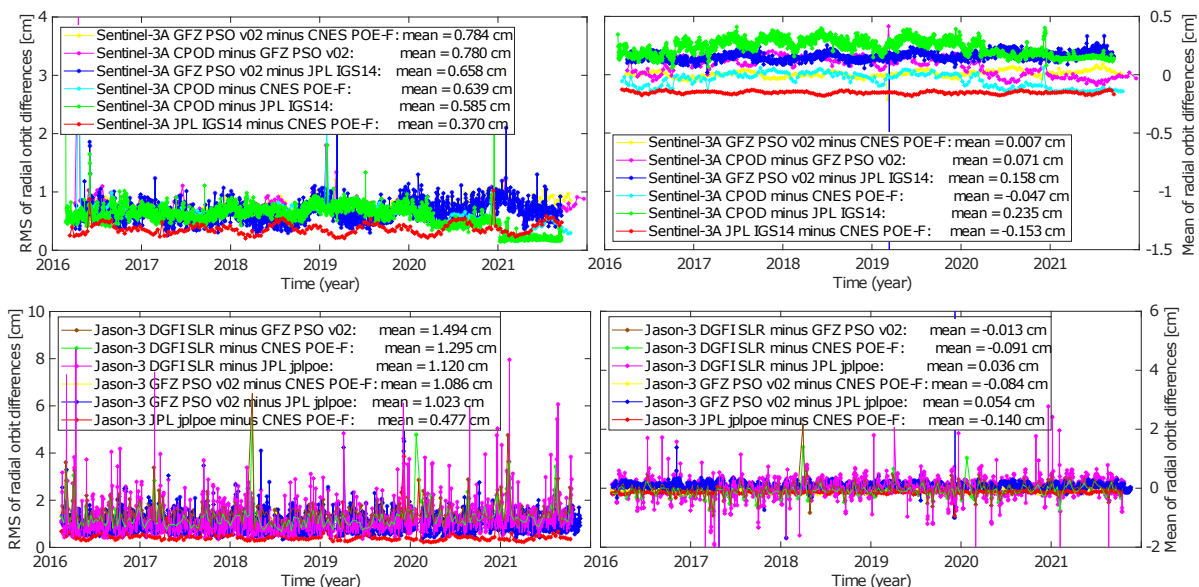


Figure 1.7: RMS and mean values of the radial orbit differences of various Sentinel-3A (upper panels) and Jason-3 (lower panels) orbit solutions including DGFI-TUM SLR-only orbits. Larger differences of SLR-only orbits compared to orbits based on DORIS and GPS observations (lower panels) result from gaps in the SLR observations.

¹³Rudenko S., Dettmering D., Zeithöfler J., Alkhal R., Upadhyay D., Bloßfeld M. (2023a): Radial orbit errors of contemporary altimetry satellite orbits. Surveys in Geophysics, doi:10.1007/s10712-022-09758-5

In the context of this study, a review of the main improvements in the POD background models and their impact on the orbit accuracy was performed. It compared radial orbit differences, single-satellite crossover differences, and geographically correlated orbit errors of the orbits of the 11 altimetry satellites from different institutions. The study highlights the fact that the major improvements in orbit quality are due to significant improvements in the modeling of Earth's time-variable gravity, the improvement of ITRS realizations, and the use of GNSS in addition to DORIS and SLR observations.

The SLR-based orbits of Jason-1/-2/-3 and TOPEX/Poseidon of DGFI-TUM are published under the acronym DGFI-TUM DSO1¹⁴. Additional orbit validation results using sea surface height crossover analysis obtained in this study are presented in Sect. 2.1.

Refined modeling of the thermospheric density

Different perturbing forces act on satellites in Earth orbit. For low-orbiting satellites, the largest non-gravitational force is atmospheric drag, which depends on thermospheric density. Spatial and temporal density variations are calculated based on atmospheric models (e.g., NRLMSISE-00, NRLMSIS 2.0). These models are supported by, among other things, daily 10.7-cm solar radio flux values and magnetic indices, typically represented at a temporal resolution of three hours. An analysis of the resulting density of the two models mentioned above exhibits jumps, mainly due to an update of the radio flux value used by the model. Sudden changes in density result in the effects of the atmosphere on the satellite not being modeled optimally. To reduce the jumps, a 4th-order interpolation of the radio flux and the magnetic indices was implemented.

Density time series without and with (smooth) interpolation are shown in Fig. 1.8. A density difference of about 10 % between the two models is evident, as well as a smoothing effect of similar magnitude. Further details on the analysis of the thermospheric density modeling performed as part of the **DFG project TIPOD** can be found in Sect. 3.1.

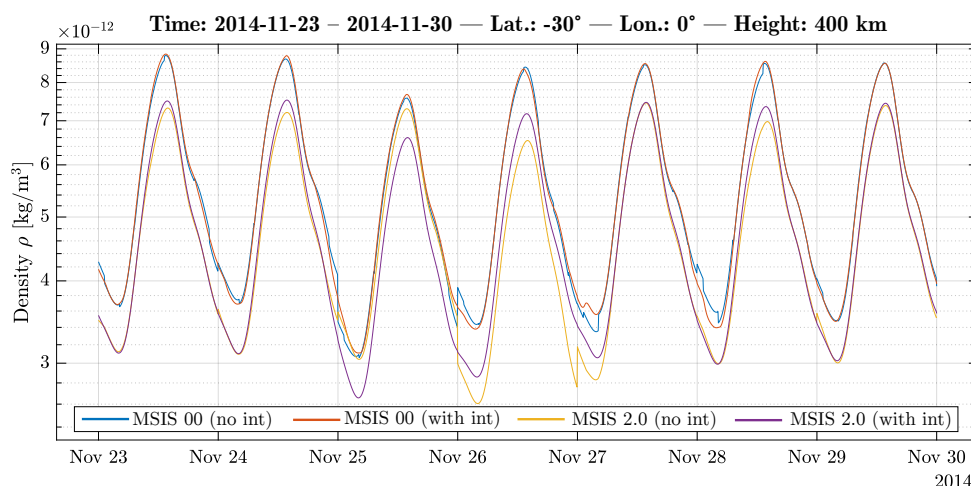


Figure 1.8: Neutral density time series derived from the empirical atmosphere models NRLMSISE-00 and NRLMSIS 2.0. The curves show density values without and with the application of an interpolation of the model values.

¹⁴Rudenko S., Zeithöfler J., Bloßfeld M. (2023b): DGFI-TUM DSO1 orbits of altimetry satellites TOPEX/Poseidon, Jason-1, Jason-2 and Jason-3 derived from SLR data in the SLRF2014 reference frame. Deutsches Geodätisches Forschungsinstitut, Zenodo, doi:[10.5281/zenodo.7441352](https://doi.org/10.5281/zenodo.7441352)

1.4 Determination of Reference Frames

ITRS Combination Center at DGFI-TUM: Calculation of DTRF2020

In 2022, the ITRS CC at DGFI-TUM focused on finalizing DGFI-TUM's ITRS Realization 2020, the *DTRF2020*. The approach followed is schematically shown in Fig. 1.9. The main tasks in 2022 were (i) the final computation of one TRF solution per observation technique, (ii) the analysis and comparison of the datum parameters provided by the individual techniques, (iii) the analysis and comparison of EOP, (iv) the combination of the techniques, and (v) the analysis of the DTRF2020 results. The DTRF2020 was provided to the IERS Directing Board and to the Analysis Coordinators of the related IAG Scientific Services IERS, IGS, IVS, ILRS, and IDS, for final testing in early 2023. The release of DTRF2020 is scheduled for the first half of 2023.

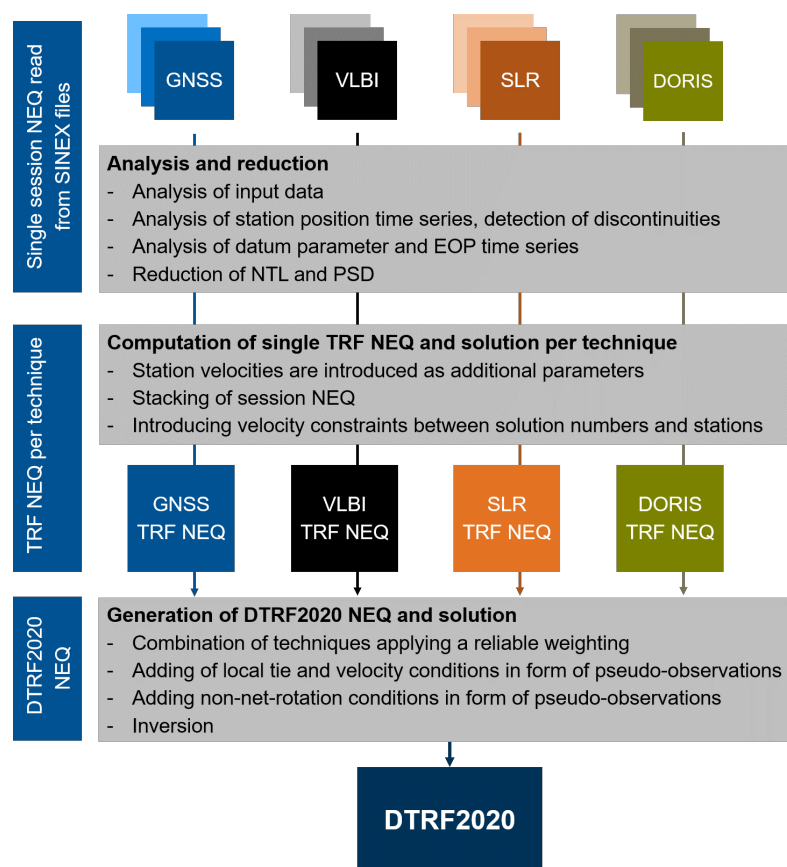


Figure 1.9: DTRF2020 computation strategy. The two-step approach is based on the combination of normal equations (NEQs). In the first step, the observations per technique are analyzed and technique-specific TRF NEQs/solutions are calculated. In the second step, the techniques are combined to the DTRF2020 solution.

Computation of one TRF solution for each technique

The completion of the intra-technique TRF solutions marks the end of the work from 2021. A particularly large amount of effort was put into the generation of the VLBI and DORIS solutions. The DORIS solution is very fragmented and had to be stabilized by introducing conditions to combine velocities between successive solution numbers of stations affected by discontinuities. In the case of VLBI, observations from the new VGOS station network were available for the first time (cf. Hellmers et al., 2022) and had to be combined with the legacy network in several steps (cf. Sect. 1.1).

Analysis of datum parameters

The different techniques contributing to the DTRF2020 provide individual intrinsic geodetic datum information which is examined to realize the DTRF2020 datum in accordance to the IERS Conventions 2010¹⁵. SLR observations are very sensitive to the Earth's CM (Fig. 1.10) and are therefore used in full length to realize the DTRF2020 origin. While in the previous ITRS realizations of DGFI-TUM (e.g., DTRF2014; Seitz et al., 2022) only VLBI and SLR provided independent information about the scale, in the case of the current ITRS 2020 realization this is now also true for GNSS due to the disclosure of the Galileo z-Phase Center Offsets (PCO). We analyzed and compared the scales provided by VLBI, SLR, and GNSS and found agreement between VLBI and GNSS in the long-term mean within 0.25 mm (epoch 2010.0) and 0.025 mm/year. The SLR scale time series shows a small offset and drift from VLBI and GNSS of about 2.2 mm (epoch 2010.0) and -0.1 mm/yr. To keep this small deviation visible in the DTRF2020, the SLR scale was not used to realize the DTRF2020 scale. The scale time series of all techniques with respect to DTRF2020 are displayed in Fig. 1.11.

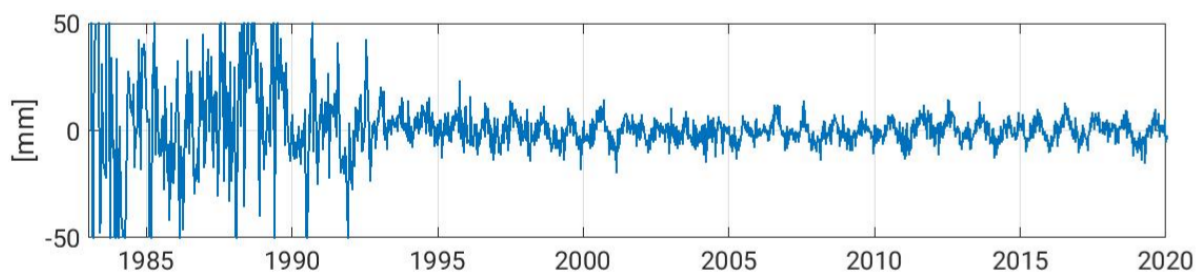


Figure 1.10: Z-component of the SLR intrinsic translation time series.

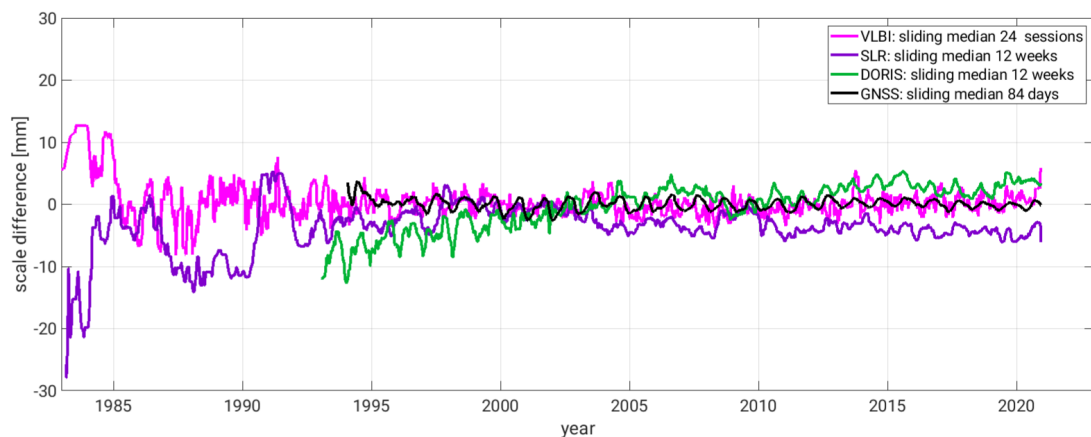


Figure 1.11: Time series of scale parameters derived by the different geodetic space techniques with respect to DTRF2020 (sliding medians).

A relevant question related to the time series of datum parameters was the extent to which annual and semiannual signals are attenuated when NTL displacements of station positions are reduced from the input NEQs. We considered CM-related NTL displacements of the GGFC for all techniques (Glomsda et al., 2022). Figure 1.12 shows the SLR, VLBI, and GNSS scale time series for the two cases where NTL was reduced and not reduced, respectively, and the corresponding amplitude spectra. The reduction of NTL leads to a significant decrease in the amplitude of the annual and, to a lesser extent, the semiannual signal. The same result was obtained for the SLR origin time series. It can be concluded that NTL displacements can explain most of the annual signal in the origin and the scale time series.

¹⁵Petit G. and Luzum B. (Eds.) (2010): *IERS Conventions 2010*. IERS Technical Note 36, ISBN 3-89888-989-6

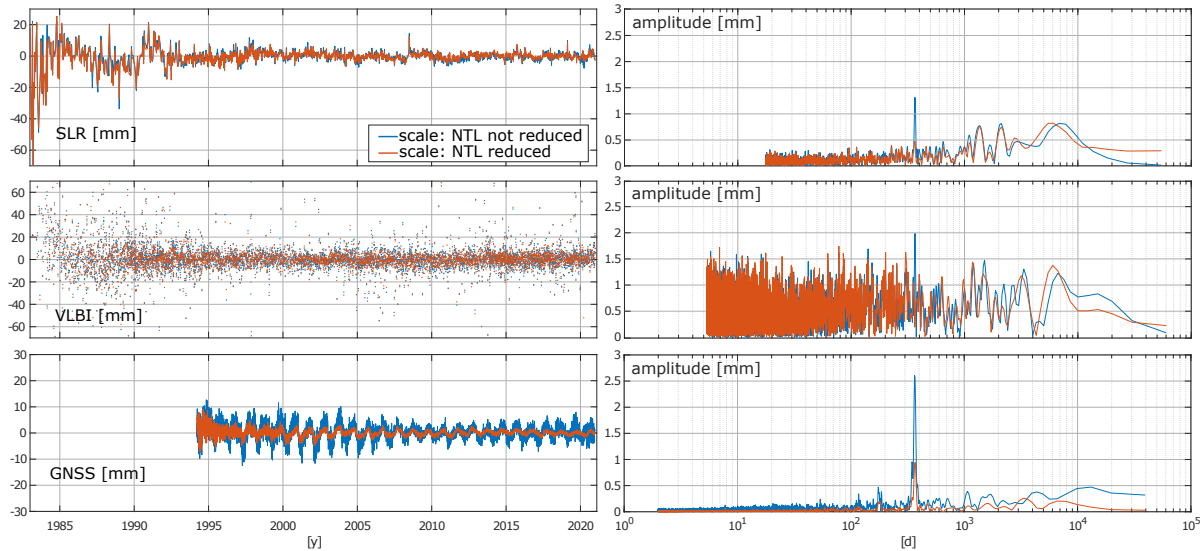


Figure 1.12: Intrinsic SLR, VLBI and GNSS scale series derived with/without reduction of NTL from the weekly, session-wise or daily input NEQs (left) and corresponding Lomb-Scargle amplitude spectra (right).

Analysis of Earth Orientation Parameters

Consistent with the DTRF2020 reference frame, a combined EOP series was estimated based on the individual contributions of the four techniques (Tab. 1.4). Two to four techniques contribute to the terrestrial pole offsets, the corresponding rates, and to LOD. We compared all EOP series and analyzed the differences in terms of periodic signals. We found good agreement for all contributions. Only the SLR-derived LOD series shows periodic signals at tidal frequencies (periods of 13.66, 14.36, and 27.6 days) compared to the other contributions and was excluded from the EOP combination.

Table 1.4: Contribution of the four geodetic space techniques to the combined EOP series. The LOD series derived from SLR was found to be affected by periodic (tidal) signals and was not used in the combination.

	terr. pole offsets	$\Delta UT1$	nutation	terr. pole rates	LOD
GNSS					
SLR					
VLBI					
DORIS					

Combination of geodetic space techniques

The combination of the techniques was performed considering the results of datum parameter and EOP analyses. Station networks were combined by introducing local tie vectors and conditions for equating station velocities at co-location sites as pseudo-observations. The EOP as common parameters were combined directly. Relative weighting was applied to ensure appropriate representation of the techniques in the DTRF2020 solution. Variance factors are considered as well as weighting factors that account for over- or underestimation of STDs. The RMS of station position residual time series of selected stations is used to derive a reference STD for the mean station position. Comparing these STDs to the ones estimated in the technique-specific TRF solutions yields a mean scaling factor that reflects a systematic error in the statistics of the input NEQs. The factors (applied as squared values to weight the NEQs

in the combination) are 1.95 (VLBI), 1.03 (SLR) and 2.95 (DORIS). In particular, the precision of DORIS station coordinates appears to be significantly underestimated when using only the statistical information provided in the SINEX input files.

For GNSS, the situation is different since the precision of station coordinates, especially station velocities, is known to be affected by colored noise in the time series. To calculate the impact on the STDs estimated in the GNSS-TRF solution, we analyzed the time series of station positions of 120 globally distributed GNSS stations with an individual observation time span of at least 15 years using maximum likelihood estimation (MLE) as implemented in the software HECTOR¹⁶.

We obtained a scaling factor of about 14.7 for the precision of station velocities estimated from the long station time series. However, including this factor in the weighting scheme of DTRF2020 would result in an improved relative weight of GNSS over the other techniques for station velocities only, while station positions and EOP are affected to a lesser extent. Therefore, we decided to keep the parameter-dependent overestimation within the GNSS part of DTRF2020 and not apply any weighting for GNSS. The estimated factor is published as additional information along with the DTRF2020 solution. The final DTRF2020 solution will include the consistently estimated station coordinates and EOP. It will be released in SINEX format along with further data on our new website <https://dtrf.dgfi.tum.de/>. The horizontal velocity field of DTRF2020 is shown in Fig. 1.13.

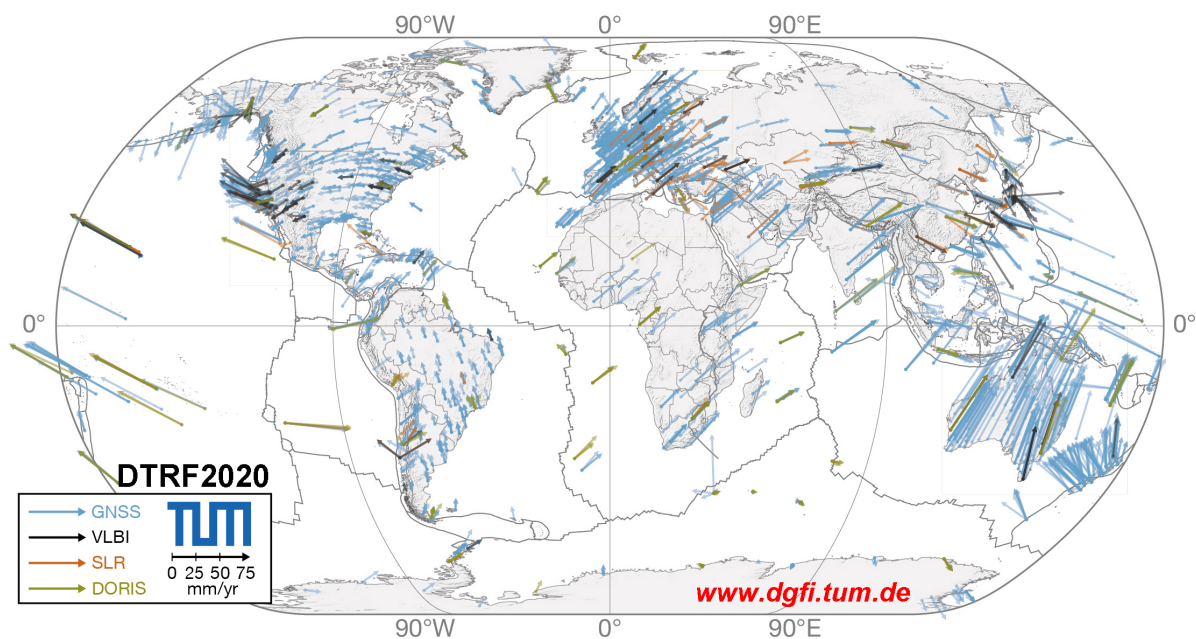


Figure 1.13: DTRF2020: horizontal velocity field.

Analysis of the DTRF2020

The agreement of DTRF2020 and ITRF2020 was investigated performing a 14-parameter similarity (Helmert) transformation. Results for translation and scale are given in Tab. 1.5. The best agreement for datum parameters was obtained for SLR, and the best agreement for network geometry (RMS) was obtained for GNSS. Scale differences in the order of a few millimeters (Tab. 1.5) were to be expected, since the scale of ITRF2020, in contrast to DTRF2020, is realized from a combination of VLBI and SLR scales. Finally, for the realized DTRF2020 datum (except for the DORIS scale), an agreement of about 5 mm and 0.15 mm/year can be observed.

¹⁶Bos M. et al. (2013): *Fast error analysis of continuous GNSS observations with missing data*. Journal of Geodesy, doi:10.1007/s00190-012-0605-0

Table 1.5: Translation and scale differences between DTRF2020 and ITRF2020 (ITRF2020 – DTRF2020) derived from a 14-parameter similarity transformation, epoch 2010.0.

		Tx	Ty	Tz	scale	RMS	# stat
GNSS	pos [mm]	1.7	-1.4	0.1	-4.0	0.3	104
	vel [mm/a]	-0.14	0.04	0.03	-0.09	0.05	
SLR	pos [mm]	0.4	-0.3	0.2	-2.0	3.1	29
	vel [mm/a]	0.05	-0.08	-0.01	-0.14	0.24	
VLBI	pos [mm]	2.8	-2.8	-3.1	-2.2	0.9	28
	vel [mm/a]	-0.02	-0.10	0.02	-0.14	0.10	
DORIS	pos [mm]	1.8	-4.5	-4.2	-6.4	0.8	20
	vel [mm/a]	-0.11	0.15	0.14	0.09	0.21	

DGFI-TUM combined EOP series were compared to IERS 14 C04, IERS 20 C04¹⁷ (which is identical to the ITRF2020 EOP series for the x-/y-pole from 1994–2021) and to the IERS Bulletin A time series. Furthermore, we compared them to the DTRF2014 EOP. Figure 1.14 shows the x-pole differences with respect to IERS 20 C04. WRMS values of all comparisons are given in Tab. 1.6. The highest agreement is obtained with respect to IERS 14 C04. However, all three Δ UT1 and LOD difference time series show a periodic signal of 13.66 days with an amplitude of about $38 \mu\text{s}$ and $7 \mu\text{s}/\text{d}$, respectively. The reason for the detected signals appears to be modeling differences between the DTRF2020 input data and the input data for the reference time series (e.g., in the EOP tidal model). The overall highest agreement is obtained with DTRF2014, with no significant periodic differences for Δ UT1 and LOD.

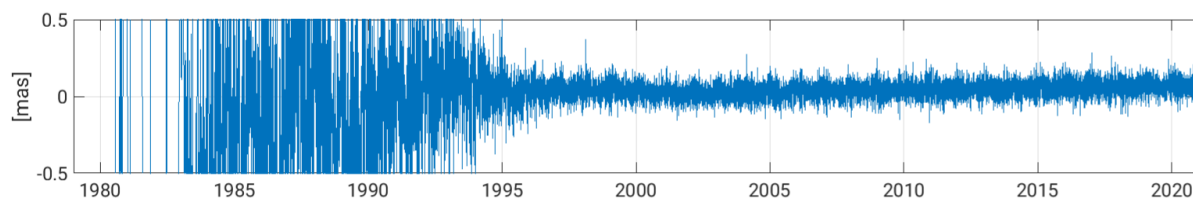


Figure 1.14: Difference time series of x-pole estimates of DTRF2020 with respect to IERS 20 C04 series.

Table 1.6: WRMS of difference time series of DTRF2020 EOP with respect to IERS 14 C04, IERS 20 C04 and IERS Bulletin A and with respect to DTRF2014 EOP. Bold numbers highlight the smallest WRMS values obtained (‘—’ means parameter not provided in reference time series).

	x-pole [mas]	y-pole [mas]	UT1 [ms]	dX [mas]	dY [mas]	x-pole rate [mas/d]	y-pole rate [mas/d]	LOD [ms/d]
14 C04	57.9	41.7	13.9	89.7	91.6	—	—	16.6
20 C04	60.0	56.7	13.9	87.6	94.5	225.7	309.7	20.4
Bull. A	73.2	59.5	13.9	105.0	111.7	—	—	16.0
DTRF2014	31.0	26.0	11.9	94.6	97.8	112.2	131.8	9.9

¹⁷<https://hpiers.obspm.fr/iers/eop/eopc04/eopc04.txt>

International Height Reference Frame (IHRF)

The International Height Reference System (IHRF) was introduced by the IAG in 2015 to provide a global standard for the precise determination of physical heights. The IHRF is based on the combination of a geometric component given by coordinates X referring to the ITRF, and a physical component given by the determination of potential values W^P at the positions $P(X)$ defined by the ITRF coordinates. The primary vertical coordinate is the geopotential number

$$-\Delta W^P = C^P = W^0 - W^P, \quad (1.1)$$

which may easily be converted to a metric physical height (orthometric or normal height). The IHRF vertical datum is realized by the equipotential surface of the Earth's gravity field defined by the conventional value $W_0 = 62,636,853.4 \text{ m}^2\text{s}^{-2}$. The International Height Reference Frame (IHRF) realizes the IHRF in two ways: physically, by a set of globally distributed reference stations, and mathematically, by the precise determination of potential values at these reference stations. Thanks to a strong international cooperation hosted by the IAG and led by DGFI-TUM, a first proposal for the IHRF reference network is completed.

Current efforts focus on the determination of the potential values at the global IHRF reference stations. An important advance in this regard is the comparison and evaluation of different methods for the computation of potential values. In the so-called Colorado Experiment¹⁸, 14 research groups from different countries computed geoid undulations, height anomalies, and potential values in Colorado (USA) using identical gravity and topography input data provided by the US National Geodetic Survey (NGS) but their own modeling strategies. The 14 solutions represent the state-of-the-art in precise regional gravity field modeling of high resolution, and the results of this experiment provide a basis for the calibration of the modeling methods.

Ongoing activities of DGFI-TUM are to coordinate the computation of potential values at the IHRF stations applying the same methods that have been used in the Colorado Experiment. Although the results show that the different methods produce similar results of up to 2 cm in terms of STDs, the most difficult challenge now is the assessment of reliable accuracy estimates of the potential values. In this regard, DGFI-TUM and TUM's Chair of Astronomical and Physical Geodesy are collaborating in the **DFG project Geo-H** (Enhanced Geopotential Field Modeling as Basis for the Establishment of Precise Height Systems):

- to improve the error budget quantification in the physical height determination,
- to develop new concepts and methods towards improved geopotential solutions and their accuracy assessment,
- to provide scientific guidelines for the realization of globally consistent geopotential-based height systems.

Geo-H is also set up as the appropriate platform to continue developing DGFI-TUM's radial basis functions' method for precise regional gravity field modeling. In 2022, DGFI-TUM developed a new approach based on the pyramid algorithm and sequential parameter estimation using a multi-resolution representation (MRR) to account for the varying spectral sensitivities of different observation techniques (Liu et al., 2022). This study represents the first successful realization of MRR in regional gravity field modeling, as the improvement achieved is 35 % and 23 % in the onshore area, and 63 % and 57 % in the offshore area, compared to the single-level approach and the MRR without pyramid algorithm, respectively. See Sect. 3.2 for more details.

¹⁸Wang Y.M., Sánchez L., ..., Liu Q., ..., Schmidt M., et al. (2021): *Colorado geoid computation experiment: overview and summary*. Journal of Geodesy, doi:10.1007/s00190-021-01567-9

GGOS Focus Area Unified Height System (GGOS-FA-UHS)

DGFI-TUM coordinates the GGOS Focus Area *Unified Height System* (GGOS-FA-UHS) since July 2015. The GGOS-FA-UHS was established in 2010 to lead and coordinate the efforts required for the establishment of a global unified height system that serves as a basis for the standardization of height systems worldwide. As previously published¹⁹, actions dedicated to investigate the best strategy for the implementation of the IHRF, the realization of the IHRF, were undertaken. In particular, a preliminary station selection for the IHRF reference network was achieved and different computation procedures for the determination of potential values as IHRF coordinates were evaluated. Ongoing activities of the GGOS-FA-UHS concentrate on:

- the determination of potential values at the IHRF reference stations,
- the refinement of standards, conventions, and guidelines to support a consistent determination of the IHRF at regional and national levels,
- the study of quality assessment methods in the determination of potential values and potential changes with time,
- the installation of an operational infrastructure within the International Gravity Field Service (IGFS) that ensures the maintenance and availability of the IHRF on a long-term basis. Fig. 1.15 summarizes the structure proposed by DGFI-TUM for the IHRF/IHRF.

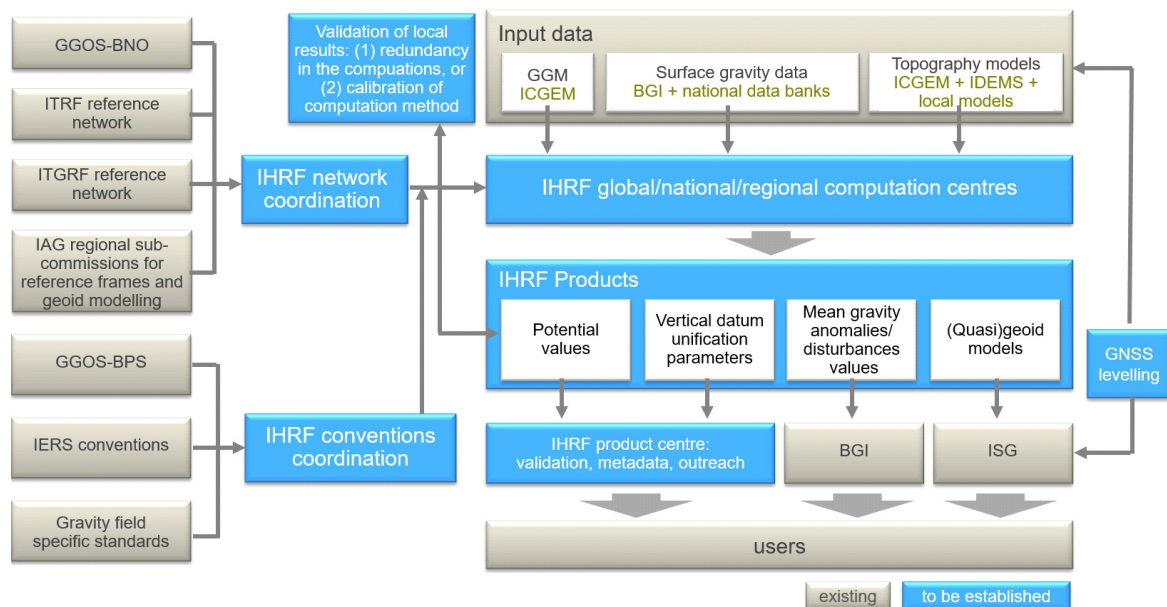


Figure 1.15: DGFI-TUM's proposal on the organizational structure to be installed within the International Gravity Field Service (IGFS) to ensure the long-term sustainability of the IHRF/IHRF.

¹⁹Sánchez L. et al. (2021): *Strategy for the realization of the International Height Reference System (IHRF)*. Journal of Geodesy, doi:10.1007/s00190-021-01481-0

Regional terrestrial reference frame in Latin America (SIRGAS)

Within the International GNSS Service (IGS), DGFI-TUM has been acting as the IGS Regional Network Associate Analysis Center for SIRGAS (RNAAC-SIR) since June 1996. The main objective of RNAAC-SIR is the development of analysis strategies to ensure the long-term stability of the regional terrestrial reference frame SIRGAS, the regional densification of the ITRF in Latin America. SIRGAS currently consists of about 500 continuously operating GNSS stations (GPS + GLONASS + GALILEO + BEIDOU), whose data are processed weekly by 10 ACs. DGFI-TUM's research in the context of SIRGAS is focused on (i) defining the best strategy for datum realization and observation combination within the regional TRF processing, (ii) improving the modeling and representation of the TRF kinematics to ensure a suitable transformation of station positions between pre- and post-seismic TRF realizations, and (iii) assessing non-linear station motions to improve the estimation of epoch-wise TRFs (ERFs).

DGFI-TUM's latest contribution to SIRGAS is the reference frame solution SIRGAS2022 (Sánchez et al., 2022). It is computed from weekly NEQs between January 2000 and April 2022 containing 584 stations with 1377 occupations. The final solution comprises station coordinates (positions and velocities), high-precision residual station position time series and, for the first time, PSD corrections (Fig. 1.16). SIRGAS2022 coordinates refer to the IGb14 TRF and are given at the epoch 2015.0. Their accuracy is estimated to be ± 0.8 mm in N/E and ± 1.4 mm in height at the reference epoch. The accuracy of the velocities is estimated to be ± 0.6 mm/yr in N/E and ± 1.0 mm/yr in height. The modeling and assimilation of seismic events remains a major challenge in the determination of the SIRGAS TRF. During this work, 793 discontinuities were detected (Fig. 1.17): 69 % are caused by antenna changes, 21 % correspond to co-seismic displacements and 10 % have unexplained causes. In addition, 75 % of the co-seismic displacements are followed by a strong post-seismic decay. In many cases (especially for stations in Argentina, Chile, Ecuador, Costa Rica), PSD effects of different earthquakes overlap, making it difficult to approximate the effects by a single logarithmic or exponential function. The situation is further complicated by the lack of data and malfunctioning or dismantling of earthquake-damaged stations, as these factors reduce the reliability and availability of station position time series. In some cases, the entire TRF of a country is affected by a single earthquake, meaning that after the earthquake, there is no reliable TRF for practical or scientific applications. This reduced reliability of regional TRFs is addressed with a novel approach for a direct geocentric datum realization of regional ERFs based on global networks (next Section).

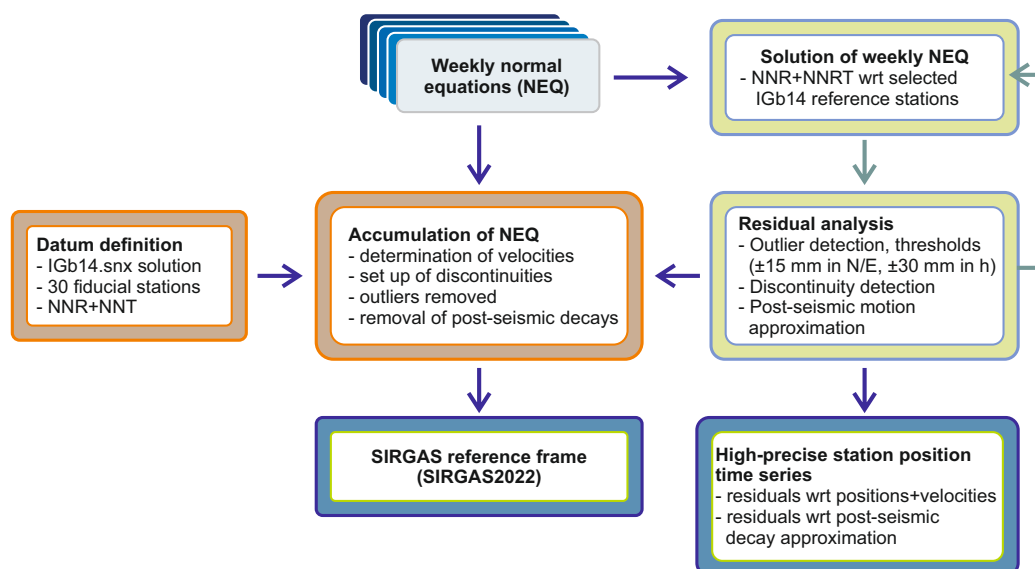


Figure 1.16: SIRGAS reference frame determination procedure (taken from Sánchez et al. 2022).

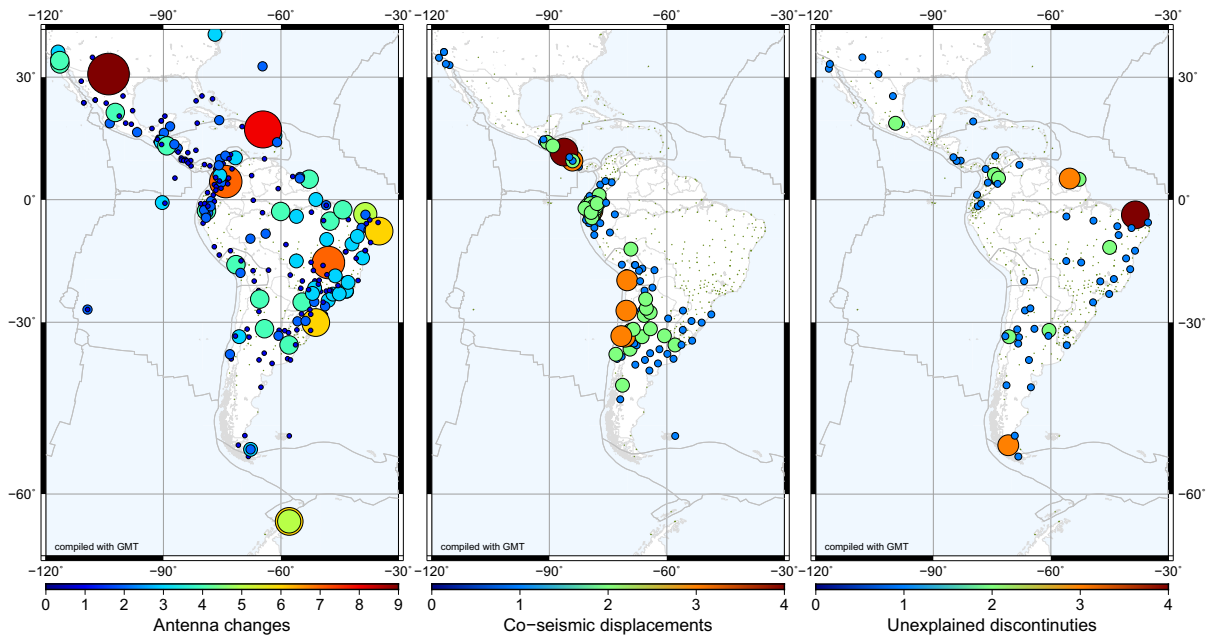


Figure 1.17: Time series discontinuities detected in SIRGAS2022: 69 % are caused by antenna changes (left), 21 % correspond to co-seismic displacements (center), and 10 % have unexplained causes (right).

Geocentric realization of regional Epoch Reference Frames (ERF)

The consistency of regional reference frames with the global geodetic datum is crucial to be able to relate geodetic observations of different types and from different networks and to analyze their observations in terms of geodynamics. DGFI-TUM has developed a methodology for the epoch-wise geocentric realization of regional reference frames, which allow to relate observed displacements directly to physical processes in the Earth system. In order to evaluate the reliability of the method, comprehensive analyses were carried out based on the realization of the Latin American reference frame SIRGAS.

The approach extends the regional GNSS network processed for SIRGAS with globally distributed IGS stations and combines this network with global SLR and VLBI networks on an epoch-by-epoch basis to perform an epoch-wise geocentric datum realization (Sánchez et al., 2022). The combination is performed at NEQ level, with a datum information filter applied prior to combination to the SLR and VLBI input data, the two techniques used to realize the physical datum parameters origin and scale (Kehm, 2022). The concept is to filter over short time periods (several weeks) to bridge observation gaps, where the filter assumes the positions of non-observing stations to be constant, but applies a stochastic filter model to capture possible unknown station motions within this time period. Stations that have not observed for longer periods are excluded from the filter as they can no longer contribute to reliable datum realization.

Validation against the JTRF2014, a high-precision geocentric sub-secular realization of the ITRS provided by NASA Jet Propulsion Laboratory (JPL), demonstrates that the realized datum has no systematic deficiencies in terms of geocentricity and its temporal evolution (Fig. 1.18). Comparisons with geophysical loading models of the Earth System Modelling Group at GFZ Potsdam show that the derived station displacement time series now directly reflect processes in a geocentric frame. This contrasts with conventional GNSS-only ERFs aligned to the global datum (such as SIRGAS), where the displacements reflect motions around the Earth's center of figure rather than its center of mass (Kehm, 2022; Kehm et al., 2022).

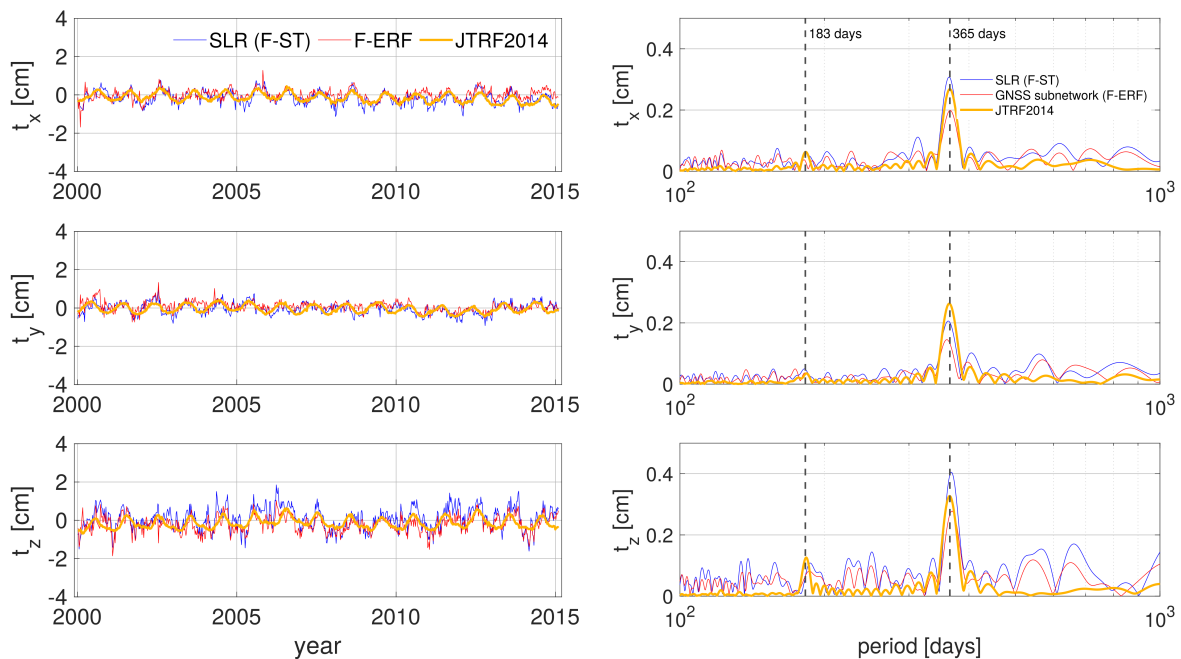


Figure 1.18: Helmer parameters with respect to ITRF2014 of (1) the filtered SLR single-technique solution (SLR F-ST, blue), (2) the GNSS sub-network of the filtered combined ERF solution (F-ERF, red), and (3) the JTRF2014 (orange). The left panels show the translations, the right panels show the respective spectra.

Consistent combination and prediction of Earth Orientation Parameters

Jointly with the Swiss Federal Institute of Technology (ETH) in Zürich, DGFI-TUM is investigating the potential of machine learning (ML) in generating highly precise rapid and predicted EOP²⁰. The investigations build on the results of the completed **project ESA-EOP** (Independent Generation of Earth Orientation Parameters), in which hindcast experiments were carried out to realize a consistently combined series of EOP²¹.

The procedure is based on a consistent and rigorous combination of geodetic space techniques to realize a highly precise final and rapid EOP determination. The time series is complemented by a prediction using effective angular momentum (EAM) data from the Earth System Modelling Group at GFZ Potsdam, several deterministic signals derived from the final-rapid EOP time series, and the last set of rapid combined EOP as initial values.

While a highly precise determination of the polar motion components from GNSS is possible, the hindcast experiments show the processing latency of 24-hour VLBI sessions as the limiting factor for the determination of $\Delta UT1$. Gaps between VLBI Intensive sessions have to be bridged solely by GNSS LOD, which requires a sophisticated treatment of the so-called GNSS LOD bias (Fig. 1.19). Validation of EOP predictions with ML trained on the final EOP from the ESA-EOP project against the realistic and ideal ESA hindcast scenarios suggests that ML-based approaches could become a valuable component to overcome current deficiencies.

²⁰Kiani-Shahvandi M. et al. (2022): *Neural ODE differential learning and its application in polar motion prediction*. Journal of Geophysical Research, Solid Earth, doi:10.1029/2022JB024775

²¹Kehm A., Hellmers H., Bloßfeld M., Dill R., Angermann D., Seitz F., et al. (2023): *Combination strategy for consistent final, rapid and predicted Earth rotation parameters*. Journal of Geodesy, doi:10.1007/s00190-022-01695-w

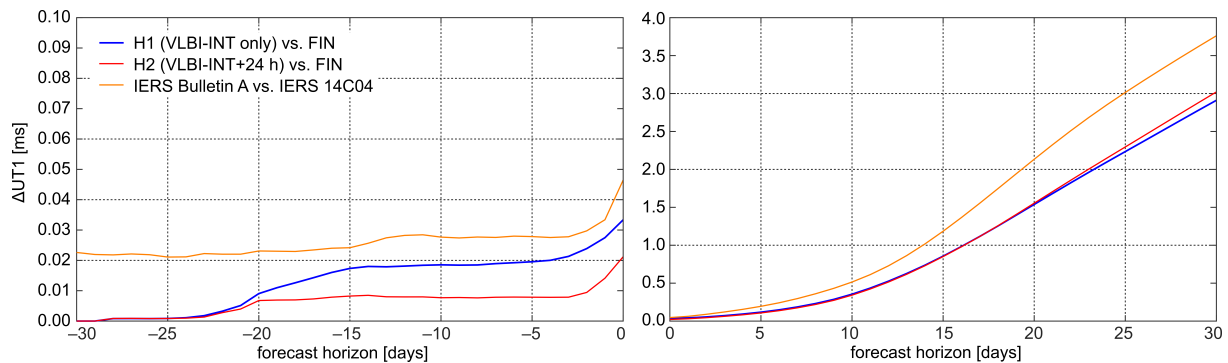


Figure 1.19: Comparison between the ‘optimal’ and the ‘realistic’ ESA-EOP hindcast scenarios for $\Delta UT1^{21}$. The ‘realistic’ scenario assumes only VLBI Intensives to be available within the rapid combination, while the ‘ideal’ scenario also includes 24-hour VLBI sessions. The RMS of each solution is given against the respective final ERP, i.e., ESA-EOP rapid/predicted vs. ESA-EOP final and IERS Bulletin A/finals.daily vs. IERS 14 C04. The ESA-EOP solution shows a seamless transition between final and rapid combination.

Related publications

Glomsda M., Bloßfeld M., Seitz M., Angermann D., Seitz F.: *Comparison of non-tidal loading data for application in a secular terrestrial reference frame*. Earth, Planets and Space, 74(1), doi:[10.1186/s40623-022-01634-1](https://doi.org/10.1186/s40623-022-01634-1), 2022

Hellmers H., Modiri S., Bachmann S., Thaller D., Bloßfeld M., Seitz M., Gipson J.: *Combined IVS Contribution to the ITRF2020*. In: Freymueller J., Sánchez L. (Eds.), IAG Symposia, Springer, doi:[10.1007/1345_2022_170](https://doi.org/10.1007/1345_2022_170), 2022

Kehm A.: *Strategies for the Realisation of Geocentric Regional Epoch Reference Frames*. Bayerische Akademie der Wissenschaften, DGK C 894, Dissertation, 2022

Kehm A., Sánchez L., Bloßfeld M., Seitz M., Drewes H., Angermann D., Seitz F.: *Combination Strategy for the Geocentric Realization of Regional Epoch Reference Frames*. Journal of Geophysical Research: Solid Earth, 127(10), doi:[10.1029/2021jb023880](https://doi.org/10.1029/2021jb023880), 2022

Kwak Y., Glomsda M., Angermann D., Gerstl M.: *Comparison and integration of CONT17 networks*. Journal of Geodesy, 96(5), doi:[10.1007/s00190-022-01610-3](https://doi.org/10.1007/s00190-022-01610-3), 2022

Liu Q., Schmidt M., Sánchez L.: *Combination of different observation types through a multi-resolution representation of the regional gravity field using the pyramid algorithm and parameter estimation*. Journal of Geodesy, 96(10), doi:[10.1007/s00190-022-01670-5](https://doi.org/10.1007/s00190-022-01670-5), 2022

Oelsmann J., Passaro M., Sánchez L., Dettmering D., Schwatke C., Seitz F.: *Bayesian modelling of piecewise trends and discontinuities to improve the estimation of coastal vertical land motion*. Journal of Geodesy, 96(9), doi:[10.1007/s00190-022-01645-6](https://doi.org/10.1007/s00190-022-01645-6), 2022

Sánchez L., Drewes H., Kehm A., Seitz M.: *SIRGAS reference frame analysis at DGFI-TUM*. Journal of Geodetic Science, 12(1), 92–119, doi:[10.1515/jogs-2022-0138](https://doi.org/10.1515/jogs-2022-0138), 2022

Seitz M., Bloßfeld M., Angermann D., Seitz F.: *DTRF2014: DGFI-TUM's ITRS realization 2014*. Advances in Space Research, 69(6), 2391–2420, doi:[10.1016/j.asr.2021.12.037](https://doi.org/10.1016/j.asr.2021.12.037), 2022

2 Research Area Satellite Altimetry

Satellite altimetry is the space-based technique for the precise measurement of the Earth's water surfaces. For more than 30 years, it has continuously monitored the ocean surface, including coastal regions and polar seas, and it provides measurement data on continental surface waters such as rivers and lakes. The most important measured variables are water levels and their changes. In addition, wave structures, surface currents, continental discharge and storage changes and many other oceanic and hydrological parameters can be determined. Satellite altimetry thus makes a substantial contribution to the understanding of the Essential Climate Variables (ECV) defined by the UN Global Climate Observing System (GCOS).

August 2022 marked the 30th anniversary of the launch of the NASA/CNES mission TOPEX/Poseidon. With this and several follow-up missions, high-precision measurements have thus been available on the same ground tracks for over three decades. These data are particularly important for long-term analyses of sea level and continental hydrology and now allow reliable interpretation of anthropogenic and climate-induced changes. But the long time series are also of great importance for the creation of ocean tide models, as they help to significantly reduce alias effects.

DGFI-TUM is working on advanced analysis methods to further improve the quality and applicability of altimetry observations for various phenomena of the oceanic and continental hydro-sphere. The focus is on combining measurement data from all available altimetry missions, which requires thorough harmonisation and calibration of the data (Sect. 2.1). In order to achieve optimal data use for various marine and inland applications, the institute operates the altimeter database OpenADB, through which derived datasets and scientific products are made available to the public. The combined multi-mission data are used for ocean research including coastal, shelf and polar regions (Sect. 2.2) and studies on continental hydrology (Sect. 2.3).

2.1 Multi-Mission Analysis

Global Multi-Mission-Crossover-Analysis MMXO22

At the end of 2022, there were eleven active satellite altimeter missions in orbit, and about as many have been completed over the past decades. In order to make the best possible use of the data from this large number of missions on different orbital tracks and with different instruments, and thus to optimize the spatial and temporal resolution of the measurement data, it is essential to combine the measurement data in a consistent way.

The prerequisite for such a multi-mission combination and joint data analysis is careful calibration and harmonisation in order to identify and eliminate possible systematic effects. In 2022, a recalculation of DGFI-TUM's global multi-mission crossover analysis²² was performed (MMXO22), based on uniform satellite orbits (all in ITRF2014) and the latest correction models, including DGFI-TUM's new ocean tide model EOT20. MMXO22 used Jason-3 as an absolute reference, and data from the Sentinel-6A mission was included for the first time. Using the calculated radial corrections, new versions of sea surface height (SSH) and sea level anomalies (SLA) were calculated. These form the basis of the DGFI-TUM scientific studies and are also made publicly available via OpenADB (openadb.dgfi.tum.de).

²²Bosch W., Dettmering D., Schwatke C. (2014): *Multi-mission cross-calibration of satellite altimeters: constructing a long-term data record for global and regional sea level change studies*. Remote Sens., doi:10.3390/rs6032255

Ionospheric correction to improve global mean sea level

Meaningful long-term measurements of sea level by satellite altimetry require precise atmospheric delay corrections to the range measurement. One of these corrections is the ionospheric correction, which takes into account the signal delays of the radar waves when interacting with free electrons in the Earth's ionosphere. Usually this correction is calculated from dual-frequency measurements of the altimeters themselves, but for single-frequency instruments or over coastal and inland regions, GNSS-derived corrections are often used. These are derived from Global Ionospheric Maps (GIM), which provide Total Vertical Electron Content (VTEC) up to a GNSS orbital altitude of about 20,000 km. For the application as altimeter correction, the plasmaspheric part of the signal (between the altitude of the altimeter orbit and the altitude of the GNSS orbit) has to be removed in a so-called downscaling approach.

Recently, it has been demonstrated that the downscaling method used in the generation of the official altimeter Geophysical Data Records (GDR) has been incorrectly implemented, leading to systematic errors in the GIM ionospheric corrections included in these datasets. The error is strongly dependent on solar activity and therefore exhibits significant long-term systematics leading to the erroneous estimation of Global Mean Sea Level (GMSL) trends. The trend error can reach up to 1 mm/year for the Jason-1 period and about 0.3 mm/year for the last two decades (1999-2021) (Dettmering and Schwatke, 2022).

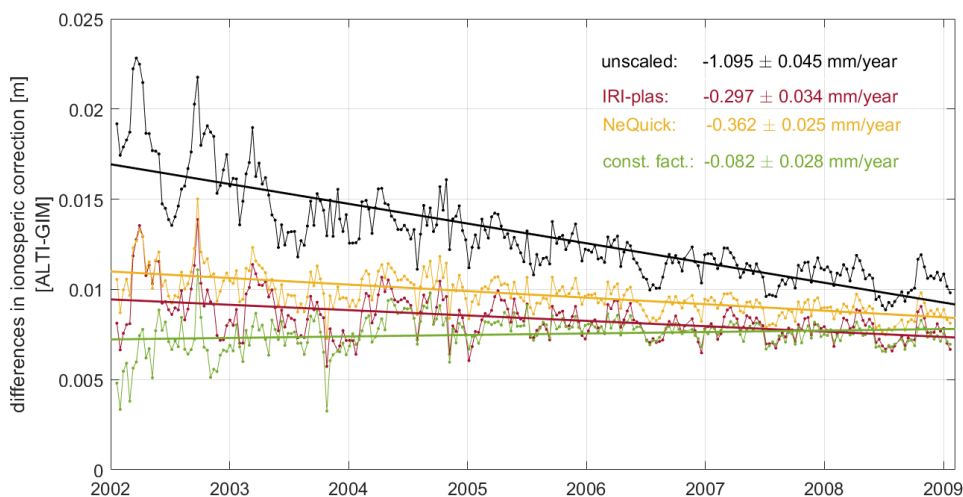


Figure 2.1: Trend differences for different scaling solutions with respect to smoothed dual-frequency altimeter data for Jason-1 mission

In a follow-up study²³, different methods and models for improved downscaling of GIM information were investigated. Using the Jason-1 mission as an example, two plasmasphere models were tested (IRI-Plas and NeQuick2), both of which reduce the error in sea level trends by about an order of magnitude, from about 1.0 to 0.3 mm/year. Even better results and at the same time simpler and faster is the use of a constant scaling factor, especially in times of low solar activity. This allows the sea level trend error to be reduced to below 0.1 mm/year for both Jason-1 (Fig. 2.1) and Sentinel-6A. In addition, a simple ML approach has been developed that shows promising results with similar accuracy, but has significantly higher processing capacity requirements.

²³Dettmering D., Schwatke C. (2023): *Comparison of different methods to account for the plasmaspheric electron content in GNSS-derived ionospheric altimeter corrections and their impact on sea level trend estimation*. Earth, Planets and Space, doi:10.1186/s40623-023-01764-0

Using satellite altimeter crossover differences for orbit validation

Within the framework of the **DFG project MEPODAS** (see Sect. 1.3), an extensive analysis of different orbit versions of numerous altimeter satellites was carried out to obtain information on the current and historical accuracy of the orbit determination¹³. Sea surface height differences at crossover points of the satellite tracks were used to determine the radial orbit accuracy and – through a multi-mission analysis – to identify geographically correlated errors and inconsistencies between missions. Using the Jason-2 satellite as an example, it was shown for the period 2008-2018 how the quality of the orbits improved with each new version, even if the improvements became smaller over time.

The same approach has been used to validate various orbit versions of the Sentinel-3A, Sentinel-3B and Sentinel-6A missions in the framework of the **ESA project CPOD** (Copernicus Precise Orbit Determination Service) to which DGFI-TUM has been contributing since 2020. Figure 2.2 illustrates selected results for Sentinel-6A orbits in 2022. Geographically correlated differences in orbit altitude for four different solutions from four different institutions compared to the CPOD combined solution are clearly visible. The orbits differ by large-scale patterns in the mm range, which has a direct impact on sea level determination.

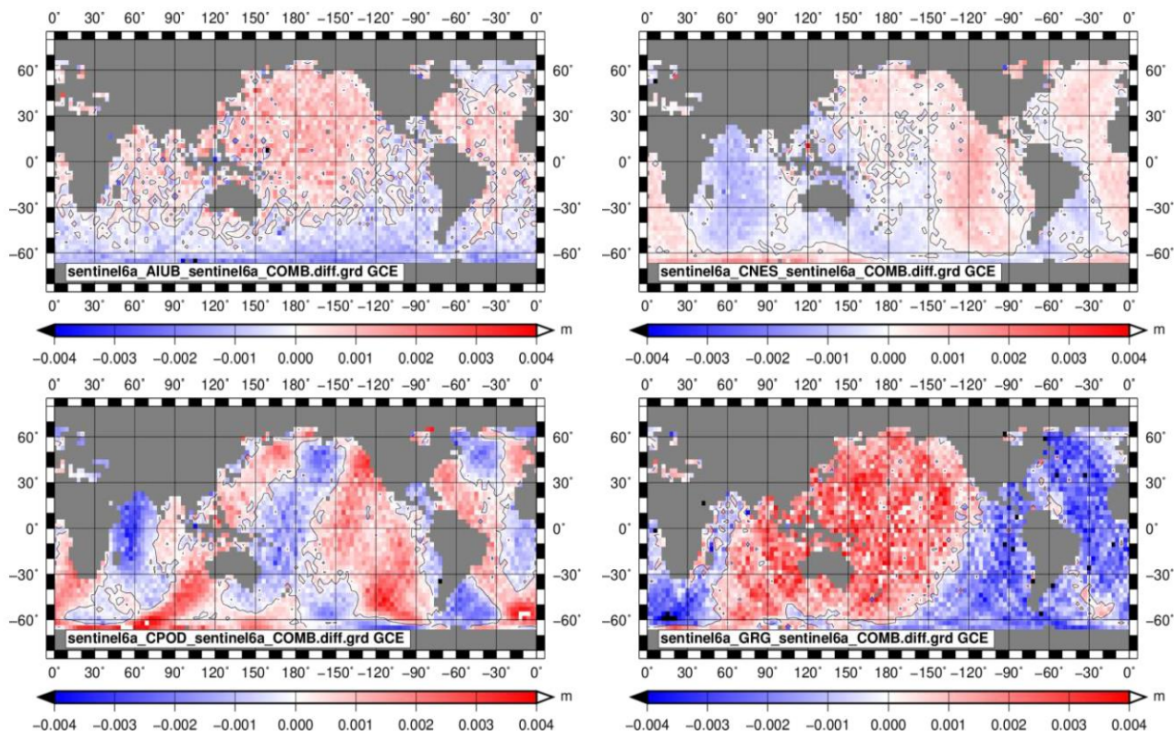


Figure 2.2: Geographically correlated orbit errors: differences of four orbit solutions (AIUB, CNES, CPOD, GRG) with respect to the CPOD Combined Solution (COMB).

2.2 Sea Surface

Analysis of SAR-altimetry signals over open ocean, coast and sea-ice

Sea level retrievals from the latest generation of radar altimeters (the SAR altimeters) are still challenging in the coastal zone and in areas covered by sea ice and require a dedicated analysis (retracking) strategy of the waveforms. In the framework of the **ESA project Baltic SEAL**, an empirical retracking strategy (ALES+ SAR), including a dedicated sea state bias correction, has been designed to improve the sea level observations in the Baltic Sea, characterized by a jagged coastline and seasonal sea ice coverage, without compromising the quality of open ocean data.

ALES+ SAR uses a mathematical formulation to describe the typical shape of the altimetric waveform. The mathematical formulation and the methodology of fitting a subwaveform of the signal is adapted from its LRM (low resolution mode) counterparts ALES²⁴ and ALES+²⁵, which avoid the contribution of the spurious reflections within the footprint. ALES+ is used for LRM waveforms, therefore the Brown-Hayne functional form physically describe the interaction between the radar pulse and the ocean surface. ALES+ SAR is instead an empirical retracker for SAR altimetry, because the same functional form is used to geometrically describe the waveform shape, but its parameters cannot be directly computed based on the physics of the measurement. Figure 2.3 shows three examples of ALES+ SAR fitting.

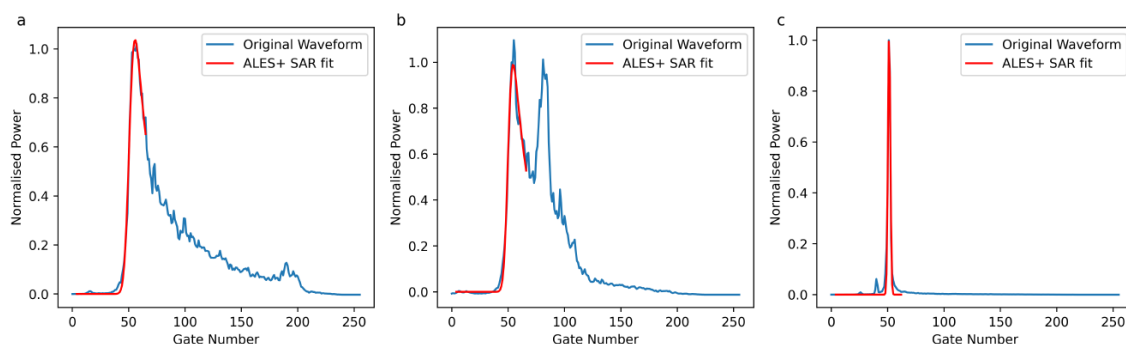


Figure 2.3: Three examples of ALES+ SAR fitting applied to a SAR altimetry waveform from a) typical open ocean conditions, b) coastal-like interference along the trailing edge and c) lead-like peaky leading edge.

In 2022, the retracker was extensively validated (Passaro et al., 2022). Its results were compared globally against the open-ocean official physical retracker of the Sentinel-3A mission (SAMOSA2) and, in the Baltic Sea, against a specific version adapted for the coastal zone (SAMOSA+). The main findings concerning the validation of these retrackers using Baltic Sea tide gauges (TG) as ground truth and computing the power spectral density (PSD) are described in the following.

The time series for the comparison against TG were formed by identifying the nearest ALES+ SAR along-track points to each TG within 30 km (from the TG) and both 0-3 km and 3-10 km away from the coast. The close proximity to the coast causes challenges for sea level estimations, which is also reflected in the results. ALES+ SAR, SAMOSA2 and SAMOSA+ all performed significantly better in the 3-10 km range than within the closest 0-3 km. However,

²⁴Passaro M. et al. (2014): *ALES: A multi-mission adaptive subwaveform retracker for coastal and open ocean altimetry*. Remote Sensing of Environment, doi:10.1016/j.rse.2014.02.008

²⁵Passaro M. et al. (2018): *ALES+: Adapting a homogenous ocean retracker for satellite altimetry to sea ice leads, coastal and inland waters*. Remote Sensing of Environment, doi:10.1016/j.rse.2018.02.074

within this close proximity to the coast, ALES+ SAR shows potential with correlation coefficient (r) of 0.5 and Root Mean Square Error (RMSE) of 35 cm. Although SAMOSA+ is able to produce the best correlation and RMSE in the 0-3 km range, the quality flag reduces the number of points down to a half when compared to the number of points achieved using the ALES+ SAR quality flag. In the 3-10 km range, ALES+ SAR outperforms SAMOSA+ and SAMOSA2 with an overall r of 0.7 and RMSE of 22 cm.

The PSD spectrum of the sea surface heights is compared with the one obtained using the SAMOSA2 ranges from the original product in Fig. 2.4. The spectral slope observed is comprised between k^{-2} and k^{-3} , which is inline with the global average observed in previous studies²⁶. ALES+ SAR PSD spectrum, as in the case of SAMOSA2, notably reduces the ‘spectral hump’ characterising the altimetry data from conventional altimetry for scales ranging from 30 to 100 km. Moreover, ALES+ SAR reaches a lower noise floor than SAMOSA2.

The results of this study show that ALES+ SAR is the first empirical retracker able to achieve results that are at least as good as the ones obtained by physical retrackerers in satellite altimetry, for any kind of oceanic returns. The ALES+ SAR fitting was applied to Cryosat-2 and Sentinel-3A data and cross-calibrated with older altimetry missions to produce the Baltic SEAL sea level dataset, which has been used for the analysis of trends²⁷ and sea level budget (Karimi et al., 2022) in the area.

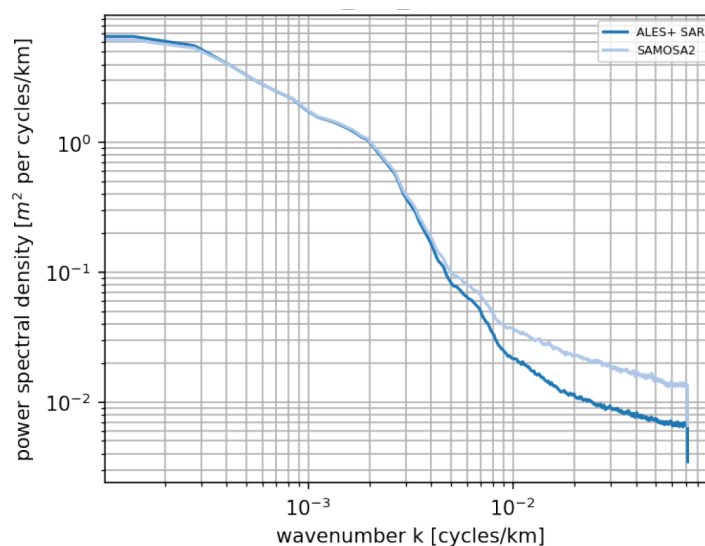


Figure 2.4: PSD spectrum of sea surface heights computed using ALES+ SAR and SAMOSA2. The spectrum is based on 8 full cycles (cycles 30 to 37) over the global ocean. To avoid outliers, points located closer than 20 km to the coast and sea level anomalies exceeding 2 m in absolute value are excluded.

Fully-focussed SAR processing for improved coastal wave height determination

Determining the three physical variables significant wave height (SWH), sea surface height, and wind speed from satellite altimetry continues to be challenging in the coastal zone because the received radar echoes exhibit significant interference from strongly reflective targets such as sandbanks, sheltered bays, ships etc.

²⁶Xu Y., Fu L. (2012): *The effects of altimeter instrument noise on the estimation of the wavenumber spectrum of sea surface height*. Journal of Physical Oceanography, doi:10.1175/JPO-D-12-0106.1

²⁷Passaro et al. (2021): *Absolute Baltic sea level trends in the satellite altimetry era: a revisit*. Frontiers in Marine Science, doi:10.3389/fmars.2021.647607

Fully focused synthetic aperture radar (FF-SAR) altimetry²⁸ is a novel processing technique exploiting the fully coherent processing of the received radar pulse echoes throughout the target illumination time. It exhibits a theoretical along-track resolution of up to less than half a metre. This suggests that the application of FF-SAR altimetry may give potential gains over unfocused SAR (UF-SAR) altimetry to resolve and mitigate small-scale interferers in the along-track direction to improve the accuracy and precision of the physical estimates.

A case study was carried out as part of a research collaboration with the Delft University of Technology with the objective to assess the applicability of FF-SAR-processed Sentinel-6 coastal altimetry data to obtain SWH estimates as close as possible to the coast²⁹. In this context, a multi-mission FF-SAR processor has been developed and the coastal retracking algorithm CORALv2 has been applied to estimate SWH (Schlembach et al., 2022). Different FF-SAR and UF-SAR processing configurations were assessed, as well as the baseline Level-2 product from EUMETSAT, by comparison with the coastal, high-resolution SWAN-Kuststrook wave model from the Deltares RWsOS North Sea operational forecasting system³⁰. Correlation, median offset, and the percentage of cycles with high correlation as a function of distance to the nearest coastline were evaluated. Moreover, the number of valid records and the L2 noise of the records was analyzed. Figure 2.5 shows the case study area comprising five coastal crossings of Sentinel-6 that are located along the Dutch coast and the German coast along the East Frisian Islands in the North Sea.

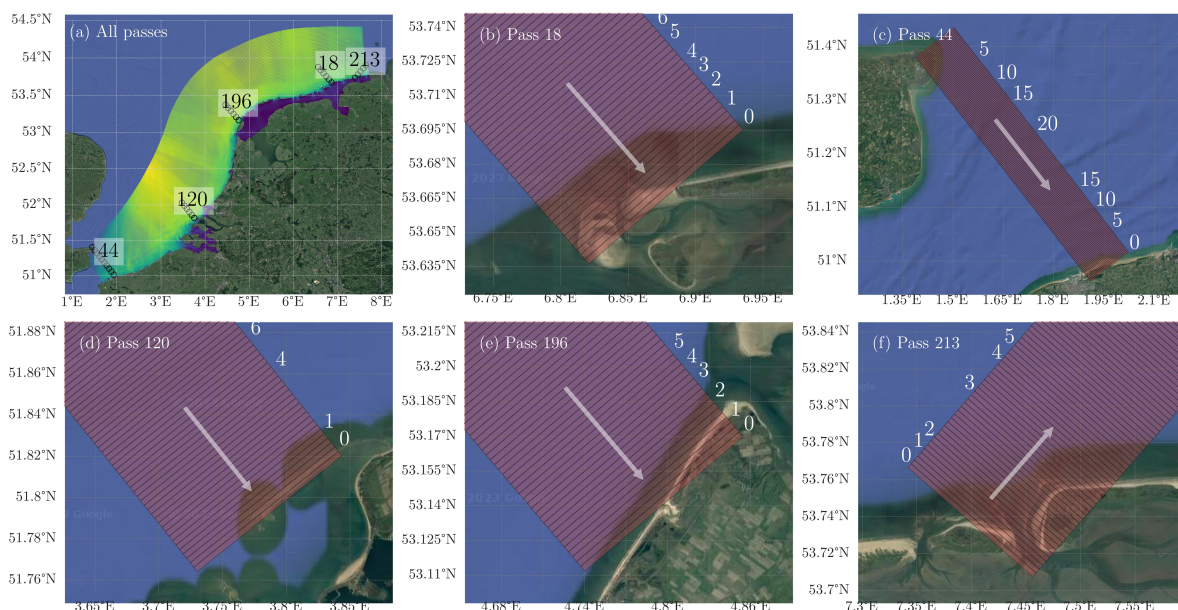


Figure 2.5: Panel a: Model domain of the SWAN-Kuststrook wave model with its curvilinear grid. Panels b, c, d, e and f display the Sentinel-6 passes 44, 120, 196, 18, and 213, respectively. White numbers next to each pass indicate the distance to coast in km, and the white arrows show the flight direction of the satellite. The estimated effective footprints have a size of 300x10000 m (along-track times across-track) and comprise the area on the ground that is estimated to have a major impact on the leading edge of the multilooked waveform, i.e. on the estimates of the physical variables (²⁹).

²⁸Egido A., Smith W. (2017): *Fully focused SAR altimetry: Theory and applications*. IEEE Trans. Geosci. Remote Sens., doi:10.1109/TGRS.2016.2607122

²⁹Schlembach F., Ehlers F., Kleinerherenbrink M., Passaro M., Dettmering D., Seitz F., Slobbe C. (2023): *Benefits of fully focused SAR altimetry to coastal wave height estimates: A case study in the North Sea*. Remote Sensing of Environment, doi:10.1016/j.rse.2023.113517

³⁰Booij et al. (1999): *A third-generation wave model for coastal regions: 1. Model description and validation*. Journal of Geophysical Research, Oceans, doi:10.1029/98JC02622

Figure 2.6 shows the results of the statistical analysis performed in this study. Accurate and precise SWH records can be determined in the nearshore zone within 1-3 km from the coast using satellite SAR altimetry. The FF-SAR-processed dataset with a Level-1b posting rate of 140 Hz show the greatest similarity with the wave model. A correlation of ~ 0.8 at 80% of valid records and a gain in precision of up to 29% of FF-SAR vs UF-SAR is achieved for 1-3 km from the coast. FF-SAR shows, for all cycles, a high correlation of greater than or equal to 0.8 for 1-3 km from the coast. The decay of SWH from offshore at 30 km to up to 1 km from the coast is estimated to amount to $26.4\% \pm 3.1\%$.

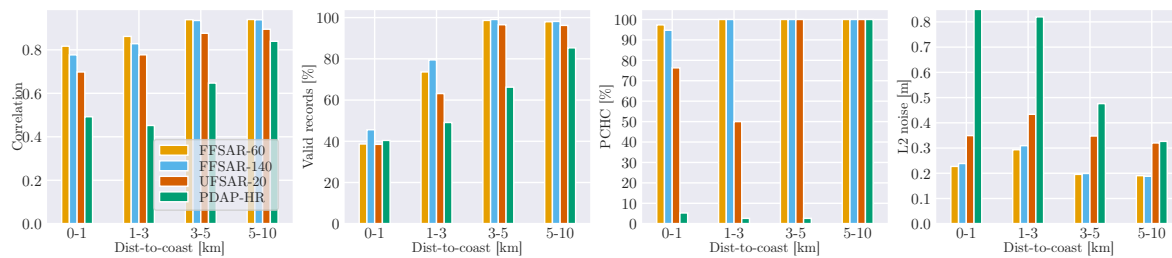


Figure 2.6: Statistical analysis of the SWH estimates for the FFSAR-60, FFSAR-140, UFSAR-20 and PDAP-HR datasets for all passes. Column panels show the Pearson correlation coefficients, the number of valid records, the median offset, PCHC and L2 noise in the distance to coast bands 0–1, 1–3, 3–5, and 5–10 km, respectively (²⁹).

Another joint study with the Delft University of Technology analytically analyzed the differences between UF-SAR and FF-SAR-processed waveforms to verify whether the UF-SAR SAMOSA2 waveform model can also be applied to the latter (Ehlers et al., 2022). It was shown that the FF-SAR waveforms are more similar to the UF-SAR-processed waveforms for Croysat-2 and Sentinel-3, so that the UF-SAR SAMOSA2 model can be used for retracking. In contrast, for Sentinel-6, the FF-SAR waveforms are more similar to the zero-Doppler beam of the SAMOSA2 model, which is recommended to be applied for retracking. This work allowed the application of FF-SAR processing in the coastal zone case study mentioned above²⁹.

Improved sea level and surface circulation in coastal and shelf ocean

Comprehensive ocean research demands sea level data continuous and homogeneous in time and space. The processing of this mapping often underlies interpolation methods and thus a loss of variability of the Sea Level Anomalies (SLA). This variability is of particular interest in coastal and continental shelf regions, where processes have higher variability on small scales.

The **DFG project CIRCOS** (Circulation from In-situ and Remote-sensing data in Coastal and Shelf ocean) is a collaboration of DGFI-TUM with partners at Scripps Institute of Oceanography in California and the Department of Atmospheric and Ocean Sciences of the University of Buenos Aires. CIRCOS aims to improve existing gridded sea level datasets in the Southwestern Atlantic Continental Shelf (SWACS) as study region. Specific coastal reprocessing is applied to along-track altimetry datasets, and improved gridding techniques are being developed and exploited. To enhance the temporal and spatial resolution, along-track satellite altimetry data will be combined with wind data, which are connected to SLA on different temporal scales.

In 2022, work of the project focused on exploring the impact of wind on SWACS. The study led to the conclusion that wind-driven SLA are found in the study region from daily to annual scales (Fig. 2.7) and could partly be connected to the shelf circulation through agreement with geostrophic velocities. Further, it was proven that the capability of the state-of-the-art gridded data to resolve SLA-variability is limited to >20 days, but wind data (e.g. remotely measured from scatterometers, available from CMEMS) provide variability in higher frequencies.

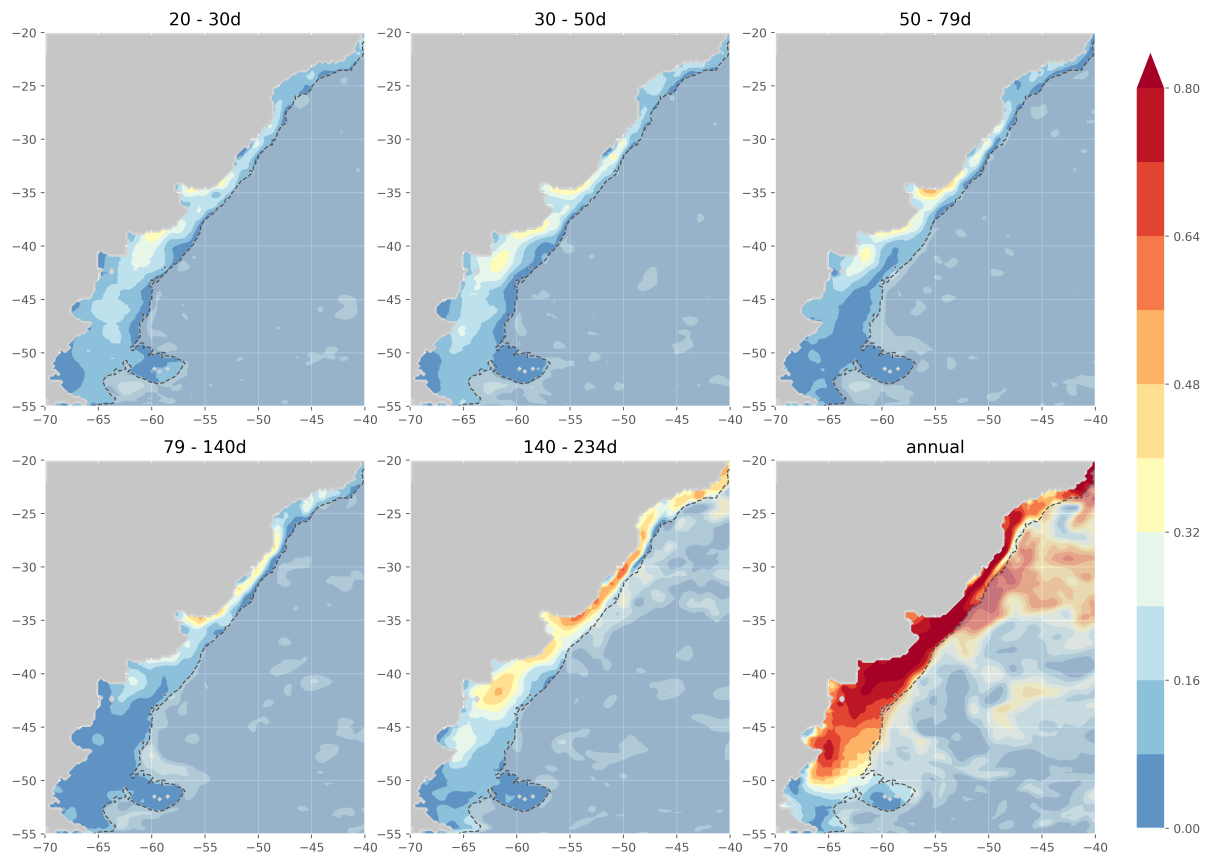


Figure 2.7: Mean coherence of SLA and along-shore wind speed over selected frequency bands in the Southwestern Atlantic Continental Shelf (SWACS).

Ongoing research within the project targets at the development of methodologies for mapping SLA on the SWACS to assess the most appropriate spatio-temporal interpolation methods to preserve fine scales of variability. So far, new studies at DGFI-TUM showed that besides conventional statistical approaches, machine learning using Random Forest is a powerful alternative for SLA mapping, with great potential for development³¹.

Lagrangian ocean analysis using particle tracking

In 2022, DGFI-TUM continued to develop its capabilities in Lagrangian ocean analysis using ocean particle tracking, i.e. the observation of motion of (virtual) particles within ocean datasets or numerical models.

Last year, a particle tracking software was developed³², which allowed for the use of virtual particle tracking in global ocean models in search and rescue applications. This tool, called LOST (Lagrangian Ocean Search Targets), was successfully implemented in several real-life applications and was continued to be developed in 2022 based on collaborations with institutions and agencies for which such a tool is crucial, for example rescue and salvage institutions. Based on the successful results of LOST and the continued community feedback, LOST placed second in an Ocean Hackathon³³ which resulted in a framework website being built. The proof of concept

³¹Passaro M., Juhl M.-C. (2023): *On the potential of mapping sea level anomalies from satellite altimetry with Random Forest Regression*. Ocean Dynamics, doi:[10.1007/s10236-023-01540-4](https://doi.org/10.1007/s10236-023-01540-4)

³²Hart-Davis M.G., Backeberg B. (2021): *Towards a particle trajectory modelling approach in support of South African search and rescue operations at sea*. J. Operational Oceanography, doi:[10.1080/1755876X.2021.1911485](https://doi.org/10.1080/1755876X.2021.1911485)

³³<https://ocean-innovation.africa/the-event/hackathon/>

in turn resulted in LOST being successfully granted cloud computing and storage infrastructure within the C-SCALE³⁴ project. This infrastructure will be used for further development within the next few years.

DGFI-TUM's particle tracking expertise was coupled with remote sensing and in-situ anthropogenic data to evaluate the vulnerability of the coastline of South Africa. Using particle tracking within a regional CROCO model, a coastal retention index (CORE) was developed to evaluate how long particles within the ocean remain in the coastal region. Figure 2.8 presents an example for the south coast of South Africa and shows correlation between the three different parameters estimated. This is crucial in terms of understanding how long pollutants such as sewage and plastics remain in coastal vicinity to evaluate the potential impact on the marine ecosystem (Pfaff et al., 2022). The study has contributed to the marine spatial planning of South Africa.

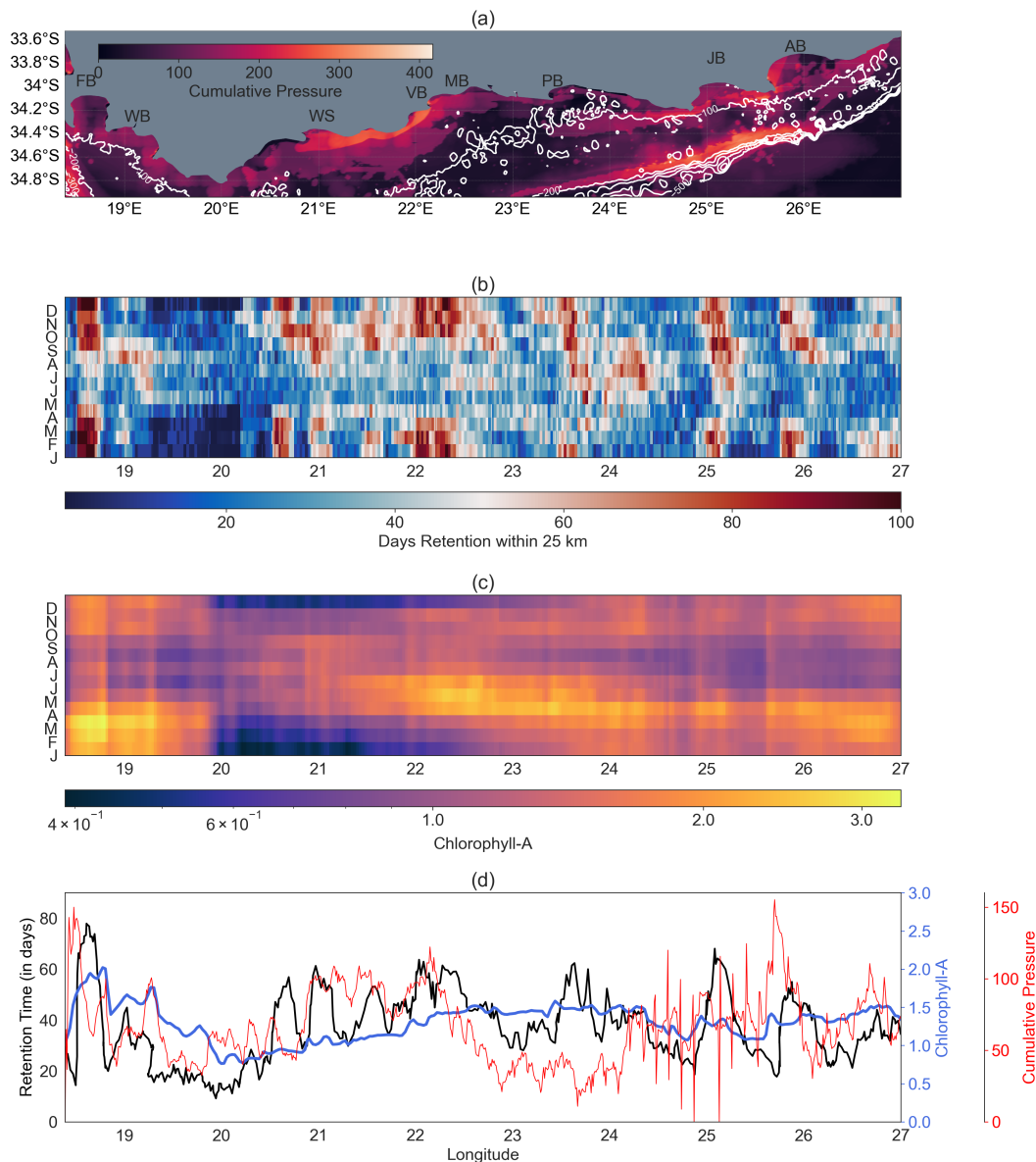


Figure 2.8: South coast: (a) cumulative anthropogenic pressure map (shading) and bathymetry (white lines; 100-m isobaths); (b) spatio-temporal coastal retention index (CORE); (c) spatio-temporal coastal chlorophyll-a; (d) longitudinal variability and relationships between long-term averages of CORE (black line), chlorophyll-a (blue line) Vleesbaai-Mossel Bay and decreasing again towards the east. From Pfaff et al. (2022)

³⁴<https://c-scale.eu/about/>

Another application of particle tracking was carried out in 2022 as part of a Master's Thesis. The main objective was to improve the understanding of the shelf circulation in the Natal Bight on the south-eastern coast of South Africa. A high-resolution 3D regional model, in-situ drifter observations and particle tracking experiments were used for the investigation. The study revealed the presence of a newly identified circulation feature, named the Natal Bight Coastal Counter-Current (NBC3). The overall circulation of this current is described by Heye et al. (2022). Virtual particle tracking has been used to demonstrate the importance of this current in terms of connectivity between marine protected areas in the region.

Empirical Ocean Tide Model EOT

Following on from the successful release of EOT20³⁵, the modelling capabilities of EOT have been further developed in line with the objectives of future global versions.

Developments in 2022 focused on improving the efficiency of the model processing, which was necessary with future plans to implement additional altimetry datasets, particularly with the Arctic and Antarctic regions in mind. This was aimed at improving the storage capability and processing time of all the altimetry data used within, which allowed for more frequent model runs at significantly less computational cost. Additionally, adjustments were made to the outlier detection and the flagging of sea level anomaly (SLA) data obtained from the satellite altimetry to improve the accuracy of the estimated constituents.

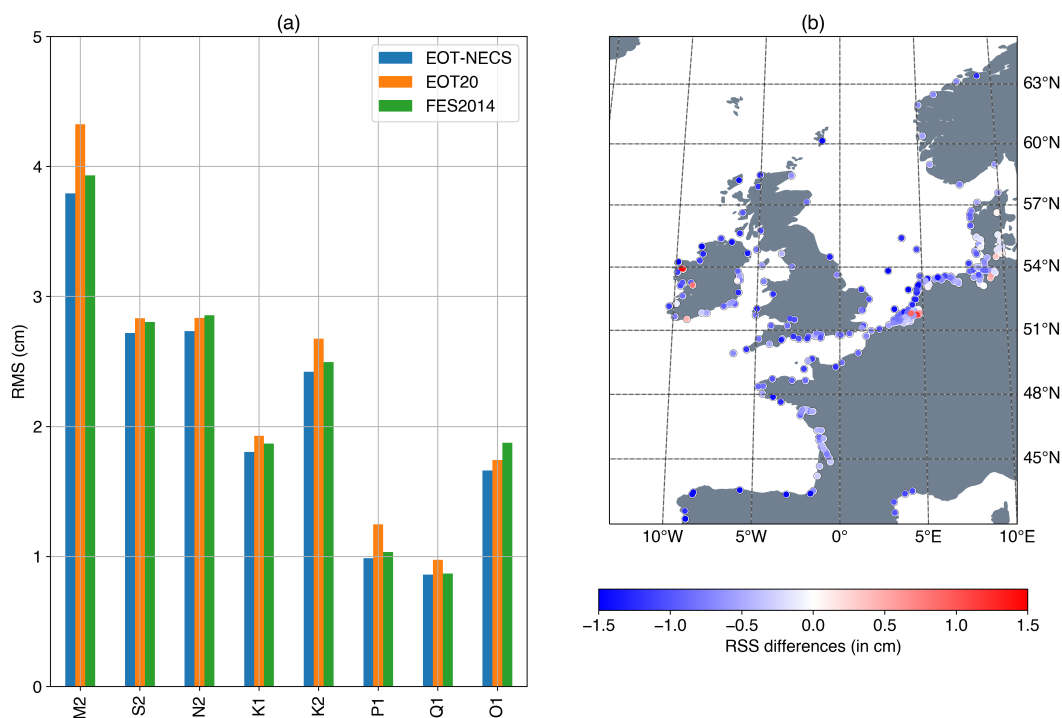


Figure 2.9: (a) RMS against 329 tide gauges in the North-West European Coastline of the eight major tidal constituents. (b) RSS difference between EOT20 compared to EOT-NECS. Red indicates a lower RSS for EOT-NECS and blue indicates a higher RSS.

³⁵Hart-Davis M.G. et al. (2021): EOT20: a global ocean tide model from multi-mission satellite altimetry. Earth System Science Data, doi:10.5194/essd-13-3869-2021

To evaluate these changes as well as to include additional altimetry data, a new regional EOT model for the North European Continental Sea (EOT-NECS) was developed³⁶. This model increased the number of altimeter missions from 11 in EOT20 to now 16 missions, with data extended to 2022 for any active mission. These inclusions resulted in a reduction in root-square-sum (RSS) error of the eight major tidal constituents relative to TICON-3 in-situ estimates (see below) by 0.42 cm relative to EOT20. This was also seen to be consistent throughout the region of interest (Fig. 2.9). The results are currently being used to force an operational ocean model to improve the predictability of water levels within the model.

The main focus of current EOT developments is to assess the impacts that altimetry corrections have on the tidal estimations, and to develop an optimal solution for the next global model. In collaboration with colleagues in USA and Norway, first investigations have assessed the impact of applying a mesoscale correction to tidal estimation in highly variable regions. These regions have been shown to have problems in determining tides from altimetry based on the contamination of tidal signals with those of submeso- and meso-scale processes. Initial experiments have shown an improved estimation of ocean tides in the order of centimeters and suggest positive implications for including such corrections in the model configuration (Fig. 2.10). Additional experiments are also ongoing for the ionospheric, dynamic atmospheric and the internal tide corrections.

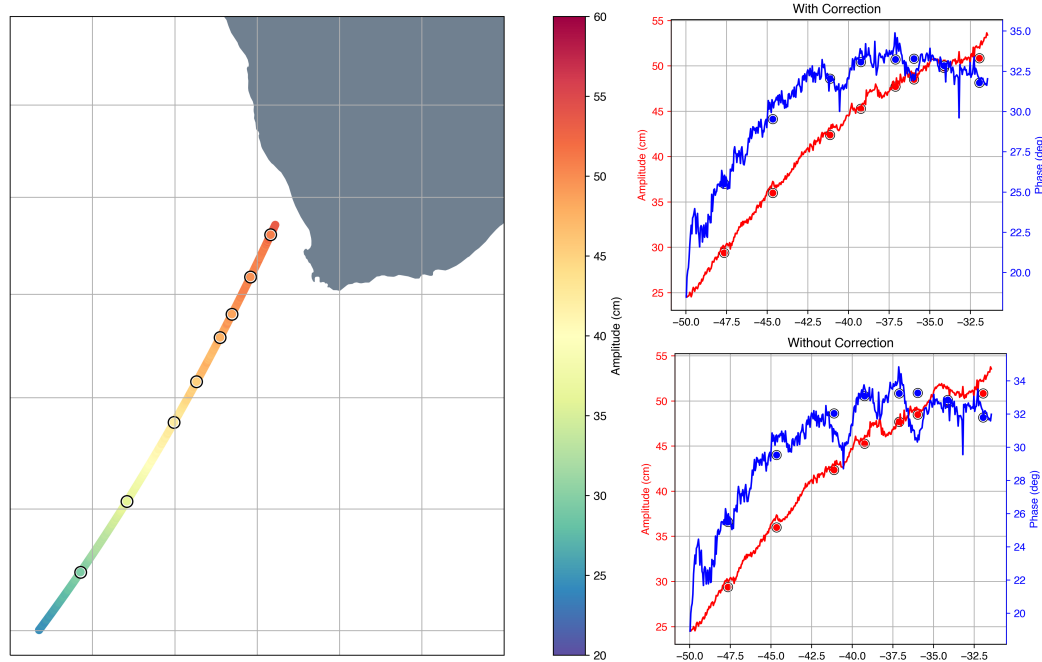


Figure 2.10: Along-track impact of including the mesoscale correction before making the tidal estimation estimated using 30 years of altimetry data from the Topex-Jason-Sentinel6a orbit.

³⁶Hart-Davis M.G. et al. (2023): *Altimetry-derived tide model for improved tide and water level forecasting along the European continental shelf*. Ocean Dynamics, in press.

Tidal constants from tide gauge stations

Within the **DFG project TIDUS** of the Research Unit 2736, NEROGRAV (New Refined Observations of Climate Change from Spaceborne Gravity Missions), two updated versions of the TICON (Tidal CONstants) dataset³⁷ were developed at DGFI-TUM. In the context of TIDUS, collaboration with colleagues at GFZ Potsdam and FU Berlin resulted in the need to incorporate additional third-degree tidal constituents in the validation of the TIME2021 numerical ocean tide model. This need resulted in the development of TICON-td (third-degree) based on producing four additional tidal constituents (3M_1 , 3M_3 , 3N_2 , 3L_2) into the dataset (Hart-Davis et al., 2022a).

Further developments focused on the reliable estimation of these tidal components, as they have very small signals and require relatively long time series to be reliably estimated. For this purpose, the length of the time series of the tide gauges used was limited to data with an observation period of more than 9 years. Compared to the original TICON dataset, this led to a significant reduction in the number of available tide gauges. Sulzbach et al. (2022) presented the first data-unconstrained global tidal atlas for these third degree tides and the use of the TICON-td dataset proved valuable in determining the level of accuracy of the model, which showed mean RMS values against the tide gauge database of 1 mm.

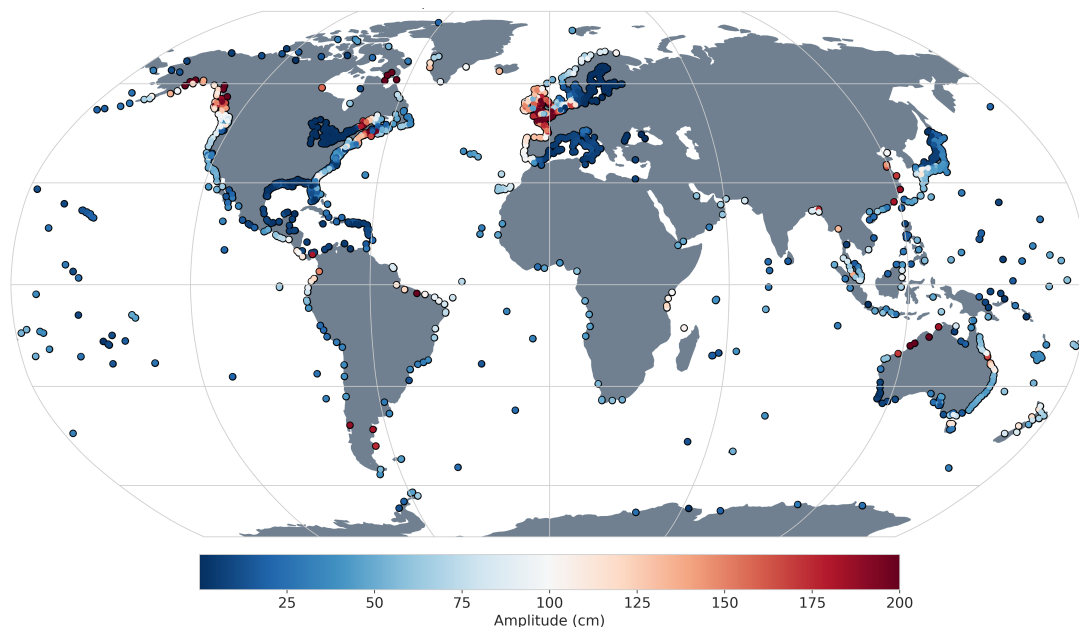


Figure 2.11: Global distribution of the TICON-3 dataset, demonstrating the amplitude of the M2 tide.

Towards the end of 2021, an update was made to the GESLA dataset (termed GESLA-3³⁸) which provides global in-situ tide gauge records for over 5,000 tide gauges. This prompted the update of our global TICON dataset (termed TICON-3) (Hart-Davis et al 2022b). Based on GESLA-3, additional processing steps have been implemented with TICON-3 to make the resultant tidal constituent estimations more reliable. This was done because some time series were limited to less than one year, which is not sufficient for the determination of certain constituents. An addition was made to the TICON-3 dataset to indicate whether tide gauges are in the coastal region or in rivers or lakes. Since the main objective of TICON is to validate tidal models, the identification of gauge positions is crucial for determining the suitability of certain constituents for model validations. Figure 2.11 shows the global distribution of TICON-3.

³⁷Piccioni G. et al. (2019): *TICON: Tidal CONstants based on GESLA sea-level records from globally located tide gauges*. Geoscience Data Journal, doi:[10.1002/gdj3.72](https://doi.org/10.1002/gdj3.72)

³⁸Haigh I. et al. (2022): *GESLA Version 3: A major update to the global higher-frequency sea-level dataset*. Geoscience Data Journal, doi:[10.1002/gdj3.174](https://doi.org/10.1002/gdj3.174)

Arctic thin ice

Openings in the polar sea ice cover, so-called polynyas or leads, are of great importance for the heat exchange between ocean and atmosphere. However, they are not permanently open, but can be partially frozen and covered by a thin layer of ice up to a thickness of about 25-30 cm. The surface temperature of the so-called thin ice lies between that of open water and that of thicker sea ice, which modulates the heat exchange between ocean and atmosphere. This modulation must be taken into account in climate modelling or prediction, for example.

In order to be able to detect water openings and thin ice areas via satellite altimetry data, DGFI-TUM has further developed its unsupervised classification algorithm³⁹ and adapted it for use with all altimeter missions. In particular, within the **IGSSE project AROCCIE** (Arctic Ocean Surface Circulation in a Changing Climate and its Possible Impact on Europe), SAR altimeter missions such as Sentinel-3 or CryoSat-2 have been included in addition to conventional (LRM) altimeter missions. The unsupervised classification enables the detection of open water surfaces and improved determination of sea surface height in the polar oceans. Now, the classification based on Cryosat-2 SAR observations has been advanced for the detection of thin ice surfaces. Individual waveform clusters were studied in terms of their physical and backscattering properties in relation to thin ice. With this new surface information, thin ice maps have been created for the Arctic, showing the temporal and spatial evolution of thin ice formation.

In collaboration with the Alfred Wegener Institute (AWI), further analyses and comparisons of the thin ice areas detected by Cryosat-2 with MODIS thermal images are being carried out. To support this comparison visually, additional image data from Sentinel-1 are used. Thin ice thickness data are calculated from MODIS ice surface temperatures derived from MOD/MYD02 standard radiance data using the surface-energy-balance model together with atmospheric re-analysis data from ERA5⁴⁰. As MODIS operates in the infrared spectrum, suitable overflights are manually checked for cloud artefacts and suitability. All comparisons take place within 30 minutes of a Cryosat-2 overflight to minimize the influence of sea ice drift and rapidly changing temperatures. Figure 2.12 shows a comparison of all three sensors.

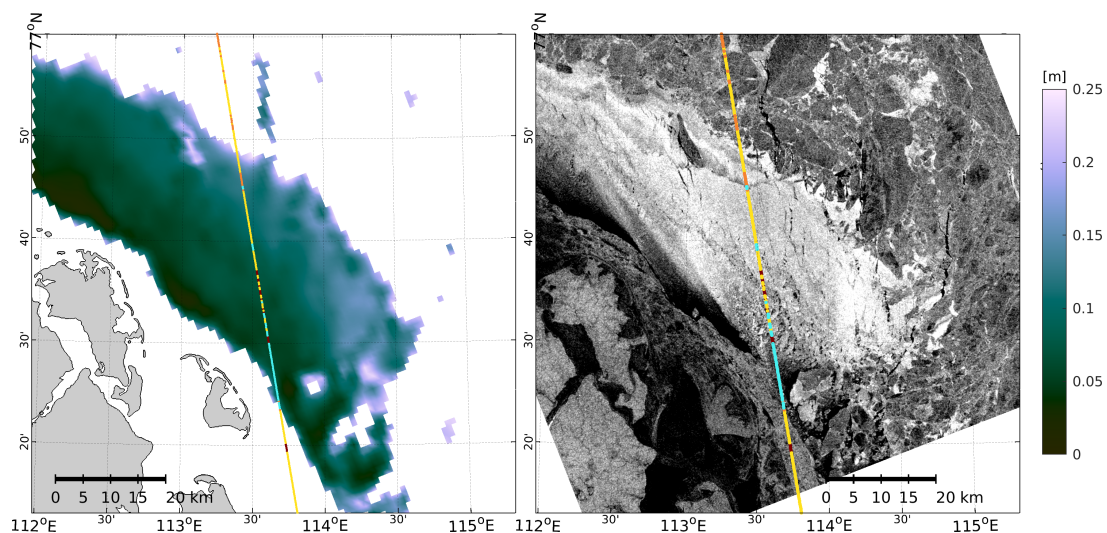


Figure 2.12: Near-simultaneous comparison of classified Cryosat-2 waveforms with MODIS thin-ice thickness (left) and the Sentinel-1A SAR image (right) with time differences of 7 min. (MODIS) and 24 min. (Sentinel-1A). Cyan classifications indicate leads, orange thin-ice, yellow sea-ice and brown undefined surfaces (⁴¹).

³⁹Müller F.L. et al. (2017): *Monitoring the Arctic Seas: How satellite altimetry can be used to detect open water in sea-ice regions*. Remote Sensing, doi:[10.3390/rs9060551](https://doi.org/10.3390/rs9060551)

⁴⁰Paul S. et al. (2015): *Long-term coastal-polynya dynamics in the southern Weddell Sea from MODIS thermal-infrared imagery*. The Cryosphere, doi:[10.5194/tc-9-2027-2015](https://doi.org/10.5194/tc-9-2027-2015)

The comparison includes about 21.000 Cryosat-2 observations and 161 MODIS scenes from the Laptev Sea during the winter months of January to March from 2011 to 2020⁴¹. In addition to a generally good agreement between the MODIS-derived thickness of thin ice and the CryoSat-2 waveform classification, a strong linear dependence of most of the used CryoSat-2 waveform parameters on the thickness of thin ice (up to 25 cm) is observed (Fig. 2.13). This is particularly visible for the Maximum Power (MP) and the Waveform width (Wwidth). This offers the possibility to improve sea level determination by providing altimeter corrections to account for thin ice layers or by adapting retracking algorithms specifically for very thin sea ice.

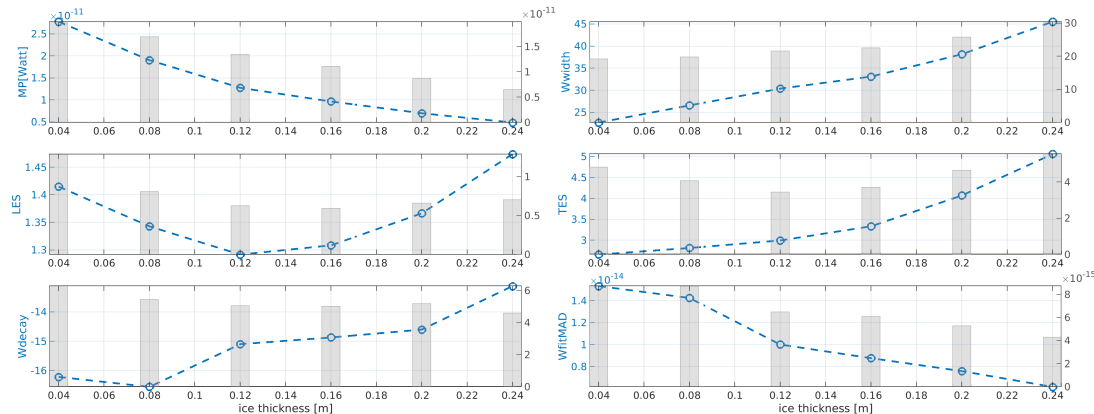


Figure 2.13: Shape and power features from the unsupervised classification of altimeter waveforms versus binned ($\pm 2\text{cm}$) thin-ice thickness from MODIS. Blue circles show mean feature values with corresponding standard deviations in grey.

Vertical land motion from coastal altimetry and tide gauge observations

The change in sea level relative to the coast is influenced by two effects: on the one hand, by absolute changes in sea level and, on the other hand, by the uplift or subsidence of the land (Vertical Land Motion, VLM) along the coastlines. While the global absolute sea level can today be observed even near the coast with increasing accuracy via satellite altimetry measurements using dedicated analysis methods, the VLM is subject to very large uncertainties in wide areas.

In the frame of the **ESA Climate Change Initiative (CCI) Sea Level project**, DGFI-TUM is involved in the determination of a novel altimetry-based global coastal sea level dataset (Cazenave et al., 2022). Also within this project, DGFI-TUM is exploring methods to create a global VLM dataset based on differences between tide gauge and altimetry observations (SATTG) optimized for the coastal zone. In addition to improved VLM, the project will provide an interpolated map of the uncertainties of the VLM estimates for different regions. This interpolation is performed using Bayesian transdimensional regression⁴², an approach which directly estimates the smoothness of the interpolation based on the spatial distribution, formal uncertainties, and spatial variance of the data. These activities strongly benefit from the algorithms developed within the **DFG project VLAD** (Vertical Land motion by satellite Altimetry and tide gauge Difference). Next to the generation of VLM information also a comprehensive performance analysis of different altimetry datasets (SLcci XTRACK, OpenADB multi-mission altimetry, and gridded data) in terms of correlation, RMS and trend differences in the coastal zone with regards to tide gauge observations is carried out.

⁴¹Müller F.L., Paul S., Hendricks S., Dettmering D. (2023): *Monitoring Arctic thin ice: a comparison between CryoSat-2 SAR altimetry data and MODIS thermal-infrared imagery*. The Cryosphere, doi:10.5194/tc-17-809-2023

⁴²Hawkins R. et al. (2019): *Trans-dimensional surface reconstruction with different classes of parameterization*. Geochemistry, Geophysics, Geosystems, doi:10.1029/2018GC008022

The interpolated VLM map for Europe is shown in Figures 2.14 and 2.15a. A clear GIA (Glacial Isostatic Adjustment)-related uplift towards Scandinavia is visible, as well as subsidence between 1-2 mm/year in central and western Europe, linked to the known GIA fore-bulge collapse. A high regional variability in the pointwise VLM rates along the English coastlines can be found, which is partly associated with high formal uncertainties. This can be explained by lower correlations of altimetry and TGs in this region. The Bayesian regression incorporates the high formal uncertainties of the data and thus yields a smooth interpolated VLM surface in this area, despite the high local variance of VLM.

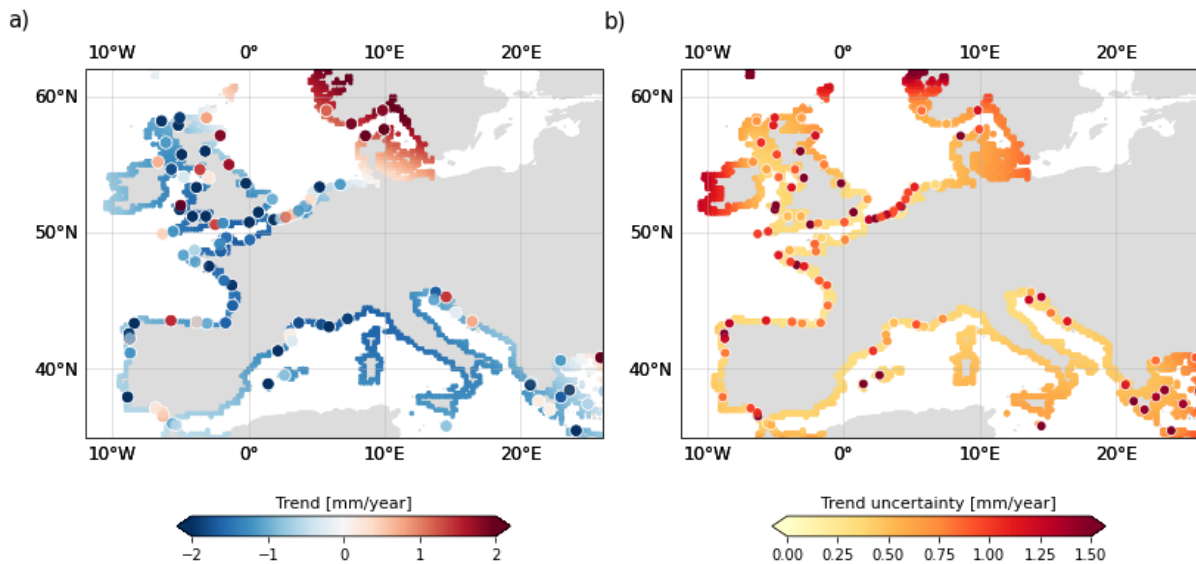


Figure 2.14: Continuous VLM (a) and uncertainties (b) along the European coastline. In addition to the continuous interpolated estimate, SATTG VLM and uncertainties are shown (white edge-colours).

For Australia (Figure 2.15b), the coastlines are affected by subsidence between 1-2 mm/year. Similar as for the English coastline, VLM and uncertainty estimates have higher variance in areas that are associated with a lower correlation of altimetry and TGs (not shown). That particularly affects the north-eastern Australian coastline, or the region north of Brisbane. Overall,

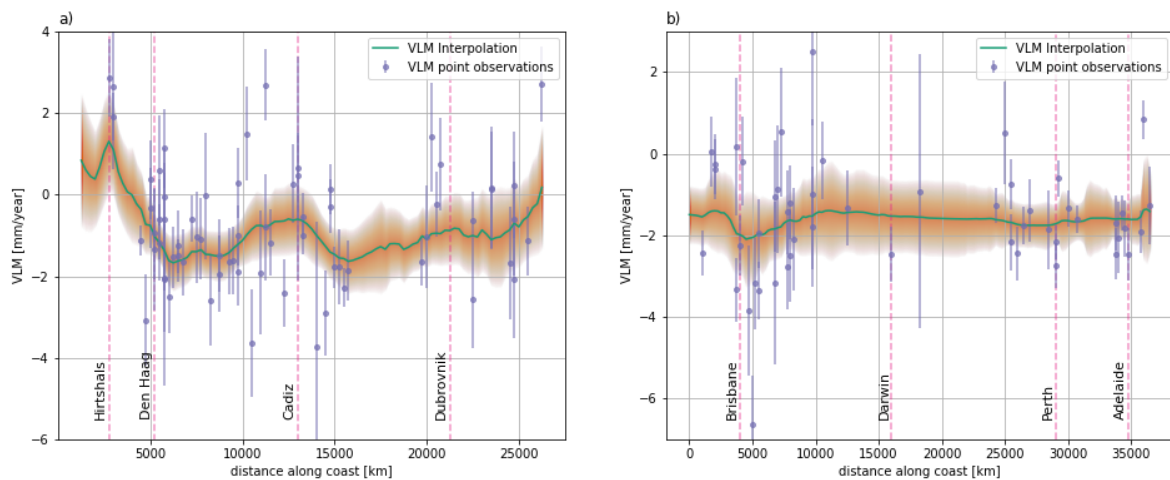


Figure 2.15: Continuous VLM and uncertainties along the European (a) and Australian (b) coastlines. The green line shows the posterior mean estimate, the orange shading encapsulates the 2-sigma confidence intervals of the interpolated VLM. SATTG VLM and uncertainties are shown in purple.

the subsidence found for the Australian coastline, as well as the Philippines (not shown), for instance, are in accordance with previous research using GNSS data⁴³. However, observed subsidence in Australia disagrees with VLM based on GIA which underlines the relevance of observed VLM to obtain continental-scale VLM processes unrelated to GIA.

The project demonstrates that VLM from SATTG can serve as an essential complementary information source to densify the existing network of GNSS stations. However, as SATTG is still associated with a lower precision and accuracy than GNSS data, extending the database by GNSS observations and increasing the number of observations in time can strongly increase the robustness of the results and enhance the resolution of VLM processes.

Relative sea level projections by vertical land motion reconstructions

A major result of the above mentioned **DFG project VLAD** (Vertical Land motion by satellite Altimetry and tide gauge Difference) is a global reconstruction of spatially and temporally varying VLM for 1995-2020. The reconstruction maximizes temporal and spatial resolution of observed VLM processes in a Bayesian framework and is based on a comprehensive database of more than 10,000 GNSS, altimetry and tide gauge time series that have been carefully cleaned of discontinuities and trend changes beforehand (Oelsmann et al., 2022).

While mechanisms such as GIA are associated with large-scale linear motions that persist over millennia, other processes such as tectonic activity, changes in surface loading or human activity can cause responses with much smaller spatial scales and non-linear temporal behavior. Current relative sea level (RSL) projections of the 6th Assessment Report of the Intergovernmental Panel on Climate Change (IPCC)⁴⁴ do not yet include VLM estimates from direct observations, nor rigorously model the uncertainties associated with non-linear VLM. VLAD used the novel VLM reconstruction to reconcile the projected RSL changes and uncertainties in 2150. To quantify the different contributions of absolute SL change and VLM to projected coastal relative sea level, the outputs of the Coupled Model Intercomparison Project Phase 6 (CMIP6)⁴⁵ under the SSP2-4.5 scenario⁴⁶ were used. The projected absolute coastal sea level was combined with the long-term linear trends and uncertainties of the VLM reconstruction.

Figure 2.16 displays different projected local relative SL change estimates based on both the VLM reconstruction and GIA model at six different locations (A-C and F-H). GIA-induced uplift and subsidence strongly contribute to future sea level in the Bothnian Bay (Skellefteå) and the eastern US coast (New York), which is consistent with our VLM reconstruction. Discrepancies between relative SL projections can be found in areas affected by localized subsidence (e.g., Venice, Gulf of Mexico, Nile Delta) or in regions impacted by high tectonic activity (western South America, Japan). Thus, unresolved processes in GIA models inevitably contribute to regional deviations of relative SL change projections.

Figure 2.16E illustrates the regional future RSL change as well as its deviation from the global mean SL rise (0.8 m in 2150), obtained as the median of the ensemble model outputs. Bars depicting the VLM component indicate its estimated contribution to RSL change. The absolute explained spatial variance (i.e., the variance of the deviations from the global mean) of coastal RSL change by VLM is projected to about 22% in 2150 along the world's coastlines, where

⁴³Hammond W. et al. (2021): *GPS Imaging of global vertical land motion for studies of sea level rise*. Journal of Geophysical Research, Solid Earth, doi:[10.1029/2021JB022355](https://doi.org/10.1029/2021JB022355)

⁴⁴Fox-Kemper B. et al. (2021): *Ocean, cryosphere and sea level change*. *Climate Change 2021: The Physical Science Basis. Contribution of Working Group I to the 6th AR of the IPCC*, doi:[10.1017/9781009157896.011](https://doi.org/10.1017/9781009157896.011)

⁴⁵Eyring V. et al. (2016): *Overview of the Coupled Model Intercomparison Project Phase 6 (CMIP6) experimental design and organization*. Geoscientific Model Development, doi:[10.5194/gmd-9-1937-2016](https://doi.org/10.5194/gmd-9-1937-2016)

⁴⁶O'Neill B. et al. (2016): *The Scenario Model Intercomparison Project (ScenarioMIP) for CMIP6*. Geoscientific Model Development, doi:[10.5194/gmd-9-3461-2016](https://doi.org/10.5194/gmd-9-3461-2016)

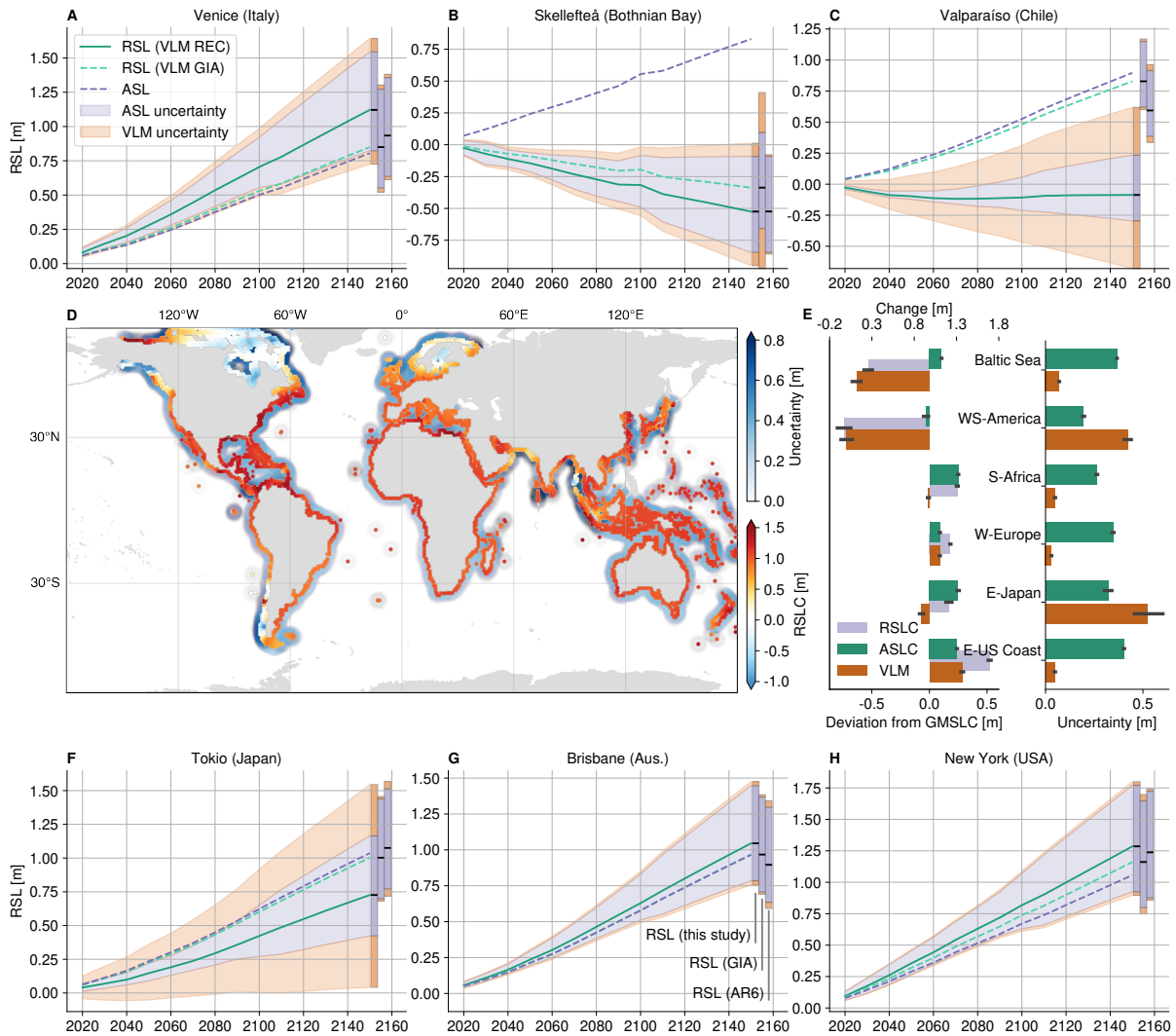


Figure 2.16: Global and regional projected RSL change based on IPCC AR6 projections (SSP2-4.5 scenario), VLM reconstruction, and GIA model. A-C and F-H: RSL change based on VLM-reconstruction (solid teal line) or GIA model (dashed teal line) from 2020-2150. The absolute projected SL change is depicted by the blue dashed line and consists of the contributions of ice sheets, glaciers, land water storage, and ocean dynamics. Uncertainty contributions of the 1σ absolute SL change uncertainties and VLM (blue and orange shading) add up to the combined RSL change uncertainties. D: coastal projected RSL change and the combined uncertainties (blue shading) of absolute SL projections and VLM reconstruction. E: different contributors of RSL change and uncertainties for different regions; Oelmann et al., 2022.

coastal SL change is by implication strongly dominated by the increased mean absolute SL rise. However, on a regional scale, VLM plays a predominant role in future SL change. VLM will explain 51% of the spatial variance of the RSL deviations from the global mean in 2150. The regional impact of VLM is thus of the same magnitude as the combined responses to ocean dynamics and mass change, causing a much larger range in projected RSL rates (from -1 m to 1.5 m change in 2150), than the absolute SL change alone (0 m to 1.1 m). The bulk of the contribution of VLM is attributable to GIA⁴⁷, which accounts for 41%. The contribution of VLM remains of comparable importance when considering other radiative forcing scenarios. Here, 49% (for SSP3-7.0) and 47% (for SSP5-8.5) of the variances of RSL change deviations from the global mean are explained by VLM (with a global mean projected absolute SL change of 1.03 m and 1.17 m in 2150, respectively).

⁴⁷Caron L. et al. (2018): *GIA Model Statistics for GRACE Hydrology, Cryosphere, and Ocean Science*. Geophysical Research Letters, doi:10.1002/2017GL076644

It was found that VLM uncertainties explain a considerable proportion of RSL change uncertainties (33%). Particularly large uncertainties are introduced in areas where non-linear VLM is dominant. Regionally, non-linear VLM drastically increases uncertainties in projections of RSL change with values up to 1 m. Uncertainty estimates in tectonically active regions (South America, Alaska, Japan) are systematically higher (by a factor of 2-5) than the coastal VLM uncertainty provided at tide gauges by the IPCC AR6 report. The study provides evidence that the reconstructed VLM and its uncertainty more realistically reflect direct observations than alternative estimates^{47, 48}, since non-linear effects were explicitly taken into account. Results imply that current sea level projections underestimate the effect of nonlinear VLM on uncertainties, and that confidence margins of current damage and protection costs to sea level change need to be reassessed.

2.3 Inland Altimetry

Hydrological time series of inland waters

For more than a decade, DGFI-TUM has been working on advanced methods for the calculation of different hydrological datasets from satellite observations. Numerous scientific studies and practical applications were carried out with the data, and they are a visible contribution of DGFI-TUM to the UN Global Climate Observing System (GCOS) in which DGFI-TUM is a National Partner in the German GCOS consortium ([GCOS.de](https://www.gcos.de)).

Starting from water level time series from satellite altimetry⁴⁹, the suite of hydrological quantities calculated at DGFI-TUM is continuously being extended. Since 2019, hydrological parameters have been derived from optical images, such as surface extent, water occurrence masks and land-water masks⁵⁰. Storage changes of lakes and reservoirs from the combination of satellite altimetry and optical remote sensing are another available product⁵¹. The latest dataset is river discharge derived from remote sensing data⁵². All results are freely available in the institute's Database for Hydrological Time Series of Inland Waters (DAHITI) (see Section 4.6).

By the end of 2022, DAHITI provides nine different hydrological parameters for more than 10,000 locations (so-called virtual stations) worldwide. Of these, 4200 stations were newly included in 2022. Their global distribution is shown in Fig. 2.17. Time series of water levels are available for 1445 (+861 in 2022) lakes/reservoirs and 8637 (+3319 in 2022) river crossings. Surface water extent, water occurrence masks and land-water masks are available for 198 lakes and reservoirs. For 70 lakes and reservoirs DAHITI provides time series of storage changes, bathymetry and hypsometry models.

Numerous new stations were also established as part of the **DFG project ARISAS** of the Research Unit 2630 GlobalCDA (Understanding the global freshwater system by combining geodetic and remote sensing information with modelling using a calibration/data assimilation), in which DGFI-TUM provides altimetry-based water level time series for assimilation into hydrological models to improve the understanding of the global freshwater system. In 2022, a total

⁴⁸Kopp R. et al. (2014): *Probabilistic 21st and 22nd century sea-level projections at a global network of tidegauge sites*. Earth's Future, doi:[10.1002/2014EF000239](https://doi.org/10.1002/2014EF000239)

⁴⁹Schwatke C. et al. (2015): *DAHITI – an innovative approach for estimating water level time series over inland waters using multi-mission satellite altimetry*. Hydrology and Earth System Sci., doi:[10.5194/hess-19-4345-2015](https://doi.org/10.5194/hess-19-4345-2015)

⁵⁰Schwatke C., et al. (2019): *Automated extraction of consistent time-variable water surfaces of lakes and reservoirs based on Landsat and Sentinel-2*, Remote Sensing, doi:[10.3390/rs11091010](https://doi.org/10.3390/rs11091010)

⁵¹Schwatke C., et al. (2020): *Volume variations of small inland waters from a combination of satellite altimetry and optical imaging*. Remote sensing, doi:[10.3390/rs12101606](https://doi.org/10.3390/rs12101606)

⁵²Scherer D., et al. (2020): *Long-term discharge estimation for the Lower Mississippi River using satellite altimetry and remote sensing images*. Remote Sensing, doi:[10.3390/rs12172693](https://doi.org/10.3390/rs12172693)



Figure 2.17: Global distribution of more than 10,000 DAHITI virtual stations by December 2022.

of 1545 new GlobalCDA-DAHITI targets were defined in the project's study regions, namely the Mississippi, Amazon, Ganges, Congo, Euphrates and Tigris basins, as well as large parts of France and Germany and the Tibetan Plateau.

In 2022, a major upgrade of DAHITI was carried out, which included both software and algorithms to process the large number of DAHITI targets in near real time with even better accuracy. Most DAHITI targets were also updated with newly released baselines of altimeter data such as Jason-3 (SGDR-F) or SARAL (SGDR-F). Ongoing research on an improved DAHITI approach aims at deriving more accurate water levels in an automated way, including new altimeter missions such as Sentinel-6A and SWOT. The existing approach for calculating the discharge of rivers is being further developed in the direction of a multi-station algorithm in order to further increase the accuracy of the time series.

Validation of water level time series

DGFI-TUM participates in the **ESA project HYDROCOASTAL**⁵³, which focuses on developing novel approaches for the processing of SAR and SARin altimeter measurements to improve data availability and quality in coastal and inland waters. Besides processing the altimeter data with its retracker, DGFI-TUM evaluates the water level time series of inland waters resulting from three different institutions (DTU, ISR, DGFI-TUM) by comparison with corresponding DAHITI virtual stations. In contrast to the HYDROCOASTAL processor, DAHITI uses no dedicated SAR retracking but applies the standard improved threshold retracker followed by an extended outlier rejection and Kalman filtering.

1031 of the 1091 virtual stations from the HYDROCOASTAL processor were compared against corresponding DAHITI stations. Additionally, 246 stations in 6 river basins could be validated against in-situ data of 76 gauging stations. Validation against in-situ data showed that the accuracy of the three tested retracker and DAHITI does not differ significantly (Figure 2.18).

The comparison with DAHITI showed that the accuracy of the time series depends more on the processor's approach to define virtual stations and detect outliers than on the chosen retracker.

⁵³SAR/SARin Radar Altimetry for Coastal Zone and Inland Water Level, Product Validation Report [PDF]

The HYDROCOASTAL processor used incorrect placements of the virtual stations at the edge of a water body or at a dam. However, for most of the low correlating stations the HYDROCOASTAL time series was almost constant and did not show the signal contained in DAHITI data. These deviations were caused either by incorrect retracking or by the river model used in the HYDROCOASTAL processor.

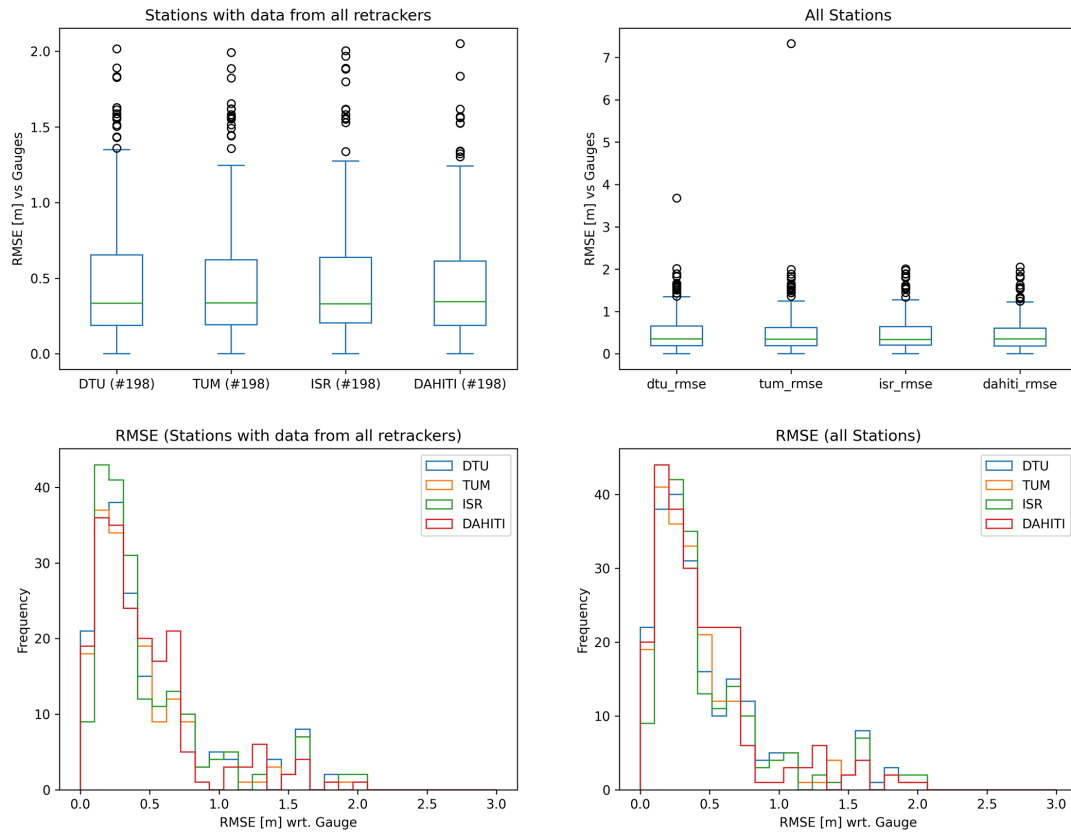


Figure 2.18: Distribution of RMSE between altimetric (each HYDROCOASTAL retracker and DAHITI) and in-situ data for the stations with data from all retrackers (left) and all stations (right).

ICESat-2 river surface slopes

Knowledge of water surface slope (WSS) of rivers is required for many applications in hydrology. For example, WSS is essential to calculate river discharge, one of the Essential Climate Variables. DGFI-TUM has developed a methodology to calculate WSS from ICESat-2 laser altimeter data. The WSS is determined across pairs of beams or along individual beams of ICESat-2's unique measurement geometry with six parallel lidar beams (Scherer et al., 2022a). The approach was validated against pairs of gauges at 815 reaches in Europe and North America with a median absolute error of 23 mm/km, almost complying with the SWOT requirements of 17 mm/km. Since no ground data is required for the calculation, it is possible to apply the methodology globally.

In 2022, DGFI-TUM created the global reach-scale *ICESat-2 River Surface Slope (IRIS)*⁵⁴ dataset that comprises average and extreme WSS derived from ICESat-2 observations between October 2018 and August 2022 as a supplement to 121,583 reaches from the 'SWOT Mission River Database' (SWORD)⁵⁵.

⁵⁴Scherer D., Schwatke C., Dettmering D., Seitz F. (2023): *ICESat-2 River Surface Slope (IRIS): A Global Reach-Scale Water Surface Slope Dataset*, Nature Scientific Data, doi:[10.1038/s41597-023-02215-x](https://doi.org/10.1038/s41597-023-02215-x)

⁵⁵Altenau E. et al. (2021): *SWOT river database (SWORD) (version v1)*. doi:[10.5281/zenodo.4917236](https://doi.org/10.5281/zenodo.4917236)

IRIS can be used to study river dynamics and morphology, to estimate river discharge and to correct water level time series from satellite altimetry. By referencing SWOT as a common database, IRIS can be used together with observations from the SWOT mission. The amount of IRIS data per reach strongly depends on the average cloud cover, as the lidar of ICESat-2 cannot penetrate the clouds. Furthermore, the amount of IRIS data increases with the width of the reach. Figure 2.19 shows the global IRIS WSS. The IRIS dataset is publicly available via Zenodo (Scherer et al., 2022b). The development of IRIS was carried out as part of the above-mentioned **DFG project ARISAS**. IRIS will also help to improve the quality of altimetry-derived water levels on a global scale by correcting the river slope below the satellite overflights to deal with spatial variations in the ground tracks.

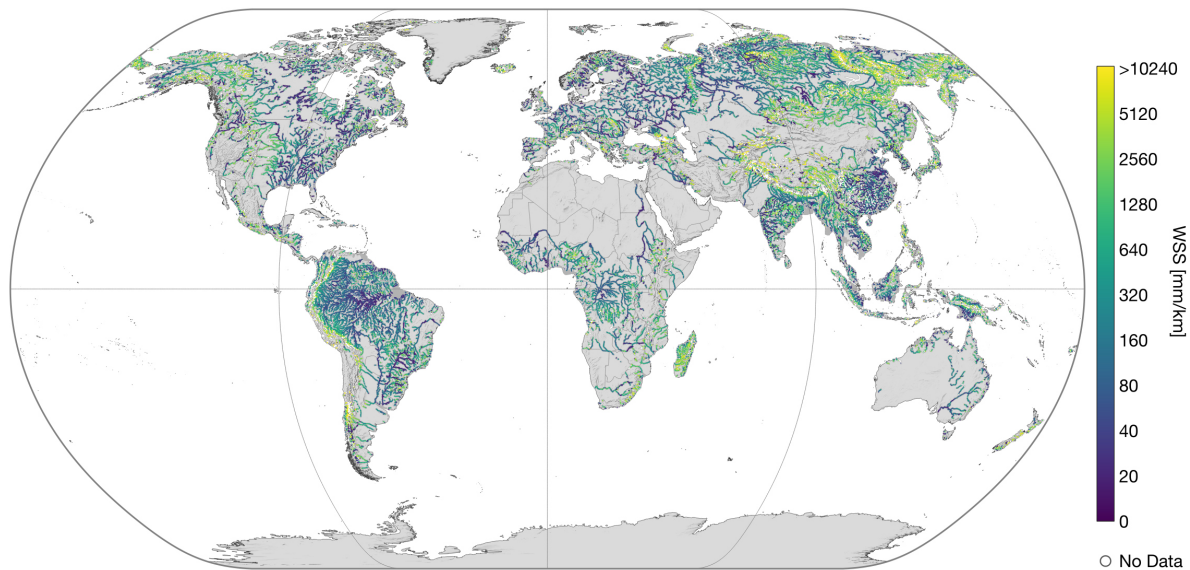


Figure 2.19: IRIS: Global averaged combined water surface slope from ICESat-2.

Related publications

- Cazenave A., Gouzenes Y., Birol, F., Leger F., Passaro M., Calafat F.M., Shaw A., Nino F., Legeais J.F., Oelmann J., Restano M., Benveniste J.: *Sea level along the world's coastlines can be measured by a network of virtual altimetry stations*. Communications Earth and Environment (Nature Portfolio), 3(1), doi:[10.1038/s43247-022-00448-z](https://doi.org/10.1038/s43247-022-00448-z), 2022
- Dettmering D., Schwatke C.: *Ionospheric corrections for satellite altimetry - impact on global mean sea level trends*. Earth and Space Science, 9, doi:[10.1029/2021EA002098](https://doi.org/10.1029/2021EA002098), 2022
- Ehlers F., Schlembach F., Kleinherenbrink M., Slobbe C.: *Validity assessment of SAMOSA retracking for fully-focused SAR altimeter waveforms*. Advances in Space Research, doi:[10.1016/j.asr.2022.11.034](https://doi.org/10.1016/j.asr.2022.11.034), 2022
- Hart-Davis M.G., Sulzbach R., Dettmering D., Thomas M., Seitz F.: *TICON-td: Third-degree tidal constants based on GESLA sea-level records from globally distributed tide gauges (data)*. DGFI-TUM, Munich, doi:[10.1594/PANGAEA.943444](https://doi.org/10.1594/PANGAEA.943444), 2022a
- Hart-Davis M.G., Dettmering D., Seitz F.: *TICON-3: Tidal Constants based on GESLA-3 sea-level records from globally distributed tide gauges including gauge type information (data)*. DGFI-TUM, Munich, doi:[10.1594/PANGAEA.951610](https://doi.org/10.1594/PANGAEA.951610), 2022b

- Heye S., Krug M., Penven P., Hart-Davis M.: *The Natal Bight Coastal Counter-Current: A modeling study*. Continental Shelf Research, 104852, doi:[10.1016/j.csr.2022.104852](https://doi.org/10.1016/j.csr.2022.104852), 2022
- Karimi A., Ghobadi-Far K., Passaro M.: *Barystatic and steric sea level variations in the Baltic Sea and implications of water exchange with the North Sea in the satellite era*. Frontiers in Marine Science, 9, doi:[10.3389/fmars.2022.963564](https://doi.org/10.3389/fmars.2022.963564), 2022
- Oelsmann J., Passaro M., Sánchez L., Dettmering D., Schwatke C., Seitz F.: *Bayesian modelling of piecewise trends and discontinuities to improve the estimation of coastal vertical land motion*. Journal of Geodesy, 96(9), doi:[10.1007/s00190-022-01645-6](https://doi.org/10.1007/s00190-022-01645-6), 2022
- Passaro M., Rautiainen L., Dettmering D., Restano M., Hart-Davis M.G., Schlembach F., Särkkä J., Müller F.L., Schwatke C., Benveniste J.: *Validation of an Empirical Subwaveform Retracking Strategy for SAR Altimetry*. Remote Sensing, 14(16), doi:[10.3390/rs14164122](https://doi.org/10.3390/rs14164122), 2022
- Pfaff M.C., Hart-Davis M., Smith M. E., Veitch J.: *A new model-based coastal retention index (CORE) identifies bays as hotspots of retention, biological production and cumulative anthropogenic pressures*. Estuarine, Coastal and Shelf Science, 107909, doi:[10.1016/j.ecss.2022.107909](https://doi.org/10.1016/j.ecss.2022.107909), 2022
- Scherer D., Schwatke C., Dettmering D., Seitz F. : *ICESat-2 Based River Surface Slope and Its Impact on Water Level Time Series From Satellite Altimetry*. Water Resources Research, 58(11), doi:[10.1029/2022WR032842](https://doi.org/10.1029/2022WR032842), 2022a
- Scherer D., Schwatke C., Dettmering D., Seitz F. : *IRIS: ICESat-2 River Surface Slope (data)*. Zenodo, doi:[10.5281/zenodo.7098113](https://doi.org/10.5281/zenodo.7098113), 2022b
- Schlembach F., Passaro M., Dettmering D., Bidlot J., Seitz F.: *Interference-sensitive coastal SAR altimetry retracking strategy for measuring significant wave height*. Remote Sensing of Environment, 274, 112968, doi:[10.1016/j.rse.2022.112968](https://doi.org/10.1016/j.rse.2022.112968), 2022
- Sulzbach R., Wziontek H., Hart-Davis M.G., Dobsław H., Scherneck H.-G., Van Camp M., Omang O.C.D., Antokoletz E. D., Voigt C., Dettmering D., Thomas M.: *Modeling gravimetric signatures of third-degree ocean tides and their detection in superconducting gravimeter records*. Journal of Geodesy, 96(5), doi:[10.1007/s00190-022-01609-w](https://doi.org/10.1007/s00190-022-01609-w), 2022

3 Cross-Cutting Research Topics

The three overarching research topics Atmosphere, Regional Gravity Field, and Standards and Conventions are closely interlinked with the DGFI-TUM Research Areas Reference Systems and Satellite Altimetry.

The atmosphere (Section 3.1) is crucial for the analysis of all space-geodetic observations. Satellite orbits are perturbed by atmospheric drag, and measurement signals are affected by refraction and propagation delay. These effects must be adequately taken into account in precise orbit determination and geodetic data analysis, and optimizing the corresponding correction models is an important research task. Conversely, geodetic space observations provide valuable information about the state and dynamics of the atmosphere. This information can be used to study atmospheric processes as well as effects of space weather and is also of high interest to other disciplines. Space weather has attracted increasing attention as an emerging field, especially from policy makers and scientists, as it can severely impact modern infrastructures, including navigation systems, power supply and communication facilities. Crucial conclusions about space weather can be drawn from changes in the upper atmosphere, i.e. the sub-components magnetosphere, ionosphere, plasmasphere and thermosphere. DGFI-TUM has built up strong expertise in modeling and forecasting global and regional structures of the electron and neutral density in the Earth's upper atmosphere through the joint analysis of geodetic space observations using problem-adapted data representations and estimation techniques. DGFI-TUM is strongly involved in space weather research in Germany and has cooperated closely with the German Space Situational Awareness Center (Weltraumlagezentrum) and DLR for many years. At the international level, DGFI-TUM has chaired the Focus Area on Geodetic Space Weather Research (FA-GSWR) of the Global Geodetic Observing System (GGOS) under the umbrella of the IAG since 2017.

Precise knowledge of the Earth's gravity field (Section 3.2) is of great relevance for various applications in geodesy, including the realization and unification of height systems and the determination of precise satellite orbits. The latter are a prerequisite for the calculation of accurate reference frames or for reliable estimates of water levels from satellite altimetry. Furthermore, the geoid represents the reference surface for ocean circulation. Temporal changes of the gravity field contain information about mass transports in the Earth system and are of interest, for example, for the study of dynamic processes in the Earth's interior or in the hydrosphere. DGFI-TUM primarily focuses on theoretical and practical aspects of regional gravity field determination with the goal to create high-resolution and high-precision potential fields by combining different data types, such as space- and airborne gravity measurements, satellite altimetry, terrestrial and ship gravimetry.

The definition and application of uniform standards and conventions (Section 3.3) is essential to ensure the highest possible consistency of parameters and data products. At the international level, DGFI-TUM is deeply involved in the activities of the relevant bodies for defining standards in geodesy and monitoring their implementation. DGFI-TUM chairs the GGOS Bureau of Products and Standards (BPS) and operates it jointly with several partners. Within the United Nations Global Spatial Information Management (UN-GGIM), DGFI-TUM provides the IAG representative for the key area 'Data Sharing and Development of Standards' in the UN-GGIM Subcommittee 'Geodesy'.

3.1 Atmosphere

The Earth's atmosphere can be divided into various layers depending on physical parameters such as temperature or charge state. Following the temperature profile, the atmosphere can be divided into troposphere, stratosphere, mesosphere, thermosphere and exosphere. In the case of the charge state, the atmosphere can be divided into the neutral lower atmosphere up to about 50 km altitude, the ionosphere from 50 km to about 1000 km altitude, and the plasmasphere above that. Both the plasmasphere and the ionosphere can be characterized by the number of free electrons, i.e. the electron density and thus, play a key role in monitoring space weather. Since the thermosphere, approximately between 80 km and 800 km altitude, coincides with the region of highest ionization, strong physical interactions exist between the neutral density of the thermosphere and the electron density of the ionosphere.

In 2022, the DFG projects MuSE (Multi-Satellite ionosphere-plasmasphere Electron density reconstruction) and TIPOD (Development of High-precision Thermosphere Models for Improving Precise Orbit Determination of Low-Earth-Orbiting Satellites), both part of the Priority Programme (SPP) 1788 'Dynamic Earth', as well as the project ML-IonoCast (Machine Learning for Forecasting the Ionospheric Total Electron Content) funded by the scholarship programme 'Research grants for doctoral programmes in Germany' of the DAAD (German Academic Exchange Service) covered most of the research work at DGFI-TUM on modeling and forecasting the state of the components ionosphere, plasmasphere, and thermosphere of the upper atmosphere. Special attention was given to the consideration of space weather effects.

Related to already completed projects (see also previous Annual Reports), new publications by Hernández-Pajares et al. (2022) and Fernandez-Gomez et al. (2022) investigated enhanced ionospheric corrections for precise agriculture using GNSS (project AUDITOR) and ionosphere-thermosphere coupling processes (project INSIGHT-II). The studies by Jerez et al. (2022) on the assessment of global and regional VTEC models (in the context of the long-running project OPTIMAP), and by Lalgudi Gopalakrishnan and Schmidt (2022) on the development of three-dimensional electron density models considering inequality constraints (project TIK) are provided in more detail below.

Assessment of global and regional VTEC maps for regional applications

In the study of Jerez et al. (2022), different global and regional VTEC models, so-called Global Ionosphere Maps (GIM) and Regional Ionosphere Maps (RIM), have been assessed with respect to their quality over Brazil. Questions were discussed whether there is an added value by using RIMs compared to using only GIMs and, if so, to what extent this added value depends on study region and space weather activity during the considered time period. To answer these questions, the spherical harmonic (SH) model 'codg' from CODE in Berne, the voxel-based model 'uqrg' from UPC in Barcelona, and the models 'otlg' and 'othg' from DGFI-TUM have been used as GIMs. The latter two VTEC models, the low-resolution 'otlg' and the high-resolution 'othg', were developed within OPTIMAP and are both based on the series expansion

$$VTEC_{\text{glob}}(\varphi, \lambda, t) = \sum_{k_1=0}^{K_{J_1}-1} \sum_{k_2=0}^{K_{J_2}-1} d_{\text{glob};k_1,k_2}^{J_1,J_2}(t) \phi_{k_1,J_1}(\varphi) \tilde{\phi}_{k_2,J_2}(\lambda), \quad (3.1)$$

in terms of two-dimensional (2-D) tensor products $\phi_{k_1,J_1}(\varphi) \tilde{\phi}_{k_2,J_2}(\lambda)$ of polynomial B-spline functions $\phi_{k_1,J_1}(\varphi)$ and trigonometric B-spline functions $\tilde{\phi}_{k_2,J_2}(\lambda)$ depending on geomagnetic latitude φ and geomagnetic longitude λ , respectively, defined in a Sun-fixed coordinate system; t means the time. In Eq. (3.1) $d_{\text{glob};k_1,k_2}^{J_1,J_2}(t)$ are the $K_{J_1} \cdot K_{J_2}$ initially unknown time-dependent series coefficients. The total numbers $K_{J_1} = 2^{J_1} + 2$ and $K_{J_2} = 3 \cdot 2^{J_2}$ of shift parameters k_1 and k_2 for

the B-spline functions depend on the B-spline levels J_1 and J_2 . As discussed by Goss et al. (2020)⁵⁶ the level values $J_1 = 5$ and $J_2 = 3$ have been chosen for ‘othg’, such that the series expansion (3.1) considers spectral components of up to a maximum SH degree $n_{\max} = 33$ and thus, much finer VTEC structures, e.g. over the equatorial anomaly, than ‘codg’, for instance. According to Goss (2022) the global VTEC product ‘othg’ is defined as

$$\widehat{VTEC}_{\text{glob}}(\varphi_i, \lambda_k, t_s) \Big|_{i=1, \dots, 73, k=1, \dots, 72} \quad (3.2)$$

in a geographical geocentric coordinate system evaluated in the grid points

$$P_{i,k} = P(\varphi_i = -90^\circ + (i-1) \cdot \Delta\Phi, \lambda_k = 0^\circ + (k-1) \cdot \Delta\Lambda) \quad (3.3)$$

with sampling intervals $\Delta\Phi = 2.5^\circ$ and $\Delta\Lambda = 5.0^\circ$ including the corresponding standard deviations $\widehat{\sigma}_{VTEC_{\text{glob}}}(\varphi_i, \lambda_k, t_s)$ from the estimated coefficients

$$\widehat{d}_{\text{glob};k_1,k_2}^{5,3}(t_s) \Big|_{k_1=0, \dots, 33, k_2=0, \dots, 23} \quad (3.4)$$

as defined in Eq. (3.1) at discrete time moments $t_s = t_{s-1} + \Delta T$ with a temporal sampling interval of $\Delta T = 10$ min. For the low-resolution model ‘otlg’ the level values $J_1 = 4$ and $J_2 = 3$ have been chosen in Eq. (3.1), such that its spectral content is comparable with the one of ‘codg’⁵⁷.

Among the RIMs used in the study of Jerez et al. (2022) are the regional model ‘inpe’ from the Instituto Nacional de Pesquisas Espaciais in Brazil and the ‘othr’ model from DGF1-TUM. The generation of regional models is restricted to continental regions which are characterized by a dense data coverage. In the case of ‘othr’, the global VTEC representation (3.1) serves as background information and allows for the regional representation

$$\begin{aligned} VTEC_{\text{reg}}(\varphi, \lambda, t) &= VTEC_{\text{glob}}(\varphi, \lambda, t) + \Delta VTEC_{\text{reg}}(\varphi, \lambda, t) \\ &= VTEC_{\text{glob}}(\varphi, \lambda, t) + \sum_{k_3=0}^{K_{J_3}-1} \sum_{k_4=0}^{K_{J_4}-1} d_{\text{reg};k_3,k_4}^{J_3,J_4}(t) \phi_{k_3,J_3}(\varphi) \phi_{k_4,J_4}(\lambda), \end{aligned} \quad (3.5)$$

where we introduce tensor products of polynomial B-spline functions of levels J_3 and J_4 with shift parameters k_3 and k_4 , respectively, for the densification model $\Delta VTEC_{\text{reg}}(\varphi, \lambda, t)$. The use of polynomial endpoint-interpolating B-splines ensures that the model intervals are closed in both directions, latitude and longitude, at the region boundaries. Equation (3.5) applies for a rectangular area $\Delta\Omega$ of size $\Upsilon \times \Gamma$. Herein, Υ means the extent of the area $\Delta\Omega$ with respect to latitude φ , whereas Γ is the extent of $\Delta\Omega$ with respect to longitude λ . Note, that in the regional representation (3.5) latitude φ and longitude λ are defined in a geographical Earth-fixed coordinate system (cf. Fig. 3.2) and therefore, the corresponding coordinate transformations between the representations of the global model $VTEC_{\text{glob}}$ and the regional densification model $\Delta VTEC_{\text{reg}}$ have to be considered. The numerical values for the regional levels J_3 and J_4 , restricted to the inequalities $J_3 \leq \log_2(\Upsilon/\Delta\varphi - 1)$ and $J_4 \leq \log_2(\Gamma/\Delta\lambda - 1)$, depend on the average sampling intervals $\Delta\varphi$ and $\Delta\lambda$ of the observations within the region $\Delta\Omega = \Upsilon \times \Gamma$. Analog to the global model ‘othg’ in the Eqs. (3.2) to (3.4) the regional model ‘othr’ is defined according to Goss (2022) as

$$\widehat{VTEC}_{\text{reg}}(\varphi_i, \lambda_k, t_s) \Big|_{i=1, \dots, N_\varphi+1, k=1, \dots, N_\lambda+1} \quad (3.6)$$

in a geographical geocentric coordinate system in grid points $P_{i,k} = P(\varphi_i, \lambda_k)$ with $\varphi_i = \varphi_{\min} + (i-1) \cdot \Delta\Phi$ and $\lambda_k = \lambda_{\min} + (k-1) \cdot \Delta\Lambda$ with the sampling intervals $\Delta\Phi = \Upsilon/N_\varphi$ and $\Delta\Lambda = \Gamma/N_\lambda$

⁵⁶Goss A., Schmidt M., Erdogan E., Seitz F. (2020): *Global and regional high-resolution VTEC modelling using a two-step B-spline approach*. Remote Sensing, doi:10.3390/rs12071198

⁵⁷Goss A., Schmidt M., Erdogan E., Görres B., Seitz F. (2019): *High-resolution vertical total electron content maps based on multi-scale B-spline representations*. Annales Geophysicae, doi:10.5194/angeo-37-699-2019

including the corresponding standard deviations $\hat{\sigma}_{VTEC_{reg}}(\varphi_i, \lambda_k, t_s)$ calculated from the estimated coefficients

$$\hat{d}_{reg; k_3, k_4}^{J_3, J_4}(t_s) \Big|_{k_3=0, \dots, K_3-1, k_4=0, \dots, K_4-1} \quad (3.7)$$

with $K_3 = 2^{J_3} + 2$ and $K_4 = 2^{J_4} + 2$ at discrete time moments $t_s = t_{s-1} + \Delta T$ with a temporal sampling interval of $\Delta T = 10$ min. Note, that for the sampling intervals $\Delta\Phi$ and $\Delta\Lambda$ we usually choose for the regional model (3.6) the values $\Delta\Phi = \Delta\Lambda = 1.0^\circ$. It needs further to be noted, that according to Eq. (3.5) the global VTEC representation (3.1) has to be considered in ‘othr’ by adding it to the estimation of the densification model.

To avoid correlations between the estimated global coefficients (3.4) and the estimated regional coefficients (3.7), we divide the set \mathcal{D} of all available observations (usually only from GNSS) into a subset \mathcal{D}_1 of global observations and a subset \mathcal{D}_2 of observations related to the regional densification area $\Delta\Omega$ under investigation. In our current installation we determine the set \mathcal{D}_1 by segmenting the Earth’s surface into bins of a size related to the global sampling intervals. For all bins in which more than two receiver stations of GNSS networks (e.g. IGS, EUREF, UNAVCO) are located, we select this receiver station which is the nearest one to the center of the bin. Then all observations of the chosen receiver station are collected in the global set \mathcal{D}_1 . The observations of the non-chosen stations within the bins and related to receiver stations within the densification area $\Delta\Omega$ are collected in the regional data set \mathcal{D}_2 . The whole procedure is visualized in Fig. 3.1; for more details see Goss et al. (2020).

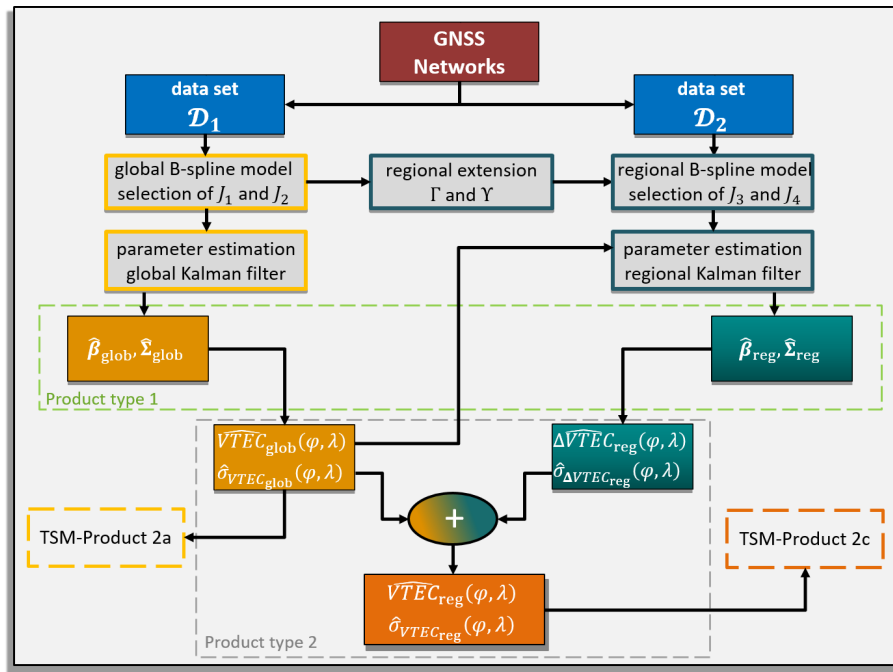


Figure 3.1: Flowchart of the densification procedure, including the estimation of the global model (left, orange) and the estimation of the regional densification (right, green); vectors $\hat{\beta}_{glob}$ and $\hat{\beta}_{reg}$ include the estimated global coefficients (3.4) and the estimated regional coefficients (3.7) as well as other parameters such as differential code biases (DCB); matrices $\hat{\Sigma}_{glob}$ and $\hat{\Sigma}_{reg}$ are the corresponding covariance matrices; figure taken from Goss et al. (2020).

Figure 3.2 shows on the right the global ‘othg’ result according to Eq. (3.2) for a specific time moment t_s . The region enclosed by the yellow colored rectangle defines as an example a densification area $\Delta\Omega = [35^\circ, 60^\circ] \times [-10^\circ, 25^\circ]$ over Europe of extent $Y = 25^\circ$ and $\Gamma = 35^\circ$ with respect to latitude and longitude, respectively. With the average sampling intervals $\Delta\varphi = \Delta\lambda = 2.5^\circ$ of the observations within \mathcal{D}_2 we obtain for the levels J_3 and J_4 the numerical values

$J_3 = J_4 = 3$ (Goss et al., 2020). Consequently, the ‘otr’ model for Europe reads

$$\widehat{VTEC}_{\text{reg}}(\varphi_i, \lambda_k, t_s) \Big|_{i=1, \dots, 26, k=1, \dots, 36} \quad (3.8)$$

evaluated in grid points

$$P_{i,k} = P(\varphi_i = 35^\circ + (i-1) \cdot \Delta\Phi, \lambda_k = -10^\circ + (k-1) \cdot \Delta\Lambda) \quad (3.9)$$

with sampling intervals $\Delta\Phi = \Delta\Lambda = 1.0^\circ$ from the estimated coefficients

$$\widehat{d}_{\text{reg};k_3,k_4}^{3,3}(t_s) \Big|_{k_3=0, \dots, 9, k_4=0, \dots, 9} \quad (3.10)$$

at discrete time moments $t_s = t_{s-1} \cdot \Delta T$. The regional model ‘otr’, i.e. the corresponding regional map for Europe, is finally obtained by adding the estimated densification part $\Delta\widehat{VTEC}_{\text{reg}}$ shown in the right panel of Fig. 3.2 to the estimated global VTEC model $\widehat{VTEC}_{\text{glob}}$ evaluated in the grid points $P_{i,k}$ from Eq. (3.9) within the area $\Delta\Omega = [35^\circ, 60^\circ] \times [-10^\circ, 25^\circ]$, i.e. the region enclosed by the yellow colored rectangle in the global map in the left panel of Fig. 3.2. According to Goss et al. (2020) the ‘otrg’ product estimated with level values $J_3 = J_4 = 3$ comprises spectral components until a maximum SH degree of $n_{\text{max}} = 63$.

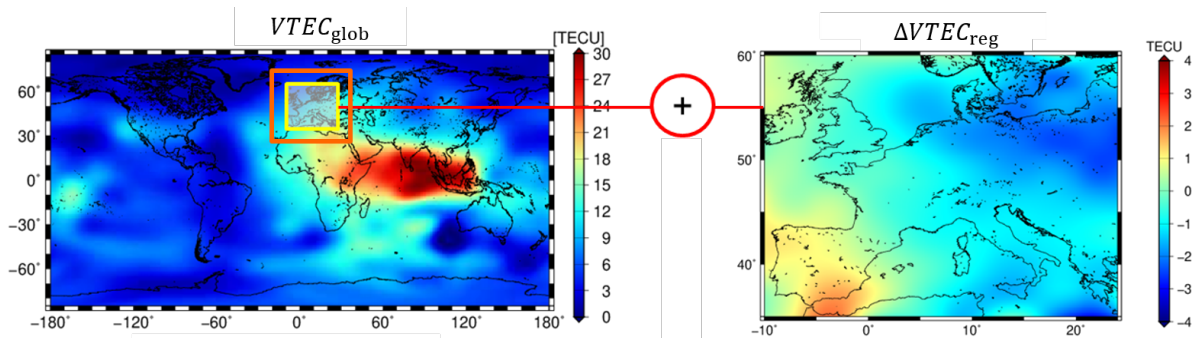


Figure 3.2: Left: estimated global solution $\widehat{VTEC}_{\text{glob}}(\varphi, \lambda, t)$ for ‘otrg’ according to the Eq. (3.2) from the coefficients (3.4) for a specific time moment t_s calculated in the grid points (3.3); Right: estimation $\Delta\widehat{VTEC}_{\text{reg}}(\varphi, \lambda, t)$ of the densification model as defined in Eq. (3.5) from the coefficients (3.10) for the same time moment t_s calculated in the grid points (3.9). In the yellow colored rectangle on the left the global model has additionally to be evaluated from the coefficients (3.4) at time t_s in the grid points (3.9). In doing this the sum of the global model in the yellow rectangle and the result of the right panel provide the high-resolution product ‘otr’.

The limitation of the regional model ‘otr’ to the densification area $\Delta\Omega$ means a weakness in many applications, e.g. in precise point positioning (PPP), because in case of RIMs the software packages often assume that outside of the densification area the VTEC values are zero. To avoid this, a new hybrid regional VTEC model, referred to as ‘otrg’, was developed at DGFI-TUM. The most important difference to ‘otr’ is the extension of the global VTEC model part – evaluated on grid points $P_{i,k}$ with 1° sampling according to Eq. (3.9) – to a larger region $\Delta\Omega_{\text{ext}}$ such that the densification area $\Delta\Omega$ is completely surrounded by $\Delta\Omega_{\text{ext}}$ and $\Delta\Omega \subset \Delta\Omega_{\text{ext}}$ holds. In the left panel of Fig. 3.2 the orange colored rectangle encloses the area $\Delta\Omega_{\text{ext}}$ and contains a spectral content of VTEC up to SH degree 33. The (much) smaller densification region $\Delta\Omega$ enclosed by the yellow colored rectangle contains the high spectral content of VTEC up to SH degree 63. This adaptation of region sizes to the covered spectral content reflects the idea of a multi-resolution representation (MRR), which signifies the fundamental strategy of ionosphere modeling at DGFI-TUM. Figure 3.3 shows the principle of a three-area model consisting of a global, a regional, and a local part. While the size of the regions decreases from global to local, the spectral content simultaneously increases from global to local. This behavior corresponds to Heisenberg’s uncertainty principle as it is understood in MRR.

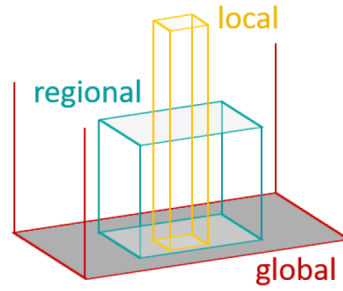


Figure 3.3: Schematic representation of a three-area model consisting of a global, a regional and a local VTEC part; figure taken from Goss (2022); the local model part describes the highest spectral components, i.e. the finest structures of VTEC in comparison to the regional and global model parts, which reflect the medium and low spectral components.

Jerez et al. (2022) used the regional product ‘othr’ and the hybrid product ‘otrg’ – both with a temporal sampling interval of $\Delta T = 10$ minutes – together with the aforementioned models. Figure 3.4 shows the ‘othr’ and ‘otrg’ maps for South America at September 3 (day of year (DOY) 246), 2017 at 0:00 UT. The densification area $\Delta\Omega = [-30^\circ, 5^\circ] \times [-70^\circ, -35^\circ]$ is defined by an extent of $\Upsilon = 35^\circ$ and $\Gamma = 35^\circ$ with respect to latitude and longitude, respectively. We introduce the level values $J_3 = J_4 = 3$ in Eq. (3.6). Figure 3.4 shows on the left the ‘othr’ product for Brazil according to Eq. (3.8). The right panel of Fig. 3.4 depicts the hybrid product ‘otrg’, where the extended region $\Delta\Omega_{\text{ext}}$ is chosen as $\Delta\Omega_{\text{ext}} = [-60^\circ, 20^\circ] \times [-90^\circ, -30^\circ]$. Within this region the global model (3.2) has to be evaluated from the coefficients (3.4) at time t_s in the grid points $P_{i,k} = P(\varphi_i = -60^\circ + (i-1) \cdot 1.0^\circ, \lambda_k = -90^\circ + (k-1) \cdot 1.0^\circ)$ with $i = 1, \dots, 81$ and $k = 1, \dots, 61$.

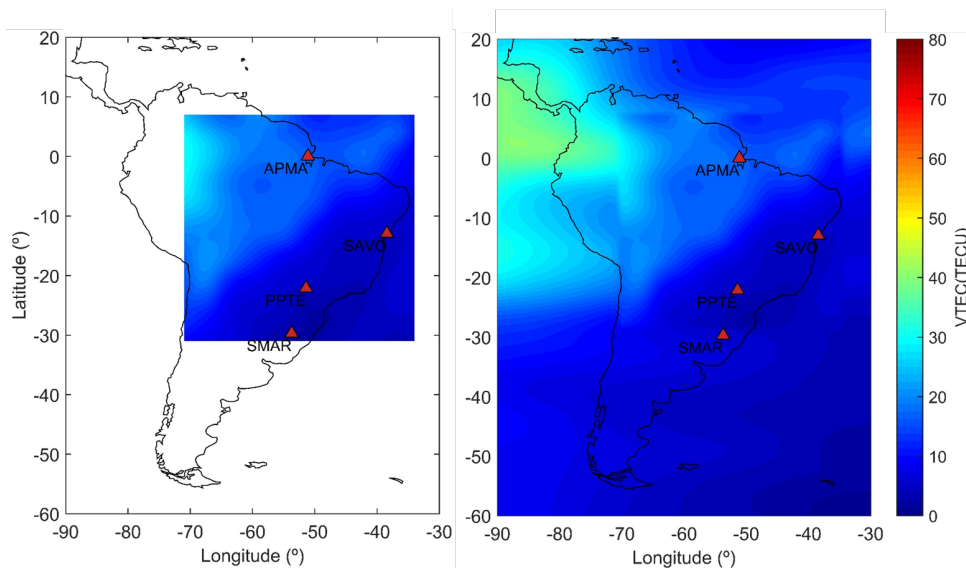


Figure 3.4: Left panel shows the ‘othr’ product, the right panel the corresponding product ‘otrg’, both for September 3 (DOY 246), 2017 at 0:00 UT; the red triangles mark the 4 GNSS receiver stations used for the PPP study case; panels taken from Jerez et al. (2022).

To rate the quality and the performance of the chosen 7 VTEC products, Jerez et al. (2022) perform both, a validation with ionosonde measurements and an assessment by means of GNSS positioning. The 4 selected GNSS receiver stations are shown as red triangles in Fig. 3.4. While the regional models ‘othr’ and ‘otrg’ provide the best results from the ionosonde validations (not shown), the 3-D position errors of the 7 products and the 4 receiver stations from Table 3.1 are more difficult to interpret. First, it should be mentioned that the purpose of

this positioning assessment was not to obtain the best results, i.e., the smallest possible 3-D errors, but to investigate the deviations between the results caused by the different ionosphere products. Consequently, the presented 3-D errors could be reduced by using more precise models, e.g., to account for tropospheric delay. With respect to the 7 ionosphere products, it was found that the hybrid model ‘otrg’ provides the lowest 3-D error with the exception of the station APMA; see Table 3.1, right column. APMA is located in the northern part of the densification area near the geomagnetic equator. Because the time window chosen for the study includes a geomagnetic storm around September 7 and 8 (DOYs 250 and 251), 2017, the results from the different models for the equatorial region are more inconsistent than, e.g., for station PPTTE. Station SMAR, on the other hand, is located at the southern boundary of the densification area. Consequently, the 3-D error with respect to the regional model ‘othr’ is much larger than for the hybrid model ‘otrg’ and for the global models. Details to this study can be found in Jerez et al. (2022). In summary, the authors conclude that DGFI-TUM’s hybrid product ‘otrg’ has the best performance in positioning among all the maps considered in this study.

Table 3.1: Time-averaged 3-D positioning error values [m] for each of the 4 stations APMA, SAVO, PPTTE and SMAR using the 7 products ‘uqrg’, ‘codg’, ‘othg’, ‘otlg’, ‘inpe’, ‘othr’, and ‘otrg’. The maximum and minimum averaged 3-D error values are highlighted in red and green, respectively.

GNSS station	uqrg	codg	othg	otlg	inpe	othr	otrg
APMA	0.934	0.759	0.808	0.757	1.108	0.868	0.918
SAVO	0.850	0.745	0.851	0.827	1.306	0.766	0.736
PPTTE	1.133	1.121	1.052	1.103	1.414	1.001	0.981
SMAR	0.845	0.571	0.545	0.547	0.690	1.805	0.541

Estimation of a 3-D electron density model by constraint optimization

Lalgudi-Gopalakrishnan and Schmidt (2022) developed a 3-D model of the electron density within ionosphere and plasmasphere. The ionosphere, defined between $h_{\min} \approx 70$ km and $h_{\max} \approx 1000$ km, is stratified into the D –, the E –, the F_1 – and the F_2 –layer with a smooth transition into the plasmasphere. In the former project TIK we developed a model which approximates the vertical electron density profile by the Multi-Layer-Chapman-Model (MLCM)

$$N_e(h) = \sum_{Q=1}^4 N_e^Q(h) + N_e^P(h) \quad (3.11)$$

which consists of the sum of four Chapman functions

$$N_e^Q(h) = N_m^Q \exp\left(\frac{1}{2} \left(1 - \frac{h - h_m^Q}{H^Q} - \exp\left(-\frac{h - h_m^Q}{H^Q}\right)\right)\right) \quad (3.12)$$

– one for each ionosphere layer $Q \in \{D, E, F_1, F_2\}$ – and an exponential decay function

$$N_e^P(h) = N_0^P \exp\left(-\frac{|h - h_m^{F_2}|}{H^P}\right), \quad (3.13)$$

for the plasmasphere P ; see also Annual Report 2019. The quantities N_m^Q (= peak density), h_m^Q (= peak height) and H^Q (= scale height) of the Q –layer in Eq. (3.12) as well as the quantities N_0^P (= basis density) and H^P (= scale height) of the plasmasphere in Eq. (3.13) define the set

$$\mathcal{K} = \{N_m^D, h_m^D, H^D, N_m^E, h_m^E, H^E, N_m^{F_1}, h_m^{F_1}, H^{F_1}, N_m^{F_2}, h_m^{F_2}, H^{F_2}, N_0^P, H^P\} \quad (3.14)$$

of altogether 14 key parameters $\kappa_r \in \mathcal{K}$ with $r = 1, 2, \dots, 14$ of the MLCM. Each key parameter κ_r can be represented globally by a 2-D B-spline expansion similar to Eq. (3.2). Since the key parameters describe the electron density of the ionosphere and the plasmasphere according to the MLCM, significant correlations will exist between various pairs of key parameters κ_r and κ_s with $r, s = 1, 2, \dots, 14$, e.g. for $\kappa_r = N_m^{F_2}$ and $\kappa_s = N_m^{F_1}$. The incorporation of inequality constraints

$$\kappa_{r;\text{lo}}(\varphi, \lambda) \leq \kappa_r(\varphi, \lambda) \leq \kappa_{r;\text{up}}(\varphi, \lambda) \quad (3.15)$$

for the key parameters $\kappa_r(\varphi, \lambda)$ may decorrelate them by considering specific intervals bounded by physically realistic lower and upper bound functions $\kappa_{r;\text{lo}}(\varphi, \lambda)$ and $\kappa_{r;\text{up}}(\varphi, \lambda)$. The region enclosed by all bound functions is called the feasible region and is a subspace of the solution space of the optimization problem to be solved. The inequality constraint (3.15) is said to be active at a certain position (φ, λ) if it is satisfied as an equality constraint, e.g. $\kappa_r(\varphi, \lambda) = \kappa_{r;\text{up}}(\varphi, \lambda)$. It is said to be inactive if the inequality signs hold and it is violated if the inequality constraint (3.15) does not hold. In this case the solution is located outside the feasible region.

A wide variety of algorithms for solving inequality constrained optimization problems exists. Most of them can be subdivided into two main classes: (1) the active-set method and (2) the interior-point method. The algorithms of the first type follow the boundary of the feasible region in the solution space, the latter follow a central path through the interior of the feasible region (Fig. 3.5). Furthermore, in active-set algorithms, constraints are considered in an exact way, while interior-point methods use them in a more relaxed way. Interior-point methods usually need fewer, but numerically more expensive, iterations⁵⁸.

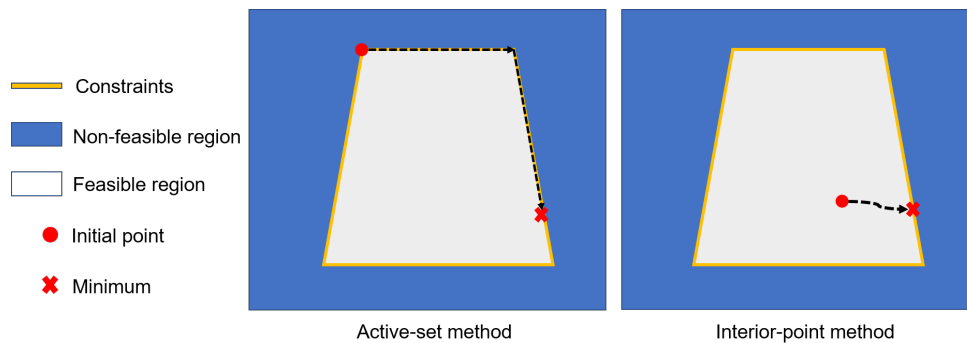


Figure 3.5: To solve the optimization problem, the iterations of the interior-point method (right) follow an internal path through the feasible region until the minimum is reached; in the active-set method (left) the iteration path follows the boundary of the feasible region. If only one inequality constraint is active, the optimal solution, i.e. the minimum, is located on the boundary. The region outside the feasible region within the solution space is called the non-feasible region; modified figure from Roese-Koerner (2015).

Lalgudi Gopalakrishnan transformed in his dissertation⁵⁹ the problem of estimating the key parameters of the MLCM (3.11) into an optimization problem and developed an inequality constrained optimization algorithm (ICOA) based on the interior-point method. Since the joint estimation of all key parameters in the set \mathcal{K} defined in Eq. (3.14) is very challenging, Lalgudi Gopalakrishnan and Schmidt (2022) applied the ICOA to estimate the selected five key parameters of the subset $\mathcal{K}_1 = \{N_m^{F_2}, h_m^{F_2}, H^{F_2}, N_0^P, H^P\} \subset \mathcal{K}$. Consequently, the remaining key parameters of the complimentary set $\mathcal{K}_2 = \mathcal{K} \setminus \mathcal{K}_1$ are assumed to be given, e.g. from ionosphere models such as the International Reference Ionosphere (IRI). It needs to be noted that the interior-point method should be applied to a not too large number of key parameters. The number five, as in this example, has proven to be a suitable upper limit.

⁵⁸Roese-Koerner L. (2015): *Convex optimization for inequality constrained adjustment problems*. Dissertation, University of Bonn

⁵⁹Lalgudi Gopalakrishnan G. (2023): *Ionosphere electron density modelling using a constrained optimization approach*. Dissertation, Technical University of Munich

Constraint violations are intolerable in electron density modeling. For example, the maximum value N_m^Q of the electron density within the layer Q , as defined in Eq. (3.12), must not be negative. Similarly, for instance, the inequalities $h_m^E < h_m^{F_1} < h_m^{F_2}$ have to be satisfied. In running the ICOA the occurrence of constraint violations depends on several factors, e.g the definition of the upper and lower bounds, the number of inequality constraints and the step size of the iterations along the internal path, i.e. the dashed line in the right panel of Fig. 3.5. The choice of the step size is not trivial, since an overshooting of the feasible region's boundary into the non-feasible region would cause constraint violations.

Since constraint violations are not tolerable and we further want to estimate more than five key parameters in one step, we applied as an alternative to the interior-point method the active-set method in the frame of a master thesis (Qiu 2022) to the MCLM as defined in Eqs. (3.11) to (3.14). As shown in Fig. 3.5 (left) the main idea of the active-set method is to follow the boundary of the feasible region in an iterative approach. This is done by extracting constraints that hold as equality constraints, i.e. being active, at the point of the current solution and therefore solve a sequence of equality constrained subproblems. If at least one inequality constraint is active, the optimal solution, i.e. the minimum, is located on the boundary.

In the following example we simulate electron density observations from the MCLM defined by Eqs. (3.11) to (3.14). We choose for the 9 key parameters of the subset

$$\mathcal{K}_1 = \{N_m^D, N_m^E, N_m^{F_1}, h_m^{F_1}, N_m^{F_2}, h_m^{F_2}, H^{F_2}, N_0^P, H^P\} \subset \mathcal{K} \quad (3.16)$$

the ‘true’ numerical values (second column of Tab. 3.2), and for the 5 remaining key parameters of the subset $\mathcal{K}_2 = \{h_m^D, H^D, h_m^E, H^E, H^{F_1}\}$ numerical values which are assumed to be already known from IRI. The ICOA based on the active-set method needs to estimate the 9 key parameters κ_r of the set (3.16) under consideration of the inequality constraints $\kappa_{r;\text{lo}} \leq \kappa_r \leq \kappa_{r;\text{up}}$ with $r = 1, 2, \dots, 9$ formulated analog to Eq. (3.15). Chosen values for the lower and upper bounds $\kappa_{r;\text{lo}}$ and $\kappa_{r;\text{up}}$ are listed in Tab. 3.2 (third and fourth column).

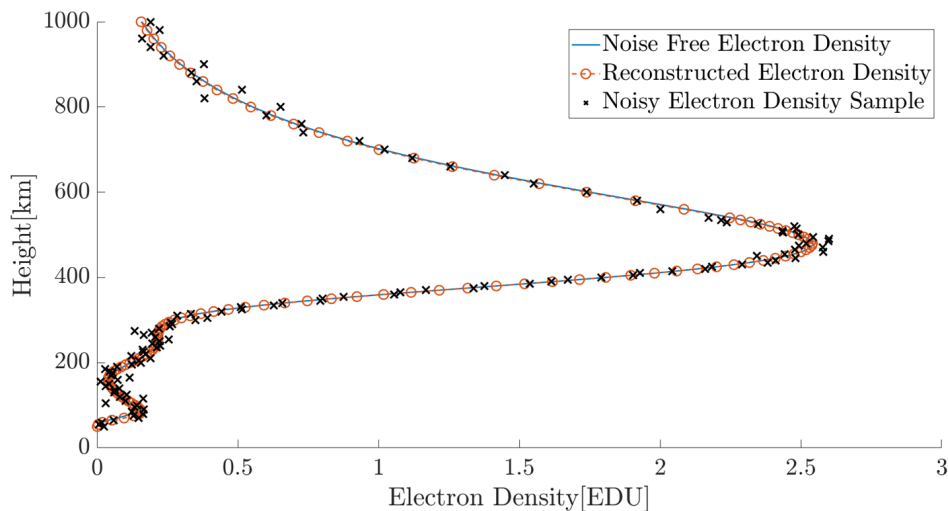


Figure 3.6: Simulated electron density observations $N_e(h_i)$ (black crosses) at $N = 122$ discrete heights h_i and estimated electron density values $\hat{N}_e(h_i)$ (brown circles) derived from the 9 estimated key parameters $\hat{\kappa}_r$ of the subset (3.16). Numerical values for the 9 key parameters are listed in Table 3.2; for details see Qiu (2022).

The blue curve in Fig. 3.6 shows the ‘true’ electron density profile calculated from the ‘true’ and the already known numerical values for the key parameters. From this profile we generate electron density observations $N_e(h_i)$ at N discrete heights h_i with $i = 1, 2, \dots, N$ (Fig. 3.6, black crosses) by adding 5% white noise. For the discretization along the height, we apply an irregular sampling strategy, with sampling intervals of 5 km between 50 and 540 km height and of

20 km between 540 and 1000 km height (at the lower heights much more electron density variations are expected than in the upper part). In total we have $N = 122$ discrete electron density observations along the vertical profile. Brown circles in Fig. 3.2 represent estimated electron density observations $\hat{N}_e(h_i)$ determined from the ICOA based on the active-set method. Table 3.2 (column six) shows the differences between estimated and ‘true’ values of the key parameters (listed in the fifth and second column, respectively). The RMS of the deviations between estimated and simulated observations (brown circles and black crosses), i.e. the residuals $r(h_i) = \hat{N}_e(h_i) - N_e(h_i)$, amounts to 0.0078 EDU ($1 \text{ EDU} = 1 \cdot 10^{12} \text{ el/m}^3$).

Table 3.2: Numerical values of a simulation study based on electron density data generated from the ‘true’ values (second column) of the 9 key parameters (first column).

Key parameter κ_r	‘true’ value $\kappa_{r;\text{true}}$	lower bound $\kappa_{r;\text{lo}}$	upper bound $\kappa_{r;\text{up}}$	estimation $\hat{\kappa}_r$	difference $\hat{\kappa}_r - \kappa_{r;\text{true}}$
N_m^D [EDU]	0.05	0.01	0.20	0.057	0.007
N_m^E [EDU]	0.10	0.00	0.50	0.096	-0.004
$N_m^{F_1}$ [EDU]	0.20	0.10	0.50	0.21	0.01
$h_m^{F_1}$ [km]	250	200	300	248.99	-1.01
$N_m^{F_2}$ [EDU]	2.50	2.20	2.60	2.49	-0.01
$h_m^{F_2}$ [km]	480	220	500	480.57	0.57
H^{F_2} [km]	80	75	120	80.35	0.35
N_0^P [EDU]	0.025	0.02	0.03	0.027	0.002
H^P [km]	80	75	120	75	-5

Table 3.2 shows that the numerical values of all estimated key parameters $\hat{\kappa}_r$ in the fifth column are close to the ‘true’ values $\kappa_{r;\text{true}}$ in the second column. Since the numerical values of the estimated key parameters are all within the intervals defined by the lower and the upper bounds, $\kappa_{r;\text{lo}}$ and $\kappa_{r;\text{up}}$, no constraint violations occur. In the last row of Table 3.2 the inequality constraint $\kappa_{r;\text{lo}} \leq \kappa_r$ is active since $\hat{H}^P = 75 \text{ km}$ holds. The estimated value for the key parameter H^P is equal to the lower bound and the optimal solution of the MLCM defined by the Eqs. (3.11) to (3.14) is located on the boundary of the feasible region. For details see Qiu (2022).

Uncertainty Quantification from Machine Learning Ensemble Approach

In the Annual Report 2021 we discussed the application of Machine Learning (ML) techniques, namely Regression Tree (RT) and Random Forest (RF) regression, for VTEC forecasting. One topic of the **DAAD project ML-IonoCast** in 2022 was the application of ensemble modeling to derive forecast uncertainties. Natras et al. (2022a, b) present novel ML approaches to forecast the ionospheric state including possible space weather impacts. A multi-model and multi-data ensemble forecasting approach was developed and applied using diverse models based on different ML algorithms and training datasets to generate 1-day VTEC forecasts (Natras et al., 2022a). This approach improves the forecasting accuracy compared to a single-model-based approach and provides forecast uncertainties by estimating the ensemble spread.

ML models can be used to forecast space weather events if sufficient input data on space weather events are available to allow suitable feature detection. In terrestrial weather forecasting, uncertainty quantification is usually achieved with ensemble forecasting systems performing multiple simulations, each with slightly different initial conditions and slightly perturbed weather models. Following this idea for space weather forecast, ML models based on different learning algorithms were developed and applied to different datasets. Their results are subsequently combined to produce a super ensemble (SE) model that provides not only reliable forecast results but also uncertainty information.

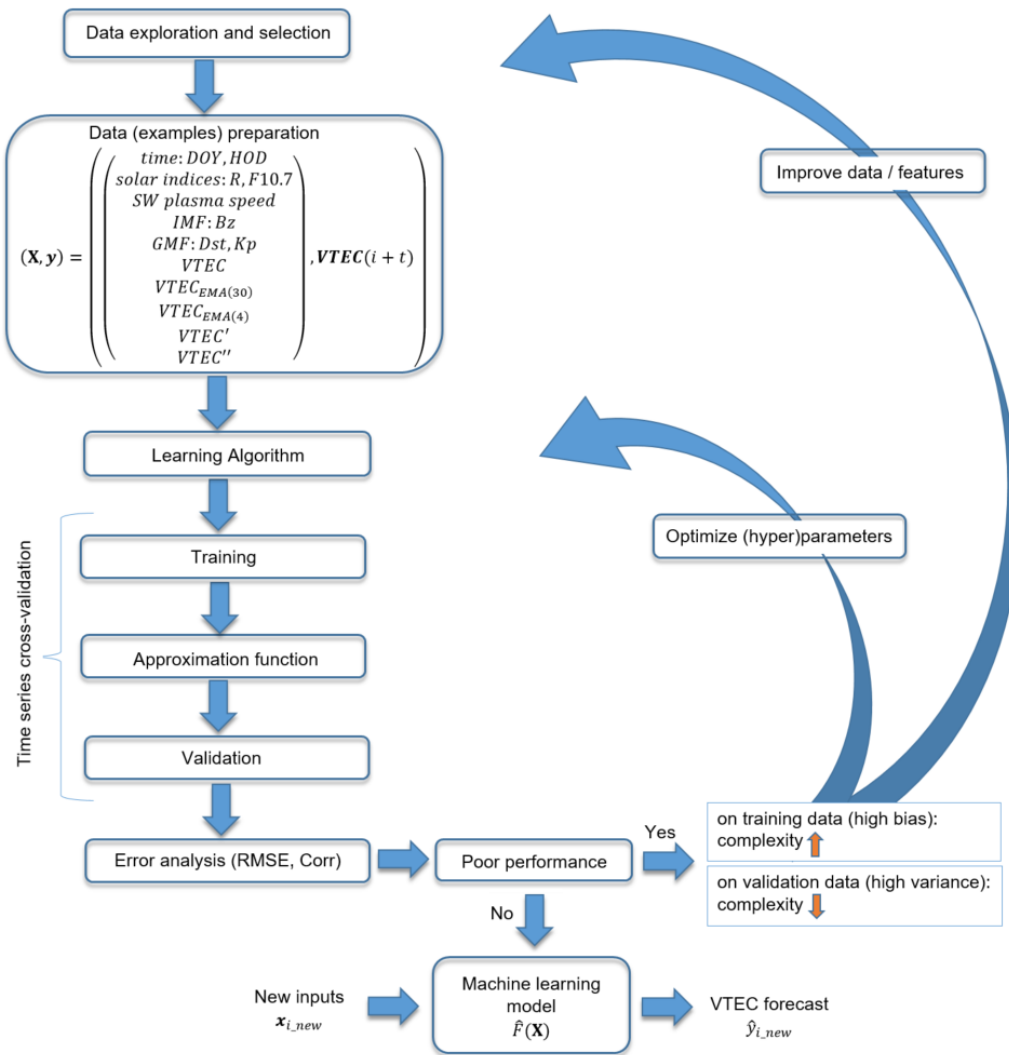


Figure 3.7: Flowchart of an ML model for VTEC forecast starting from data exploration, selection and preparation (top left) to training and cross-validation down to the final ML model identified with the approximation function $\hat{F}(\cdot)$ and optimized in terms of its performance. The final ML model can be used to forecast VTEC from new input data (bottom). The formulation $VTEC(i+t)$ means that VTEC values are forecasted to time moments $t_i + \Delta t$ where Δt is the forecast time step, e.g. 1 hour or 24 hours; see Natras et al. (2022b).

Each of the ML models for VTEC forecasting is based on supervised learning. The minimization of the objective cost function, represented as the RMSE between VTEC observations and corresponding VTEC values estimated from the ML model defines the performance measure. Supervised learning can be interpreted as the determination of a function $F(\cdot)$ that maps the $P \times 1$ input vector $\mathbf{x}_i = (x_{i,p})$ of P features at time moment t_i with $i \in \{1, 2, \dots, N\}$ into the output variable y_i (VTEC observations). During the learning phase, training and validation data are used to optimize model parameters and hyperparameters, and to estimate the approximation $\hat{F}(\cdot)$ of the function $F(\cdot)$ such that the estimated VTEC observations $\hat{y}_i = \hat{F}(\mathbf{x}_i)$ minimize the objective cost function. Figure 3.7 shows the development of a ML model for VTEC forecast. The features considered in the study (second box from the top) comprise ‘hour of day’ (HOD), ‘day of year’ (DOY), the ‘exponential moving average’ (EMA), the derivatives VTEC’ and VTEC” of VTEC and other quantities such as the solar flux index F10.7, geomagnetic field (GMF) indices Dst and Kp, and the interplanetary magnetic field (IMF) component Bz. If the error analysis indicates poor performance on training or validation data the complexity of the model should be increased or decreased, respectively. For details see Natras et al. (2022b).

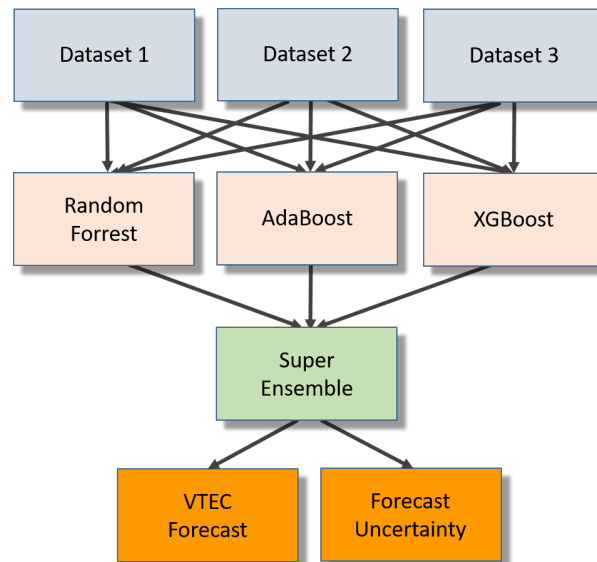


Figure 3.8: Flowchart of the ensemble modeling procedure, trained on 3 different datasets using the 3 different learning algorithms Random Forest (RF), AdaBoost and XGBoost. After the 9 individual model runs, the results are combined in a super-ensemble (SE) model which provides the VTEC forecast values and their uncertainty.

A numerical study on VTEC forecast to demonstrate ensemble modeling applies the procedure to a time period from January 2015 to December 2017. Training data covers the first two years while the testing is performed for 2017. Different learning algorithms were selected and applied to different datasets: (1) Random Forest (RF), (2) Adaptive Boosting (AdaBoost), (3) eXtreme Gradient Boosting (XGBoost). The three datasets are the original given data (Dataset 1), daily differences for both input and output data (Dataset 2) and input data combining the first and the second dataset, while the output data corresponds to the original VTEC data (Dataset 3). The idea behind is that daily differences remove the dominant VTEC variations, such that the ML models consider only the remaining structures associated with other sources of VTEC fluctuations such as space weather impacts. These 9 model runs are performed at 3 different locations reflecting high-latitude, mid-latitude and low-latitude regions. The solar and geomagnetic input data, i.e. solar wind, IMF and GMF data were taken from the NASA/GSFC OMNI-Web. VTEC time series for the 3 locations P_1 to P_3 were provided by CODE (Berne).

Figure 3.9 gives an overview of solar and geomagnetic activity during the week September 6 to 13, 2017, characterized by strong space weather events with Kp values around 8. Two minimum Dst values can be observed, namely at midnight and in the evening of September 8, representing the main phases of the geomagnetic storms. The recovery phase is following from September 9 to 11, to less stormy conditions on September 12 to 13. During September 6, the day before the initial phase of the first storm, the solar activity increased, while the GMF conditions were mostly quiet. The data from the five time series in Fig. 3.9 were used to forecast VTEC values of the following days with a forecast time step of $\Delta t = 24$ hours.

The individual 9 VTEC forecasts of the different ML models for the 3 locations P_k with $k = 1, 2, 3$ are the input data of the SE model (Fig. 3.8) which provides as output the time series $\mu_k(t)$ of the ensemble mean and the standard deviation $\sigma_k(t)$ for the 3 locations P_k . The ensemble spread is defined as the interval $[\mu_k(t) - 2 \cdot \sigma_k(t), \mu_k(t) + 2 \cdot \sigma_k(t)]$ which can be interpreted as the confidence interval of the time series $\mu_k(t)$ for the mean. The period September 7 to 12, 2017, covers the initial, main, and recovery phase of severe geomagnetic storms. The VTEC forecast uncertainty (green colored band defining the confidence interval in Fig. 3.10) is for all 3 locations P_k the largest during the main storm phases on September 8. Later, the confidence intervals narrow and thus, reduce the forecast uncertainty.

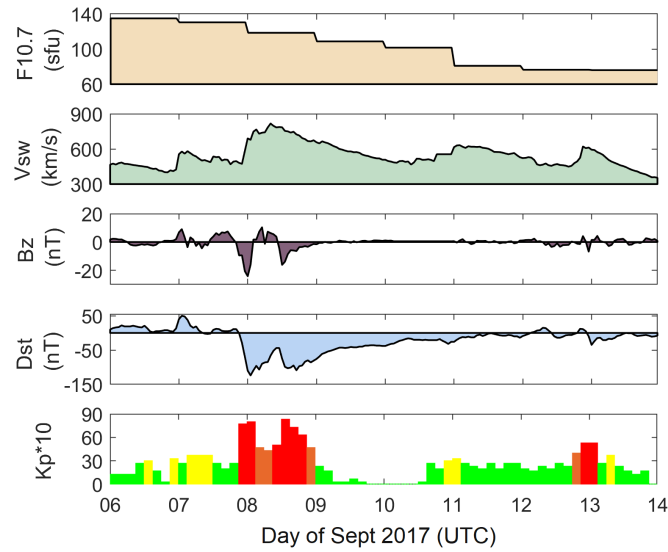


Figure 3.9: Solar radio flux $F10.7$ (in solar flux units (sfu)), solar wind speed V_{sw} , IMF component B_z (in nano Tesla (nT)), and the GMF indices Dst and K_p (multiplied by factor 10), for September 6 to 13, 2017. In the bottom panel quiet, moderate, active, and storm times are defined by K_p values $0 \leq K_p < 3$ (green), $3 \leq K_p < 4$ (yellow), $4 \leq K_p < 5$ (orange), and $5 \leq K_p \leq 9$ (red); Natras et al. (2022a).

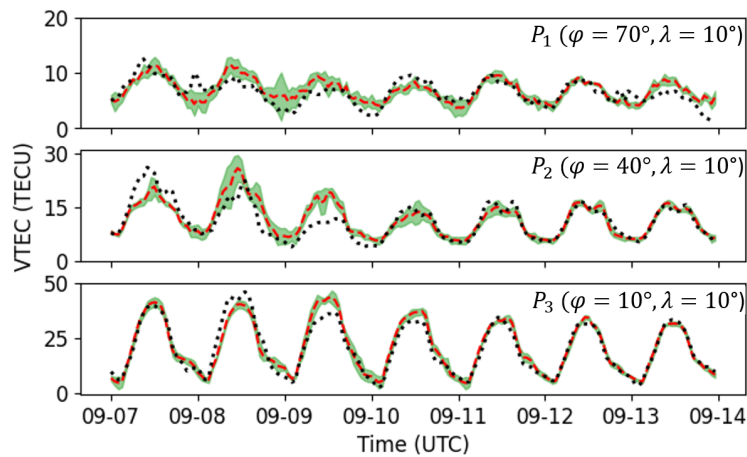


Figure 3.10: Time series of VTEC forecast $\mu_k(t)$ (red) computed with a forecast time step $\Delta t = 24$ hours from the SE model, confidence interval $[\mu_k(t) - 2 \cdot \sigma_k(t), \mu_k(t) + 2 \cdot \sigma_k(t)]$ (light green band) and VTEC time series of CODE (black dotted line) for September 7 to 13, 2017 at the 3 location P_k with $k = 1, 2, 3$; Natras et al. (2022a).

The VTEC time series at location P_1 , i.e. in high-latitude, is mainly given within, at or even outside the boundaries of the confidence interval. VTEC values are not error-free ‘true’ values but are given with standard deviations of a few TECU ($1 \text{ TECU} = 1 \cdot 10^{16} \text{ el/m}^2$). The VTEC time series at mid-latitude (location P_2) shows larger differences to the ensemble mean on September 7, the initial storm phase, when the VTEC forecast is underestimated, and on September 9, the beginning of the recovery phase, when the VTEC forecast is overestimated. In the main storm phase, VTEC is mostly given within the confidence interval. The ensemble mean is slightly overestimated during the main phase. During September 10 to 13, the mid-latitude VTEC values are within the confidence interval and correspond to the ensemble mean. For low-latitudes (location P_3), the differences between ensemble mean and VTEC time series are larger during daytime on September 8 and September 9. An overview of the RMSE values of the 3 individual ML models entering the SE model according to Fig. 3.7 and the mean values of the time series $2 \cdot \sigma_k(t)$ are provided in Tab. 3.3.

Table 3.3: RMSE of the difference between the VTEC values of CODE and the VTEC forecasts of the ensemble members Random Forest (RF), AdaBoost (AB), and XGBoost (XGB) applied to the three datasets 1 to 3, as well as the SE model forecast $\mu_k(t)$. The right column provides the mean values of the time series $2 \cdot \sigma_k(t)$. All data for the 3 locations P_k with $k = 1, 2, 3$, i.e. high-latitude, mid-latitude and low-latitude, refer to the time period September 7 to 13, 2017; the forecast time step is $\Delta t = 24$ hours.

location	dataset	RF [TECU]	AB [TECU]	XGB [TECU]	SE [TECU]	mean of $2 \cdot \sigma_k(t)$ [TECU]
P_1	1	1.62	1.67	1.78	1.63	0.90
	2	1.75	1.69	1.66		
	3	1.66	1.76	1.77		
P_2	1	3.08	3.05	3.00	2.80	1.28
	2	2.82	2.61	2.61		
	3	2.96	3.22	2.80		
P_3	1	3.14	3.38	3.20	3.13	1.60
	2	3.31	3.27	3.22		
	3	3.20	3.30	3.26		

Most of the time, the ensemble mean and confidence interval agree with the VTEC values. Largest differences occur during the initial storm phase and at the beginning of the recovery phase. Changes in the IMF and GMF data were short-term, and the input data from the previous day (September 6) does not contain enough information about these changes. However, during the main storm phase, the VTEC values do not deviate too much from the ensemble spread. After the storm, the ensemble spread is more narrow and the ensemble mean is in better agreement with the VTEC values.

Impact of scale factors on precise orbit determination of LEO satellites

Satellites in low-Earth orbits (LEO) are strongly influenced by atmospheric drag, which depends mainly on the density of the thermosphere. The interaction between thermosphere and satellite is described by thermosphere models in the precise orbit determination (POD). The **DFG project TIPOD** (see also Sect. 1.3) targets at the improvement of the POD of LEO satellites. In particular, SLR measurements to LEO satellites and on-board accelerometer (ACC) measurements have been shown to be suitable to improve thermospheric density information by scaling numerical model values. In the frame of TIPOD, scale factors were estimated for the empirical

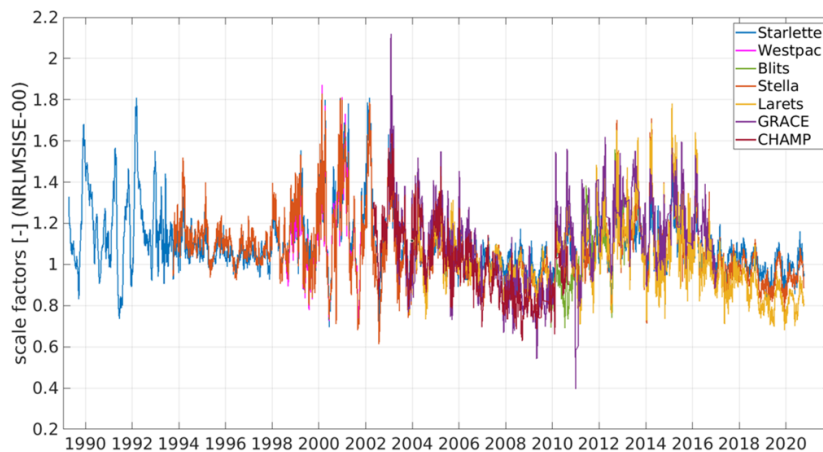


Figure 3.11: Time series of scale factors estimated from SLR and ACC. Variations within the time series are highly correlated with the temporal variations of the F10.7 solar activity index.

thermosphere model NRLMSISE-00 by DGFI-TUM from SLR measurements to various LEO satellites (Starlette, Westpac, Blits, Stella and Larets), while the Institute of Geoinformation and Geodesy (IGG) of the University of Bonn, cooperation partner within TIPOD, estimated scale factors from ACC measurements of CHAMP and GRACE⁶⁰.

To quantify the effect of thermospheric drag on the POD, two orbit solutions are computed for three LEO satellites (SpinSat, Larets, Stella) with mean altitudes of 425 km, 681 km and 798 km. One solution uses only density information provided by NRLMSISE-00 (i.e. scale factor = 1). For the second solution the model density was multiplied with estimated scale factors (Fig. 3.11). The norm of the orbit deviations are shown in Fig. 3.12 in dependence on time and satellite altitude. Lower satellite orbits that are stronger impacted by thermospheric drag show larger orbit deviations. After one week, the two orbit solutions deviate by about 12.5 m for Stella and almost 12 km for SpinSat. Both panels in Fig. 3.12 show a correlation between the thermospheric scale factor and the rate with which the orbit deviations increase. Scale factors close to 1 cause only a slight increase in orbit deviations (January 11 and 12, 2015), while large differences with respect to 1 lead to a rapid increase of the numerical values; see also Tab. 3.4. These results demonstrate impressively the necessity of considering reliable thermospheric drag corrections in POD.

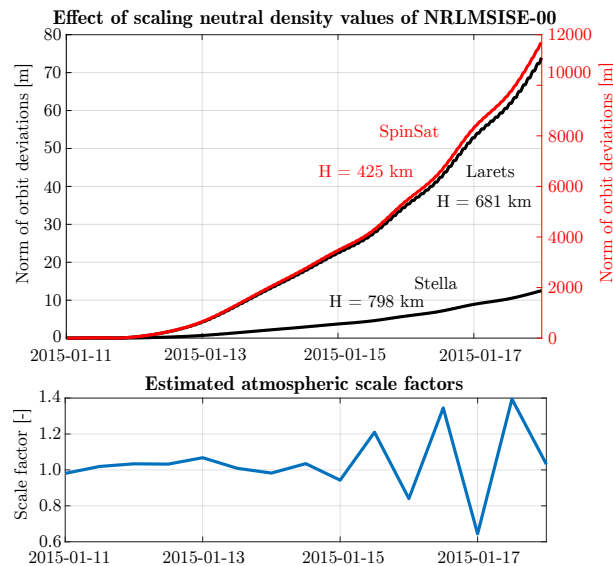


Figure 3.12: The norm of orbit deviations for three satellites SpinSat (orbital height $H = 425$ km), Larets ($H = 681$ km) and Stella ($H = 798$ km) for a period of one week (top). The deviations are obtained when multiplying the thermospheric density values from NRLMSISE-00 with the estimated scale factors (bottom).

Table 3.4: The norm of orbit deviations according to the number days after starting the 2 PODs.

day	Stella [m]	Larets [m]	SpinSat [m]
1	0.05	0.29	46
2	0.70	4.23	647
3	2.17	13.00	2,025
4	3.74	22.52	3,468
5	5.83	34.85	5,417
6	8.92	52.78	8,314
7	12.52	73.90	11,681

⁶⁰Zeitler L. et al. (2021): Scale factors of the thermospheric density: a comparison of Satellite Laser Ranging and accelerometer solutions. Journal of Geophysical Research, Space Physics, doi:10.1029/2021JA029708

Related publications

- Fernandez-Gomez I., Kodikara T., Borries C., Forootan E., Goss A., Schmidt M., Codrescu M.: *Improving estimates of the ionosphere during geomagnetic storm conditions through assimilation of thermospheric mass density*. Earth, Planets and Space, 74(121), doi:[10.1186/s40623-022-01678-3](https://doi.org/10.1186/s40623-022-01678-3), 2022
- Goss A.: *Generation of high-resolution global and regional multi-scale B-spline models of the vertical total electron content based on low-latency GNSS data*. Bayerische Akademie der Wissenschaften, DGK C 886, Dissertation, 2022
- Jerez G., Hernández-Pajares M., Goss A., da Silva C., Alves D., Monico J.: *Impact synergies of GIM error estimates on the VTEC interpolation and single-frequency PPP at low latitude region*. GPS Solutions, 26(2), doi:[10.1007/s10291-022-01228-0](https://doi.org/10.1007/s10291-022-01228-0), 2022
- Hernández-Pajares M., ..., Schmidt M., Goss A., Erdogan E., et al.: *Wide-Area GNSS Corrections for Precise Positioning and Navigation in Agriculture*. Remote Sensing, 14(16), doi:[10.3390/rs14163845](https://doi.org/10.3390/rs14163845), 2022
- Lalgudi Gopalakrishnan G., Schmidt M.: *Ionospheric electron density modelling using B-splines and constraint optimization*. Earth, Planets and Space, 74(1), doi:[10.1186/s40623-022-01693-4](https://doi.org/10.1186/s40623-022-01693-4), 2022
- Natras R., Soja B., Schmidt M.: *Machine Learning Ensemble Approach for Ionosphere and Space Weather Forecasting with Uncertainty Quantification*. 2022 3rd URSI Atlantic and Asia Pacific Radio Science Meeting (AT-AP-RASC), IEEE Xplore, doi:[10.23919/AT-AP-RASC54737.2022.9814334](https://doi.org/10.23919/AT-AP-RASC54737.2022.9814334), 2022a
- Natras R., Soja B., Schmidt M.: *Ensemble Machine Learning of Random Forest, AdaBoost and XGBoost for Vertical Total Electron Content Forecasting*. Remote Sensing, 14(15), 3547, doi:[10.3390/rs14153547](https://doi.org/10.3390/rs14153547), 2022b
- Qiu F.: *Estimation of electron density key parameters using the Multi-Layer Chapman Model considering inequality constraints from ionospheric radio occultation measurements*, Master thesis, Technical University Munich, 2022

3.2 Regional Gravity Field

Hundreds of local height systems exist worldwide, which can differ by more than 2 m. For both scientific and practical reasons, there is a growing need to establish a unified physical height reference system. In 2015, the IAG, with strong involvement of DGFI-TUM¹⁹, introduced the International Height Reference System (IHRs) as a global standard for determining physical heights, and its implementation is a current major goal of geodesy; see also Sect. 1.4. Research activities in this regard are addressed in the **DFG project Geo-H** (Enhanced geopotential field modeling as basis for the establishment of precise height systems), which has been running jointly at DGFI-TUM and TUM's Chair of Astronomical and Physical Geodesy since September 2021 as a continuation of the DFG project ORG4Heights.

The realization of the IHRs relies on high-resolution and high-precision regional gravity refinement. Different types of gravity measurements have not only different spatial resolution but also

different spectral sensitivities. The long-wavelength parts of the gravity field can only be evaluated by global satellite observations, while the short-wavelength parts are mainly detectable by other types of gravity observations, such as terrestrial and airborne data. The optimal combination of different measurement types is the key to obtaining high-resolution and high-precision regional gravity models. Current studies based on spherical radial basis functions (SRBFs) majorly consider a single-level approach for data combination. Despite the promising results reported in numerous publications⁶¹, it has been suspected in the existing literature that the single-level model might be biased towards the high-resolution measurements. To avoid this effect, a spectral combination can be implemented through a multi-resolution representation (MRR). The fundamental idea of the MRR is that the gravity signal is decomposed into an expansion in terms of spherical harmonics for the global long-wavelength part, and a number of detail signals in terms of wavelet functions for the regional medium and high frequency parts⁶². The MRR of a gravity functional $F(\mathbf{x})$ can be expressed as

$$F(\mathbf{x}) = \bar{F}(\mathbf{x}) + \sum_{i=i'}^I G_i(\mathbf{x}) + r(\mathbf{x}) \quad (3.17)$$

where $\bar{F}(\mathbf{x})$ is a reference model, usually the long-wavelength component from a global gravity model (GGM). In Eq. (3.17) $r(\mathbf{x})$ is the truncation error and $G_i(\mathbf{x})$ means the detail signal of resolution level $i = i', \dots, I-1, I$ defined as

$$G_i(\mathbf{x}) = \sum_{k=1}^{K_i} d_{k,i} \psi_i(\mathbf{x}, \mathbf{x}_{k,i}). \quad (3.18)$$

The position vectors $\mathbf{x}_{k,i}$ with $k = 1, 2, \dots, K_i$ are related to the level- i Reuter grid points where the spherical wavelet functions $\psi_i(\mathbf{x}, \mathbf{x}_{k,i})$ are centered and where the corresponding series coefficients $d_{k,i}$ are located.

Previous studies applying the MRR approach (3.17) estimated the coefficients $d_{k,i}$ defined in Eq. (3.18) for each level i independently, using all or selected groups of observations⁶³. However, if all observation types are used at each level, the corresponding detail signals are strongly correlated. If only specific data sets are used, large data gaps may occur, and the prior information is insufficient for filling these data gaps at higher resolution levels. This leads to large erroneous effects in the output signals. To avoid such issues, a pyramid algorithm can be applied to consider all available information by connecting the different levels.

Pyramid algorithm

The pyramid algorithm determines the coefficients of the lower resolution levels from the coefficients of the higher level by a low-pass filtering. With the pyramid algorithm, the coefficients at level i ($i = i', i' + 1, \dots, I-2, I-1$) can be expressed as

$$\mathbf{d}_{i|i+1} = \mathbf{L}_i \mathbf{d}_{i+1} \quad (3.19)$$

$$\boldsymbol{\Sigma}_{\mathbf{d}_{i|i+1}} = \mathbf{L}_i \boldsymbol{\Sigma}_{\mathbf{d}_{i+1}} \mathbf{L}_i^T \quad (3.20)$$

where \mathbf{L}_i is a $K_i \times K_{i+1}$ low-pass filter matrix, transforming the $K_{i+1} \times 1$ coefficient vector \mathbf{d}_{i+1} of the level $i+1$ into the $K_i \times 1$ coefficient vector $\mathbf{d}_{i|i+1}$ of the lower level i . $\boldsymbol{\Sigma}_{\mathbf{d}_{i|i+1}}$ is the covariance

⁶¹Liu Q. et al. (2020): *Regional gravity field refinement for (quasi) geoid determination based on spherical radial basis functions in Colorado*. Journal of Geodesy, doi:10.1007/s00190-020-01431-2

⁶²Schmidt M., et al. (2007): *Regional gravity modeling in terms of spherical base functions*. Journal of Geodesy, doi:10.1007/s00190-006-0101-5

⁶³Lieb V. (2017): *Enhanced regional gravity field modeling from the combination of real data via MRR*. Dissertation, Technical University of Munich

matrix of $\mathbf{d}_{i|i+1}$ obtained from the covariance matrix $\Sigma_{\mathbf{d}_{i+1}}$ following the law of error propagation. The low-pass filter matrix \mathbf{L}_i can be decomposed as

$$\mathbf{L}_i = \mathbf{W}_i \mathbf{H}_i \quad (3.21)$$

where \mathbf{H}_i is a $K_i \times K_{i+1}$ matrix containing the reproducing kernel $K_{rep}(\mathbf{x}_{k,i}, \mathbf{x}_{k,i+1})$ between the grid points $P_{k,i+1}$ ($k = 1, 2, \dots, K_{i+1}$) of level $i + 1$ and the grid points $P_{k,i}$ ($k = 1, 2, \dots, K_i$) of level i . \mathbf{W}_i is the $K_i \times K_i$ diagonal matrix of the integration weights associated with the grid points $P_{k,i}$ of level i , and it depends on the implemented type of grid. Liu et al. (2022b) developed a strategy to set up the corresponding integration weights in case of using the Reuter grid, which read

$$w_i = \frac{4\pi R^2}{Z_i} \quad (3.22)$$

where Z_i is the number of the Reuter grid points on the sphere at level i . Based on the pyramid algorithm, a new MRR scheme is developed using sequential parameter estimation (Liu 2022a), see Fig. 3.13. The initial step of the developed MRR procedure is to estimate the unknown coefficient vector \mathbf{d}_I and its covariance matrix $\Sigma_{\mathbf{d}_I}$ at the highest resolution level I using only the high-resolution gravity data⁶⁴. Then, they are used to calculate the coefficient vector $\mathbf{d}_{I-1|I}$ and the corresponding covariance matrix $\Sigma_{\mathbf{d}_{I-1|I}}$ of the next lower level $I - 1$, by applying the pyramid algorithm according to the Eqs. (3.19) and (3.20). Instead of transforming the coefficient vector $\mathbf{d}_{I-1|I}$ directly to the next lower level $I - 2$, it is updated by the gravity observations \mathbf{y}_{I-1} introduced at this level $I - 1$ through parameter estimation. The combination of \mathbf{y}_{I-1} and $\mathbf{d}_{I-1|I}$ is in analogy to the Kalman filter, where $\mathbf{d}_{I-1|I}$ is the predicted state vector and \mathbf{d}_{I-1} is the corrected state vector after incorporating the involved measurements. The updated coefficient vector $\hat{\mathbf{d}}_{I-1}$ is then used for calculating the detail signal $\hat{\mathbf{G}}_{I-1}$ at level $I - 1$ and for determining the coefficient vector $\hat{\mathbf{d}}_{I-2|I-1}$ of level $I - 2$ by the Eqs. (3.19) and (3.20). Continuing this process until the lowest resolution level, each observation type is introduced into the MRR scheme, and the coefficients as well as the detail signals of each level can be obtained. By continuing this process to the lowest level of resolution, each observation type is introduced into the MRR scheme, and the coefficients and detail signals of each level can be determined.

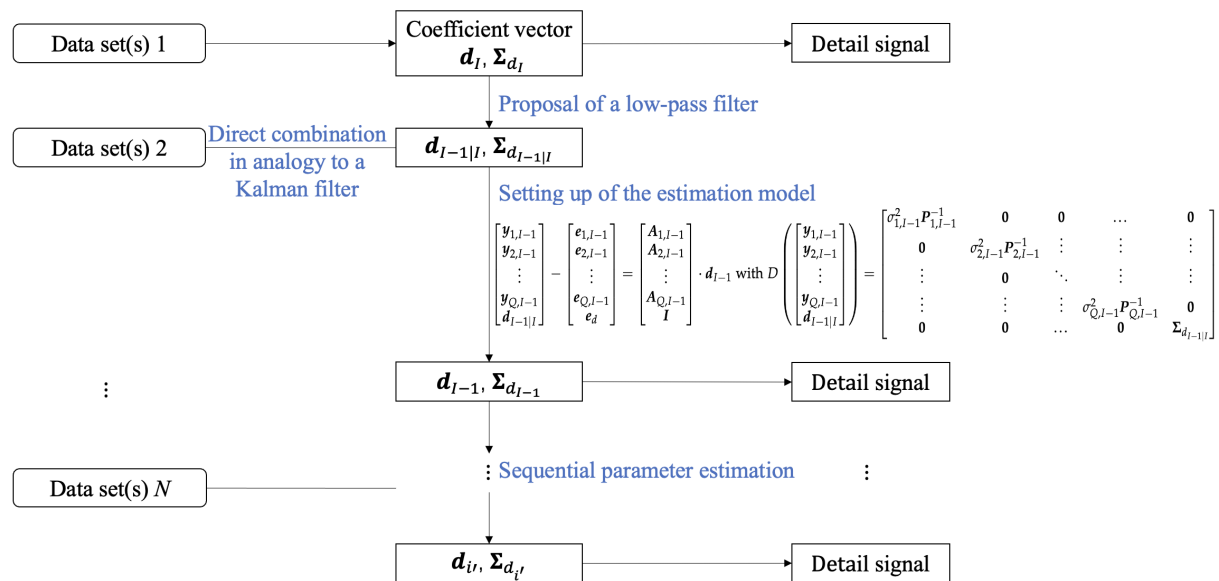


Figure 3.13: MRR scheme based on the pyramid algorithm; blue text highlights novelties

⁶⁴Liu Q., et al. (2020): *Determination of the regularization parameter to combine heterogeneous observations in regional gravity field modeling*. Remote Sensing, doi:10.3390/rs12101617

The main advantage of applying the MRR based on the pyramid algorithm is that different observation types can now be introduced into the evaluation model at the spectral level of their highest sensitivities. Furthermore, the covariance information can be calculated following the law of error propagation from the higher levels and serve as input for the lower levels.

Numerical evaluation

The new MRR scheme is applied for regional gravity refinement using real gravity measurements. Its performance is compared with both the single-level SRBF approach and the MRR without pyramid algorithm, i.e., the coefficients are estimated at each resolution level using all types of observations. Figure 3.14 shows the study area, covering Northern Germany, parts of the North Sea and Baltic Sea, and a small part of the Netherlands and Denmark. Gravity measurements were provided by BKG and the federal states Schleswig-Holstein, Mecklenburg West-Pomerania, and Lower Saxony. These data are taken from Lieb et al. (2016)⁶⁵, where in contrast to this study, the combination was done in a single-level manner (see also Annual Report 2015). Terrestrial data (yellow points) and shipborne data (red points) are used in terms of gravity anomalies Δg , airborne data (orange points) are used in terms of gravity disturbance δg , and altimetry data (green points) are used in terms of geoid height N . The altimetry data (from DGFI-TUM) contain observations from the missions ERS-1, Envisat, Jason-1, and Cryosat.

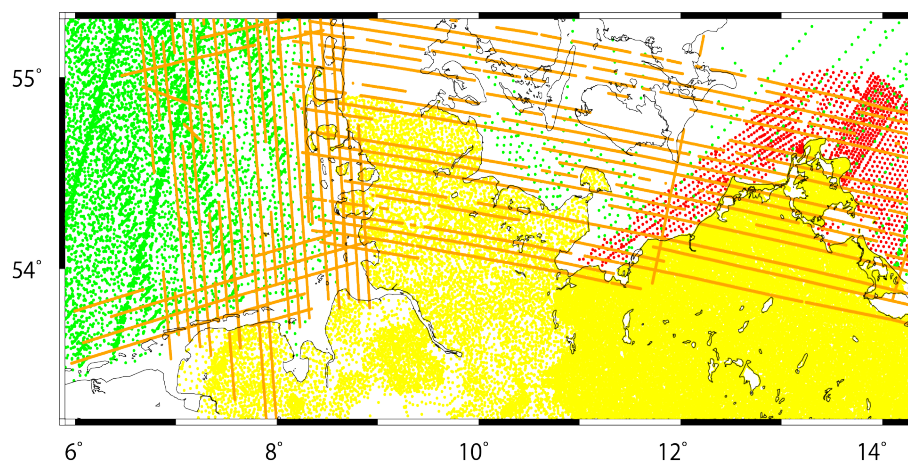


Figure 3.14: Study area and available gravity measurements, including terrestrial (yellow), shipborne (red), airborne (orange), and altimetry (green) data

The terrestrial, shipborne, airborne, and altimetry data are included in the estimation model at the levels 12, 11, 10, and 9, respectively. The long-wavelength component up to level 8 is modeled using the remove-compute-restore (RCR) procedure with GOCO06s, which enhances an optimal combination of the GOCE and GRACE data. Validations are made using GPS/leveling data in Northern Germany and the $2' \times 2'$ altimetric gravity anomaly grid DTU17 in the offshore area. Figure 3.15 shows the differences between the calculated quasi-geoid model and the GPS/leveling data, delivered by the single-level approach (Fig. 3.15a), the MRR without pyramid algorithm (Fig. 3.15b), and the MRR based on the pyramid algorithm (Fig. 3.15c). Note that the mean values (around 33 cm) of the differences are removed, which is caused by differences in the height system definition. The corresponding statistics are listed in Tab. 3.5. The MRR based on the pyramid algorithm delivers the smallest difference with respect to the GPS/leveling data with an RMS error of 2.23 cm, which is 23% smaller than the one given by the MRR without pyramid algorithm, and 35% smaller than that of the single-level model.

⁶⁵Lieb V., et al. (2016): *Combination of various observation techniques for regional modeling of the gravity field*. Journal of Geophysical Research, Solid Earth, doi:10.1002/2015JB012586

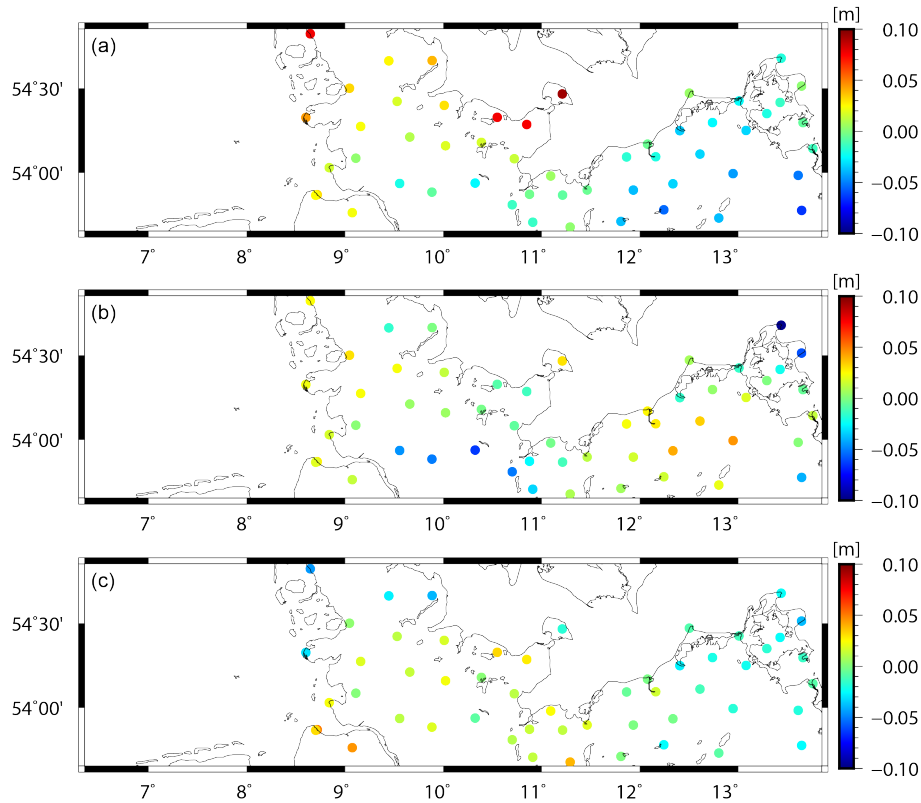


Figure 3.15: Differences between the calculated quasi-geoid model and the GPS/leveling data, delivered by (a) the single-level approach, (b) the MRR without pyramid algorithm, and (c) the MRR based on the pyramid algorithm. Mean values of the differences are removed

Figure 3.16 shows the differences between the computed gravity anomaly results and DTU17 in the offshore area, and the corresponding statistics are listed in Table 3.5. Again, the largest differences are delivered by the single-level approach (Fig. 3.16a), with an RMS error of 7.22 mGal. In the single-level model, much smaller differences show up in regions with shipborne data coverage (see Fig. 3.14), which suggests that it majorly recovers gravity information from the high-resolution shipborne data, and information from other measurement types are not captured sufficiently. In comparison to the single-level model, applying the MRR (without pyramid algorithm) improves the modeling results by 13%. Comparing Fig. 3.16b with Fig. 3.16a reveals improvements in regions with altimetry data (between 6.35° and 7° longitude). This indicates

Table 3.5: Comparison between single-level approach, MRR without pyramid algorithm and MRR based on the pyramid algorithm w.r.t. GPS/leveling data (in terms of quasi-geoid; mean differences are removed) and w.r.t. the DTU17 grid (in terms of gravity anomaly)

	w.r.t. GPS/leveling data (unit [cm])			w.r.t. the DTU17 grid (unit [mGal])		
	Min	Max	RMS	Min	Max	RMS
Single-level	-6.48	9.36	3.43	-53.24	60.46	7.22
MRR without pyramid algorithm	-9.70	4.57	2.88	-44.17	39.63	6.25
MRR based on pyramid algorithm	-4.50	5.15	2.23	-7.98	8.70	2.67

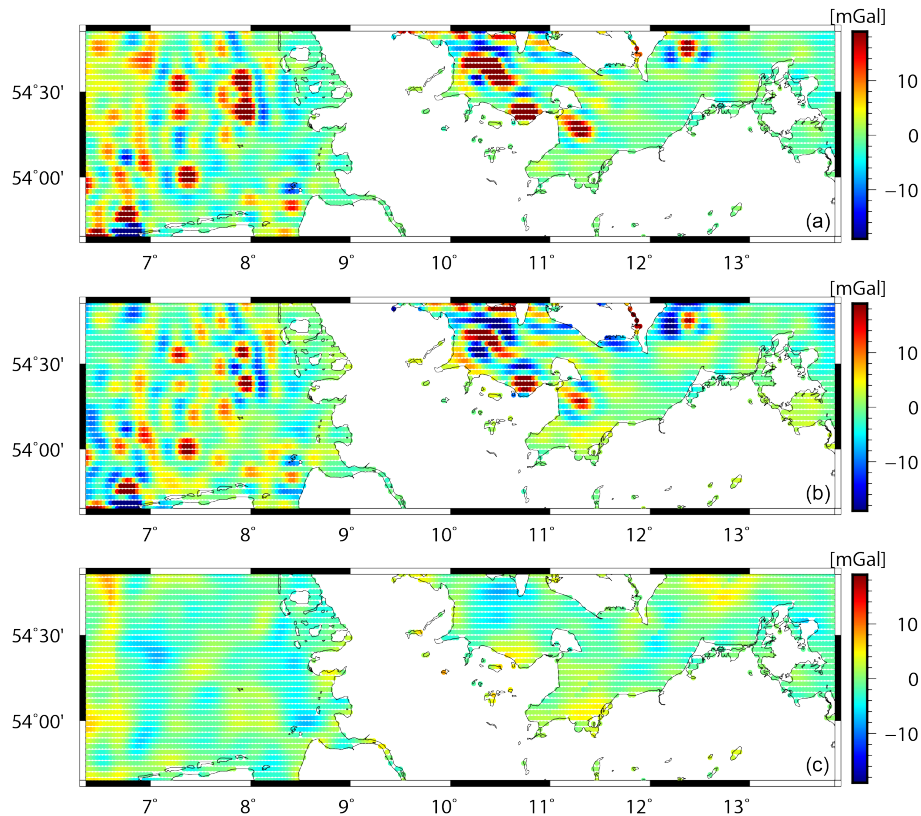


Figure 3.16: Differences between calculated gravity anomalies and the DTU17 grid in the offshore area, delivered by (a) the single-level approach, (b) the MRR without pyramid algorithm, and (c) the MRR based on the pyramid algorithm

that the MRR extracts gravity information from the lower resolution altimetry data better than the single-level approach. However, it can still be seen from Fig. 3.16b that larger differences occur in regions without shipborne data coverage. Even though the MRR without pyramid algorithm already gives better results than the single-level approach, it is not optimal. When the MRR based on the pyramid algorithm is applied, the differences with respect to DTU17 are significantly reduced, giving an RMS of 2.67 mGal, which is 57% smaller than the one delivered by the MRR without pyramid algorithm, and 63% smaller than that of the single-level approach. This demonstrates the benefits of applying the MRR based on the pyramid algorithm. Furthermore, the improvement achieved by applying the MRR based on the pyramid algorithm is larger in the offshore area than in the onshore area, where high-resolution terrestrial data are available. Neither the single-level approach nor the MRR without pyramid algorithm can represent the lower-resolution data in an optimal way. The MRR scheme based on the pyramid algorithm is beneficial, especially in regions without large coverage of high-resolution gravity data.

Related publications

Liu Q.: *Regional gravity field refinement for geoid height modeling based on the combination of data from various observation techniques*. Bayerische Akademie der Wissenschaften, DGK C 896, Dissertation, 2022a

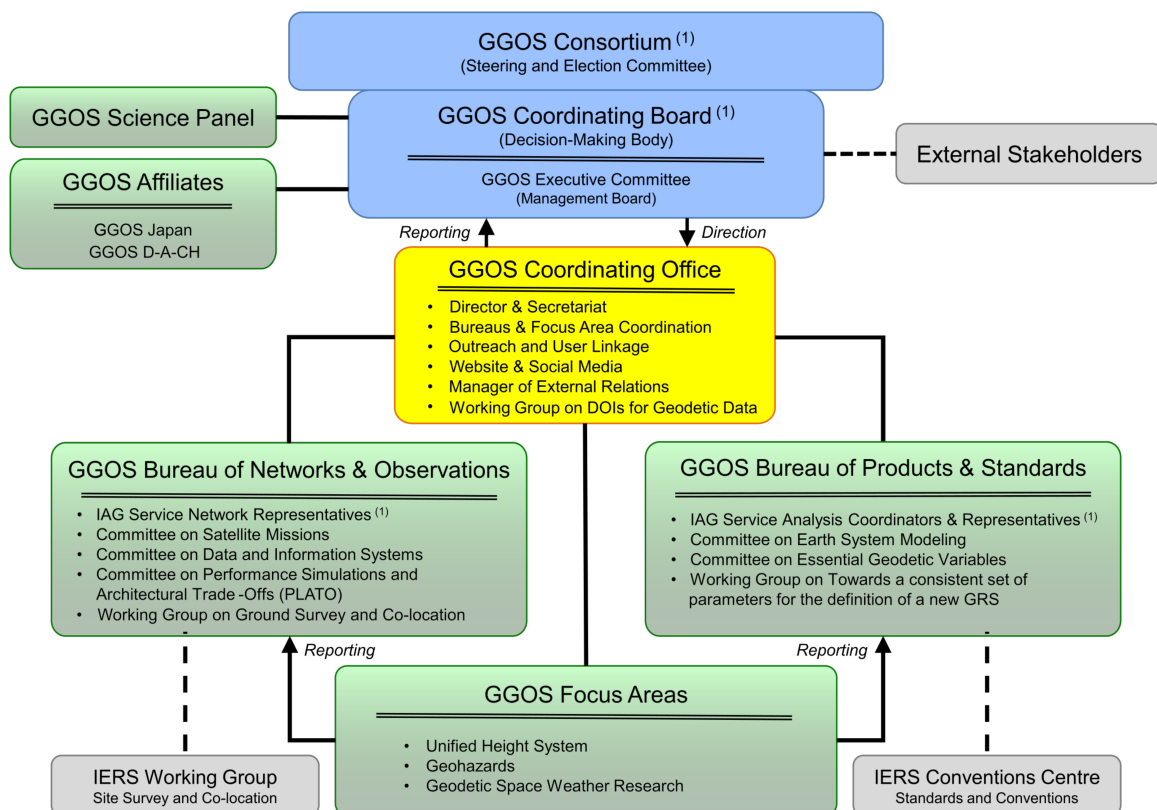
Liu Q., Schmidt M., Sánchez L.: *Combination of different observation types through a multi-resolution representation of the regional gravity field using the pyramid algorithm and parameter estimation*. Journal of Geodesy, 96(10), doi:10.1007/s00190-022-01670-5, 2022b

3.3 Standards and Conventions

With the progressive technological development of Earth observation systems, geodesy is opening up an increasing potential to unambiguously determine the geometric shape of land, sea, and ice surfaces as well as the rotation and gravity field of the Earth as global functions of space and time. Based on its comprehensive space- and ground-based infrastructure, geodesy provides the metrological basis for studying the Earth system and reliably monitoring geodynamics and climate change phenomena. Under the umbrella of the Global Geodetic Observing System (GGOS), the IAG strives to provide geodetic results at the highest level of precision and consistency. This fundamentally requires that the processing and combination of the contributing geometric and gravimetric observations are based on uniform standards and conventions. The definition and implementation of uniform standards and conventions has played an important role in DGFI-TUM research for many years.

For more than a decade, DGFI-TUM has been a key contributor to GGOS. The institute plays a major role in defining and implementing uniform standards and conventions by chairing the GGOS Bureau of Products and Standards (BPS; Director: Dr. Detlef Angermann). The BPS is one of two GGOS bureaus, along with the Bureau of Networks and Observations (BNO), which is chaired by the Harvard Smithsonian Center for Astrophysics, USA. Across all IAG components, the BPS evaluates the adopted standards and conventions used to create high-quality scientific data products for scientific and societal applications.

Within GGOS, DGFI-TUM also provides the GGOS Vice President (Dr. Laura Sánchez) and chairs two of the three GGOS Focus Areas (FA): The FA Unified Height System (Chair: Dr.



(1) GGOS is built upon the foundation provided by the IAG Services, Commissions, and Inter-Commission Committees

Figure 3.17: Organizational structure of IAG's Global Geodetic Observing System (GGOS).

Laura Sánchez; see Section 1.4) and the FA Geodetic Space Weather Research (Chair: Prof. Michael Schmidt; see Section 3.1). The third FA Geohazards is chaired by NASA. DGFI-TUM also participates in the GGOS Affiliate *GGOS D-A-CH* (founded in 2021), which bundles the GGOS-related activities of the D-A-CH region (Germany, Austria, Switzerland) in terms of science and infrastructure. The organizational structure of GGOS is shown in Figure 3.17.

GGOS Bureau of Products and Standards

The BPS is chaired by DGFI-TUM and operated jointly with TUM's Chair of Astronomical and Physical Geodesy within the Research Group Satellite Geodesy (Forschungsgruppe Satellitengeodäsie, FGS). GFZ (German Research Centre for Geosciences, Potsdam) and DLR (German Aerospace Centre, Oberpfaffenhofen) are further involved partners.

The mission and overall objectives of the BPS are to

- serve as coordinating point for the homogenization of IAG standards and products,
- keep track of the adopted standards and conventions across all components of the IAG,
- motivate the development of new and integrated geodetic products, needed for Earth sciences and society,
- describe and promote geodetic results (see below).

In its current structure, the following GGOS entities are associated to the BPS:

- Committee 'Contributions to Earth System Modeling',
- Committee 'Definition of Essential Geodetic Variables (EGVs)',
- Working Group 'Towards a consistent set of parameters for the definition of a new Geodetic Reference System (GRS)'.

The BPS supports GGOS in its goal of obtaining consistent scientific data products that include the geometry, rotation, gravity field, and other parameters of the Earth system, including their changes over time.

An overview and schedule of BPS tasks in the categories of (1) Coordination activities, (2) Specific BPS tasks, and (3) Outreach activities is shown in the BPS Implementation Plan 2020–2022 (Fig. 3.18), which is currently being updated for the next period 2023–2026.

To achieve its objectives, close collaboration has been established between the BPS and the IAG Scientific Services, the IERS Conventions Center and other entities involved in standards and conventions such as the International Astronomical Union (IAU) Commission A3 'Fundamental Standards', the International Organization for Standardization (ISO/TC 211) and the United Nation Global Geospatial Information Management (UN-GGIM) Subcommittee on Geodesy (SCoG) Working Group 'Data Sharing and Development of Geodetic Standards'.

Description and representation of geodetic science products

In collaboration with the IAG and other GGOS components, the BPS has created user-friendly descriptions for geodetic science data products and implemented them on the GGOS portal (www.ggos.org). In this way, GGOS serves to promote the contributions of geodesy to Earth system research (Angermann et al., 2022a). The data products are divided into two categories:

- **Geodetic themes:** Reference frames, Earth's geometry, orientation and gravity field, positioning and applications.
- **Earth system components and space:** Outer and near space, atmosphere, hydrosphere, oceans, cryosphere, solid Earth.

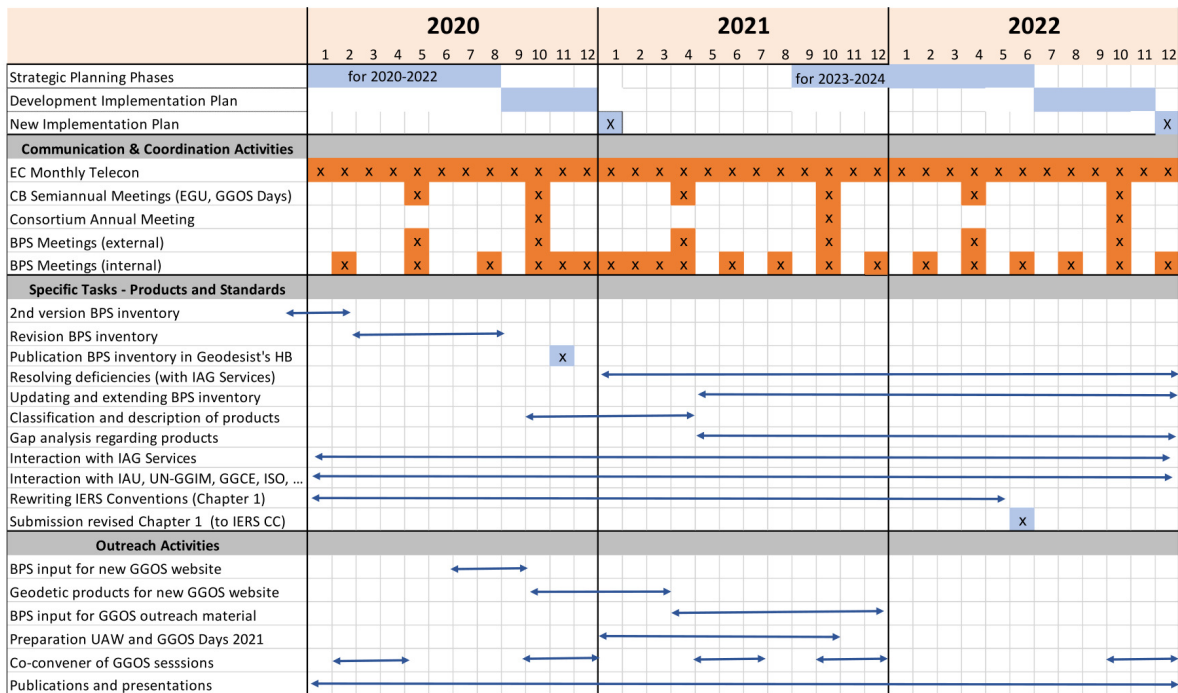


Figure 3.18: Overview and schedule of BPS activities.

BPS contributes to updating the IERS Conventions

In 2022, the BPS and the IERS Conventions Center organized a special meeting on standards, conventions, and formats, specifically to update Chapter 1 of the IERS Conventions ‘General Definitions and Numerical Standards’. One topic was the treatment of the permanent tide in heights as specified in the IERS definition (see Section 1.4), which prescribes IHRF coordinates in the mean-tide system to support oceanographic and hydrographic modeling. Section 1.1 ‘Permanent Tides’ of the IERS Conventions will be updated accordingly to reference these IERS developments. In addition, the current status of numerical standards (Section 1.2 of the IERS Conventions) was addressed. Several updates were proposed and will be incorporated to reflect recent changes in the field of standards and conventions (Angermann et al., 2022b).

As outlined in the BPS inventory of standards and conventions⁶⁶, also within IAG different numerical standards, time systems and tide systems are still in use. Such inconsistencies are a potential source of error when combining different data. Therefore, the IAG is considering the need and appropriateness of replacing the GRS80 with a new geodetic reference system. To this end, the GGOS Working Group ‘Towards a consistent set of parameters for the definition of a new GRS’ has been established as part of the BPS.

GGOS Days 2022 and Strategic Plan Workshop

From November 15-16, the GGOS Days 2022 and the Strategic Plan Workshop took place at the premises of the Bavarian Academy of Sciences and Humanities (BAW) in downtown Munich. The events were organized by GGOS in cooperation with the TUM and the German Geodetic Commission (DGK). A total of 111 scientists from around the world participated in the GGOS Days 2022 and discussed new geodetic technologies and methodologies, as well

⁶⁶Angermann D. et al. (2020): *Bureau of Products and Standards: Inventory of standards and conventions used for the generation of IAG products*. Journal of Geodesy, doi:10.1007/s00190-020-01434-z

as the contributions of geodesy to the monitoring of climate change phenomena and geodynamics. Detailed information is available on the GGOS website (<https://ggos.org/event/ggos-days-2022/>) which also includes links to download presentations, videos, and photos from the conference. Following the 2022 GGOS Days, the GGOS Strategic Plan Workshop was convened at the same venue. Approximately 20 invited IAG representatives attended this workshop to discuss the future direction and goals of GGOS.



Figure 3.19: On-site participants of GGOS Days 2022.

Related publications

Angermann D., Gruber T., Gerstl M., Heinkelmann R., Hugentobler U., Sánchez L., Steigenberger P., Gross R., Heki K., Marti U., Schuh H., Sehnal M., Thomas M.: *GGOS Bureau of Products and Standards: Description and Promotion of Geodetic Products*. In: Freymueller J., Sánchez L. (Eds.), *IAG Symposia*, Springer, doi:[10.1007/1345_2022_144](https://doi.org/10.1007/1345_2022_144), 2022a

Angermann D., Gruber T., Gerstl M., Heinkelmann R., Hugentobler U., Sánchez L., Steigenberger P.: *GGOS of Products and Standards (BPS): BPS Activities on Standards*. Unified Analysis Workshop 2022, Thessaloniki, Greece, doi:[10.5281/zenodo.7291721](https://doi.org/10.5281/zenodo.7291721), 2022b

4 Scientific Transfer

The transfer of knowledge, scientific results and data within the scientific community and to the public is an essential element of scientific work. Strong involvement in scientific organizations and networking in collaborative research programs at national and international level is a long-standing important pillar in the international strategy of DGFI-TUM. Scientific publications and presentations, participation in scientific meetings, guest visits and the operation of internet and data portals are the most important instruments of cross-disciplinary information exchange.

Section 4.1 contains a compilation of the positions and involvement of DGFI-TUM staff in national and international scientific organizations. The institute is intensively networked with other institutions worldwide, in particular through research activities within the International Union of Geodesy and Geophysics (IUGG), the International Astronomical Union (IAU), and the International Association of Geodesy (IAG). DGFI-TUM is a major player in the IAG's Global Geodetic Observing System (GGOS) (cf. Section 3.3) and operates research centers, analysis centers, and data centers, mostly on the basis of long-term commitments (cf. Section 1). Scientists of DGFI-TUM participate in various collaborative projects, working and study groups, and assume numerous key leadership and management positions to actively shape the future direction of international geodetic research.

Section 4.2 provides the scientific publications of the year 2022. Section 4.3 contains the list of posters and talks given by DGFI-TUM scientists at the numerous national and international conferences, symposia and workshops listed in Section 4.4. Guests who visited DGFI-TUM as part of research collaborations in 2022 are listed in Section 4.5. To share scientific information and data with partners and the interested public, DGFI-TUM maintains several websites, public databases, and social media channels. An overview of the portals operated is given in Section 4.6.

4.1 Functions in Scientific Bodies

United Nations Global Spatial Information Management (UN-GGIM)

- Subcommittee Geodesy, Working Group for a Global Geodetic Reference Frame (GGRF), *IAG Representative for Key Area Data Sharing and Development of Standards: Angermann D.*

International Astronomical Union (IAU)

- Commission A.2, Rotation of the Earth, *Immediate Past President and Senior Advisor: Seitz F., Member: Seitz M.*
- Joint IAU CA.2/IAG/IERS Working Group Consistent Realization of TRF, CRF and EOP, *Co-Chair: Seitz M., Member: Seitz F.*
- Joint IAU CA.2/IAG Working Group Improving Theories and Models of the Earth's Rotation, *Member: Seitz F.*

International Union of Geodesy and Geophysics (IUGG)

- *Representative to the Panamerican Institute for Geodesy and History (PAIGH), Sánchez L.*

International Association of Geodesy (IAG)

- Global Geodetic Observing System (GGOS),
Vice-President: Sánchez L.
- Global Geodetic Observing System (GGOS) Executive Committee,
Member: Angermann D., Sánchez L.
- Global Geodetic Observing System (GGOS) Coordinating Board,
Member: Angermann D., Sánchez L., Schmidt M.
- Global Geodetic Observing System (GGOS) Bureau of Products and Standards,
Director: Angermann D., Member: Sánchez L.
- Global Geodetic Observing System (GGOS) Focus Area Unified Height System,
Lead: Sánchez L.
- Global Geodetic Observing System (GGOS) Focus Area Geodetic Space Weather Research,
Lead: Schmidt M.
- Global Geodetic Observing System (GGOS) Bureau of Products and Standards, Working Group Towards a consistent set of parameters for the definition of a new GRS,
Member: Angermann D., IHRF representative: Sánchez L.
- Global Geodetic Observing System (GGOS) Focus Area Unified Height System, Joint Working Group Implementation of the International Height Reference Frame (IHRF),
Chair: Sánchez L., Member: Liu Q.
- Global Geodetic Observing System (GGOS) Focus Area Geodetic Space Weather Research, Joint Working Group 1 Electron density modelling,
Member: Gerzen T., Schmidt M.
- Global Geodetic Observing System (GGOS) Focus Area Geodetic Space Weather Research, Joint Working Group 2 Improvement of thermosphere models,
Member: Schmidt M.
- Global Geodetic Observing System (GGOS) Focus Area Geodetic Space Weather Research, Joint Working Group 3 Improved understanding of space weather events and their monitoring by satellite missions,
Member: Dettmering D.
- Global Geodetic Observing System (GGOS) Working Group on DOIs for Geodetic Data,
Member: Angermann D., Schwatke C.
- Global Geodetic Observing System (GGOS) Working Group on Performance Simulations and Architectural Trade-Offs (PLATO),
Member: Bloßfeld M., Kehm A.
- Global Geodetic Observing System (GGOS) Committee Essential Geodetic Variables,
Member: Angermann D.
- IAG Symposia Series,
Assistant Editor-in-Chief: Sánchez L.
- Commission 1, Sub-Commission 1.4 Interaction of celestial and terrestrial reference frames,
Member: Seitz M.
- Commission 1, Working Group 1.2.1 Assessing impacts of loading on reference frame realizations,
Member: Seitz, M.

- Commission 2, Joint Working Group 2.1.1 Establishment of the International Gravity Reference Frame,
Corresponding member, IHRF representative: Sánchez L.
- Commission 2, Joint Working Group 2.2.2 Error assessment of the 1 cm geoid experiment,
Member: Liu Q., Sánchez L.
- Commission 2, Sub-Commission 2.5.4: International Altimeter Service Planning Group,
Member: Schwatke C.
- Commission 4, Sub-Commission 4.3 Atmosphere Remote Sensing,
Chair: Schmidt M.
- Commission 4, Working Group 4.3.3 Ionosphere Scintillations,
Member: Schmidt M.
- Inter-Commission Committee on Theory (ICCT), Joint Study Group T.26 Geoid/quasi-geoid modelling for realization of the geopotential height datum,
Member: Sánchez L.
- Inter-Commission Committee on Theory (ICCT), Joint Study Group T.29 Machine learning in geodesy,
Member: Natras R.
- Inter-Commission Committee on Theory (ICCT), Joint Study Group T.33 Time series analysis in geodesy and geodynamics,
Member: Schmidt M.

International Earth Rotation and Reference Systems Service (IERS)

- Directing Board,
Associate member: Angermann D., Bloßfeld M.
- ITRS Combination Center,
Chair: Seitz M., Member: Bloßfeld M.
- Working Group on SINEX Format,
Member: Seitz M.
- Working Group on Site Coordinate Time Series Format,
Member: Seitz M.

International Laser Ranging Service (ILRS)

- Governing Board,
Member: Bloßfeld M., Schwatke C.
- Analysis Center,
Co-Chair: Bloßfeld M.
- Analysis Center Representative to ILRS Governing Board,
Bloßfeld M.
- Analysis Standing Committee,
Member: Bloßfeld M., Kehm A., Schwatke C.
- EUROLAS Data Center (EDC),
Chair: Schwatke C.
- Data Centers Representative to ILRS Governing Board,
Schwatke C.

- Operations Center,
Chair: Schwatke C.
- Data Formats and Procedures Standing Committee,
Chair: Schwatke C.
- Networks and Engineering Standing Committee,
Member: Schwatke C.
- Study Group on Data Format Update,
Member: Schwatke C.
- Study Group on ILRS Software Library,
Member: Schwatke C.
- ILRS Representative to the World Data System,
Schwatke C.
- ILRS Technique Center Representative to IERS Directing Board,
Bloßfeld M.

International VLBI Service for Geodesy and Astrometry (IVS)

- Operational Analysis Center,
Member: Glomsda M., Seitz M.
- IVS Combination Center,
Member: M. Seitz

International DORIS Service (IDS)

- Governing Board,
Member: Dettmering D.
- Associate Analysis Center,
Member: Bloßfeld M., Rudenko S.
- DORIS Analysis Working Group,
Member: Rudenko S.
- Working Group on NRT DORIS data,
Chair: Dettmering D., Member: Schmidt M.

International GNSS Service (IGS)

- Governing Board,
Network Representative: Sánchez L.
- Regional Network Associate Analysis Center for SIRGAS,
Chair: Sánchez L.
- Infrastructure Committee,
Member: Sánchez L.
- Working Group Reference Frame,
Member: Sánchez L.
- Ionosphere Working Group,
Member: Schmidt M.

International Service for the Geoid (ISG)

- *Scientific Advisor: Sánchez L.*

International Organization for Standardization (ISO)

- ISO/TC211,
IAG Representative to ISO/TC211: Angermann D.

International Space Science Institute (ISSI)

- Team Understanding the connection between coastal sea level and open ocean variability through space observations,
Member: Oelsmann J., Passaro M.

European Commission (EC) / European Space Agency (ESA)

- Copernicus POD Quality Working Group,
Member: Dettmering D.

European Space Agency (ESA)

- Copernicus New Generation Topography Constellation Ad-Hoc Expert Group,
Member: Passaro M.
- Copernicus Sentinel-3 Next Generation Topography Mission Advisory Group,
Member: Passaro M.
- CryoSat Expert Group,
Member: Passaro M.
- Coastal Altimetry Workshop Organizing Committee,
Member: Passaro M.

European Space Agency (ESA) / European Organisation for the Exploitation of Meteorological Satellites (EUMETSAT)

- Sentinel-3 Validation Team, Altimetry Sub-Group,
Member: Dettmering D.
- Sentinel-6 Validation Team,
Member: Dettmering D., Oelsmann J., Passaro M., Schlembach F., Schwatke C.

Centre National d'Etudes Spatiales (CNES) / National Aeronautics and Space Administration (NASA)

- Ocean Surface Topography Science Team,
Member: Dettmering D., Oelsmann J., Passaro M., Schlembach F., Schwatke C.
- SWOT Science Team,
Member: Dettmering D., Schwatke C.
- SWOT Science Team Working Group Global Hydrology and Remote Sensing,
Member: Schwatke C.
- SWOT Science Team Working Group River Science,
Member: Schwatke C.
- SWOT Science Team Working Group Science for Lakes and Wetlands,
Member: Schwatke C.

Sistema de Referencia Geocéntrico para las Américas (SIRGAS)

- Scientific Committee,
Member: Sánchez L.
- SIRGAS Analysis Center,
Chair: Sánchez L.

Forschungsgruppe Satellitengeodäsie (FGS)

- *Deputy Speaker: Seitz F.*
- Managing Board,
Member: Schmidt M., Seitz F.

Deutsche Gesellschaft für Polarforschung (DGP)

- Working Group Polar Geodesy and Glaciology,
Member: Müller F.

Deutsche Gesellschaft für Geodäsie, Geoinformation und Landmanagement (DVW)

- Working Group 7: Experimentelle, Angewandte und Theoretische Geodäsie,
Member: Schmidt M., Seitz F.

**Ausschuss Geodäsie der Bayerischen Akademie der Wissenschaften
(Deutsche Geodätische Kommission, DGK)**

- *Member: Seitz F.*

4.2 Publications

Angermann D., Pail R., Seitz F., Hugentobler U.: *Aardobservatie: Geodynamica en klimaatverandering beziën vanuit de ruimte*, New Scientist, ISBN 978-9-085-71780-5, 2022

Angermann D., Pail R., Seitz F., Hugentobler, U.: *Mission Earth: Geodynamics and Climate Change Observed Through Satellite Geodesy*, Springer, ISBN 978-3-662-64105-7, doi:[10.1007/978-3-662-64106-4](https://doi.org/10.1007/978-3-662-64106-4), 2022

Angermann D., Gruber T., Gerstl M., Heinkelmann R., Hugentobler U., Sánchez L., Steigenberger P., Gross R., Heki K., Marti U., Schuh H., Sehnal M., Thomas M.: *GGOS Bureau of Products and Standards: Description and Promotion of Geodetic Products*. In: Freymueller J., Sánchez L. (Eds.), IAG Symposia, Springer, doi:[10.1007/1345_2022_144](https://doi.org/10.1007/1345_2022_144), 2022

Barta V., Natras R., Srećković V., Koronczay D., Schmidt M., Šulic D.: *Multi-instrumental investigation of the solar flares impact on the ionosphere on 05–06 December 2006*. *Frontiers in Environmental Science*, 904335, doi:[10.3389/fenvs.2022.904335](https://doi.org/10.3389/fenvs.2022.904335), 2022

Cazenave A., Gouzenes Y., Birol, F., Leger F., Passaro M., Calafat F.M., Shaw A., Nino F., Legeais J.F., Oelmann J., Restano M., Benveniste J.: *Sea level along the world's coastlines can be measured by a network of virtual altimetry stations*. *Communications Earth and Environment (Nature Portfolio)*, 3(1), doi:[10.1038/s43247-022-00448-z](https://doi.org/10.1038/s43247-022-00448-z), 2022

Dettmering D., Schwatke C.: *Ionospheric corrections for satellite altimetry - impact on global mean sea level trends*. *Earth and Space Science*, 9, e2021EA002098, doi:[10.1029/2021EA002098](https://doi.org/10.1029/2021EA002098), 2022

- Ehlers F., Schlembach F., Kleinherenbrink M., Slobbe C.: *Validity assessment of SAMOSA retracking for fully-focused SAR altimeter waveforms*. *Advances in Space Research*, doi: [10.1016/j.asr.2022.11.034](https://doi.org/10.1016/j.asr.2022.11.034), 2022
- Escapa A., Heinkelmann R., Ferrándiz J.M., Seitz F., Gross R.: *Resolutions adopted in the IAU XXXI General Assembly Business Sessions proposed by Commission A2 on Rotation of the Earth*. *IAU Catalyst* March 2022, 18-22, 2022
- Fernandez-Gomez I., Kodikara T., Borries C., Forootan E., Goss A., Schmidt M., Codrescu M.: *Improving estimates of the ionosphere during geomagnetic storm conditions through assimilation of thermospheric mass density*. *Earth, Planets and Space*, 74(121), doi: [10.1186/s40623-022-01678-3](https://doi.org/10.1186/s40623-022-01678-3), 2022
- Glomsda M., Bloßfeld M., Seitz M., Angermann D., Seitz F.: *Comparison of non-tidal loading data for application in a secular terrestrial reference frame*. *Earth, Planets and Space*, 74(87), doi: [10.1186/s40623-022-01634-1](https://doi.org/10.1186/s40623-022-01634-1), 2022
- Gruber T., Ågren J., Angermann D., Ellmann A., Engfeldt A., Gisinger C., Jaworski L., Kur T., Marila S., Nastula J., Nilfouroushan F., Nordman M., Poutanen M., Saari T., Schlaak M., Świątek A., Varbla S., Zdunek R.: *Geodetic SAR for Height System Unification and Sea Level Research: Results in the Baltic Sea Test Network*. *Remote Sensing*, 14(14), 3250, doi: [10.3390/rs14143250](https://doi.org/10.3390/rs14143250), 2022
- Hart-Davis M.G., Dettmering D., Seitz F.: *TICON-3: Tidal Constants based on GESLA-3 sea-level records from globally distributed tide gauges including gauge type information (data)*. Deutsches Geodätisches Forschungsinstitut, Munich, doi: [10.1594/PANGAEA.951610](https://doi.org/10.1594/PANGAEA.951610), 2022
- Hart-Davis M.G., Sulzbach R., Dettmering D., Thomas M., Seitz F.: *TICON-td: Third-degree tidal constants based on GESLA sea-level records from globally distributed tide gauges (data)*. Deutsches Geodätisches Forschungsinstitut, Munich, doi: [10.1594/PANGAEA.943444](https://doi.org/10.1594/PANGAEA.943444), 2022
- Hellmers H., Modiri S., Bachmann S., Thaller D., Bloßfeld M., Seitz M., Gipson J.: *Combined IVS Contribution to the ITRF2020*. In: Freymueller J., Sánchez L. (Eds.), *IAG Symposia*, Springer, doi: [10.1007/1345_2022_170](https://doi.org/10.1007/1345_2022_170), 2022
- Hernández-Pajares M., Olivares-Pulido G., Graffigna V., García-Rigo A., Lyu H., Roma-Dollase D., Clara de Lacy M., Fernández-Prades C., Arribas J., Majoral M., Tisropoulos Z., Stamatelopoulos P., Symeonidou M., Schmidt M., Goss A., Erdogan E., van Evert F., Blok P., Grosso J., Spaltro E., Domínguez J., López E., Hriscu A.: *Wide-Area GNSS Corrections for Precise Positioning and Navigation in Agriculture*. *Remote Sensing*, 14(16), doi: [10.3390/rs14163845](https://doi.org/10.3390/rs14163845), 2022
- Heye S., Krug M., Penven P., Hart-Davis M.: *The Natal Bight Coastal Counter-Current: A modeling study*. *Continental Shelf Research*, 104852, doi: [10.1016/j.csr.2022.104852](https://doi.org/10.1016/j.csr.2022.104852), 2022
- Jerez G., Hernández-Pajares M., Goss A., da Silva C., Alves D., Monico J.: *Impact synergies of GIM error estimates on the VTEC interpolation and single-frequency PPP at low latitude region*. *GPS Solutions*, 26(2), doi: [10.1007/s10291-022-01228-0](https://doi.org/10.1007/s10291-022-01228-0), 2022
- Karimi A., Ghobadi-Far K., Passaro M.: *Barystatic and steric sea level variations in the Baltic Sea and implications of water exchange with the North Sea in the satellite era*. *Frontiers in Marine Science*, 9, doi: [10.3389/fmars.2022.963564](https://doi.org/10.3389/fmars.2022.963564), 2022
- Kehm A.: *Strategies for the Realisation of Geocentric Regional Epoch Reference Frames*. Bayerische Akademie der Wissenschaften, DGK C 894, Dissertation, 2022

- Kehm A., Sánchez L., Bloßfeld M., Seitz M., Drewes H., Angermann D., Seitz F.: *Combination Strategy for the Geocentric Realization of Regional Epoch Reference Frames*. Journal of Geophysical Research: Solid Earth, 127(10), doi:[10.1029/2021jb023880](https://doi.org/10.1029/2021jb023880), 2022
- Kwak Y., Glomsda M., Angermann D., Gerstl M.: *Comparison and integration of CONT17 networks*. Journal of Geodesy, 96(5), doi:[10.1007/s00190-022-01610-3](https://doi.org/10.1007/s00190-022-01610-3), 2022
- Lalgudi Gopalakrishnan G., Schmidt M.: *Ionospheric electron density modelling using B-splines and constraint optimization*. Earth, Planets and Space, 74(1), doi:[10.1186/s40623-022-01693-4](https://doi.org/10.1186/s40623-022-01693-4), 2022
- Liu Q.: *Regional gravity field refinement for geoid height modeling based on the combination of data from various observation techniques*. Bayerische Akademie der Wissenschaften, DGK C 896, Dissertation, 2022
- Liu Q., Schmidt M., Sánchez L.: *Combination of different observation types through a multi-resolution representation of the regional gravity field using the pyramid algorithm and parameter estimation*. Journal of Geodesy, 96(10), doi:[10.1007/s00190-022-01670-5](https://doi.org/10.1007/s00190-022-01670-5), 2022
- Natras R., Halilovic Dz., Mulic M., Schmidt M.: *Mid-latitude Ionosphere Variability (2013–2016), and Space Weather Impact on VTEC and Precise Point Positioning*. In: Ademović, N., et al. (Eds), *Advanced Technologies, Systems, and Applications VII.*, Lecture Notes in Networks and Systems, 539, doi:[10.1007/978-3-031-17697-5_37](https://doi.org/10.1007/978-3-031-17697-5_37), 2022
- Natras R., Soja B., Schmidt M.: *Machine Learning Ensemble Approach for Ionosphere and Space Weather Forecasting with Uncertainty Quantification*. 2022 3rd URSI Atlantic and Asia Pacific Radio Science Meeting (AT-AP-RASC), IEEE Xplore, doi:[10.23919/AT-AP-RASC54737.2022.9814334](https://doi.org/10.23919/AT-AP-RASC54737.2022.9814334), 2022
- Natras R., Soja B., Schmidt M.: *Ensemble Machine Learning of Random Forest, AdaBoost and XGBoost for Vertical Total Electron Content Forecasting*. Remote Sensing, 14(15), 3547, doi:[10.3390/rs14153547](https://doi.org/10.3390/rs14153547), 2022
- Oelsmann J., Passaro M., Sánchez L., Dettmering D., Schwatke C., Seitz F.: *Bayesian modelling of piecewise trends and discontinuities to improve the estimation of coastal vertical land motion*. Journal of Geodesy, 96(9), doi:[10.1007/s00190-022-01645-6](https://doi.org/10.1007/s00190-022-01645-6), 2022
- Passaro M., Rautiainen L., Dettmering D., Restano M., Hart-Davis M.G., Schlembach F., Särkkä J., Müller F. L., Schwatke C., Benveniste J.: *Validation of an Empirical Sub-waveform Retracking Strategy for SAR Altimetry*. Remote Sensing, 14(16), 4122, doi:[10.3390/rs14164122](https://doi.org/10.3390/rs14164122), 2022
- Pfaff M.C., Hart-Davis M., Smith M. E., Veitch J.: *A new model-based coastal retention index (CORE) identifies bays as hotspots of retention, biological production and cumulative anthropogenic pressures*. Estuarine, Coastal and Shelf Science, 107909, doi:[10.1016/j.ecss.2022.107909](https://doi.org/10.1016/j.ecss.2022.107909), 2022
- Scherer D., Schwatke C., Dettmering D., Seitz F. : *ICESat-2 Based River Surface Slope and Its Impact on Water Level Time Series From Satellite Altimetry*. Water Resources Research, 58(11), doi:[10.1029/2022WR032842](https://doi.org/10.1029/2022WR032842), 2022
- Scherer D., Schwatke C., Dettmering D., Seitz F. : *IRIS: ICESat-2 River Surface Slope (data)*. Zenodo, doi:[10.5281/zenodo.7098113](https://doi.org/10.5281/zenodo.7098113), 2022
- Schlembach F., Passaro M., Dettmering D., Bidlot J., Seitz F.: *Interference-sensitive coastal SAR altimetry retracking strategy for measuring significant wave height*. Remote Sensing of Environment, 274, 112968, doi:[10.1016/j.rse.2022.112968](https://doi.org/10.1016/j.rse.2022.112968), 2022

Seitz M., Bloßfeld M., Angermann D., Seitz F.: *DTRF2014: DGFI-TUM's ITRS realization 2014*. *Advances in Space Research*, 69(6), 2391-2420, doi:[10.1016/j.asr.2021.12.037](https://doi.org/10.1016/j.asr.2021.12.037), 2022

Sulzbach R., Wziontek H., Hart-Davis M.G., Dobslaw H., Scherneck H.-G., Van Camp M., Omang O.C.D., Antokoletz E. D., Voigt C., Dettmering D., Thomas M.: *Modeling gravimetric signatures of third-degree ocean tides and their detection in superconducting gravimeter records*. *Journal of Geodesy*, 96(5), doi:[10.1007/s00190-022-01609-w](https://doi.org/10.1007/s00190-022-01609-w), 2022

Sánchez L.: *SIRGAS Regional Network Associate Analysis Centre Technical Report 2021*. IGS Technical Report 2021, 129-141, doi:[10.48350/169536](https://doi.org/10.48350/169536), 2022

Sánchez L., Drewes H., Kehm A., Seitz M.: *SIRGAS reference frame analysis at DGFI-TUM*. *Journal of Geodetic Science*, 12(1), 92–119, doi:[10.1515/jogs-2022-0138](https://doi.org/10.1515/jogs-2022-0138), 2022

4.3 Presentations

Aldarias A., Passaro M., Gomez-Enri J., Mulero-Martinez R., Laiz I., Ehlers F., Schlembach F., Scagliola M.: *Analysis of Fully Focused and unfocused SAR data in the 0-5 km of the coastal strip*. OSTST Meeting 2022, Venice, Italy, 2022

Aldarias A., Passaro M., Gómez-Enri J., Mulero-Martínez R., Laiz I., Ehlers F., Schlembach F., Scagliola M.: *Accuracy and precision assessment of Sentinel-3 Fully-Focused SAR in the Gulf of Cadiz (Spain). Benefits for oceanographic applications.* ESA Living Planet Symposium 2022, Bonn, Germany, 2022

Angermann D.: *Geodäsie und Geoinformation*. Unitag, Technische Universität München, Munich, Germany, 2022

Angermann D.: *FGS-Beiträge zu IAG und GGOS*. FGS Review of the Research and Development Programme 2021-2025, Bad Kötzing, Germany, 2022

Angermann D., Gruber T., Gerstl M., Heinkelmann R., Hugentobler U., Sanchez L., Steigenberger P., Heki K., Schuh H., Sehnal M.: *GGOS Bureau of Products and Standards: Description and promotion of geodetic products*. EGU General Assembly 2022, Vienna, Austria, 2022

Angermann D., Gruber T., Gerstl M., Heinkelmann R., Hugentobler U., Sánchez L., Steigenberger P.: *GGOS Bureau of Products and Standards*. GGOS Japan Meeting, online, 2022

Angermann D., Gruber T., Gerstl M., Heinkelmann R., Hugentobler U., Sánchez L., Steigenberger P.: *Report GGOS Bureau of Products and Standards*. GGOS Days 2022, Munich, Germany, 2022

Angermann D., Gruber T., Gerstl M., Heinkelmann R., Hugentobler U., Sánchez L., Steigenberger P.: *GGOS Bureau of Products and Standards (BPS): BPS Activities on Standards*. Unified Analysis Workshop 2022, Thessaloniki, Greece, 2022

Barta V., Natras R., Sreckovic V., Koronczay D., Schmidt M., Sulic D.: *Multi-instrumental investigation of the solar flares impact on the ionosphere on 05-06 December 2006*. 8th IAGA/ICMA/SCOSTEP Workshop on Vertical Coupling in the Atmosphere-Ionosphere System, Sopron, Hungary, 2022

Barta V., Natras R., Sreckovic V., Koronczay D., Schmidt M., Sulic D.: *Multi-instrumental investigation of the solar flares impact on the ionosphere on 05–06 December 2006*. 18th European Space Weather Week (ESWW2022), Zagreb, Croatia, 2022 (Poster)

- Barta V., Natras R., Sreckovic V., Koronczay D., Schmidt M., Sulic D.: *Multi-instrumental investigation of the solar flares impact on the ionosphere occurring in December 2006*. EGU General Assembly 2022, Vienna, Austria, 2022
- Benveniste J., Cotton D., Garcia-Mondejar A., ...Passaro M., Dettmering D., ...Restano M.: *Improving SAR Altimeter Processing over Inland Water - the ESA HYDROCOASTAL Project*. EGU General Assembly 2022, Vienna, Austria, 2022
- Benveniste J., Cotton D., Garcia-Mondejar A., ...Passaro M., Dettmering D., ...Restano M.: *SAR Altimetry Processing Over the Coastal Zone and Inland Water - the ESA HYDROCOASTAL Project*. IAHS-AISH Scientific Assembly 2022, Montpellier, France, 2022
- Benveniste J., Dinardo S., Buchhaupt C., Scagliola M., Passaro M., Fenoglio-Marc L., Sabatino G., Restano M., Abis B., Ambrozio A., Orru C.: *SAR, SARin, RDSAR and FF-SAR Altimetry Processing on Demand for Cryosat-2 and Sentinel-3 at ESA's Altimetry Virtual Lab*. ESA Living Planet Symposium 2022, Bonn, Germany, 2022 (Poster)
- Benveniste J., Dinardo S., Buchhaupt C., Scagliola M., Passaro M., Fenoglio-Marc L., Sabatino G., Restano M., Ambrozio A., Orru C.: *SAR, SARin, RDSAR and FF-SAR Altimetry Processing on Demand for CryoSat-2, Sentinel-3 and Sentinel-6 at ESA's Altimetry Virtual Lab*. OSTST Meeting 2022, Venice, Italy, 2022 (Poster)
- Birkett G., Hermes J., Veitch J., Hart-Davis M.: *Nurdle Spill Scenarios: Using A Numerical Model To Identify High Risk Coastal Regions*. Southern African Marine Science Symposium (SAMSS), online, 2022
- Bloßfeld M., Neidhardt A., Seitz F.: *P7: The application of time in closure as a novel strategy towards error-free space geodetic observations*. DFG review of Research Unit 5456 Clock Metrology: A Novel Approach to TIME in Geodesy, Bad Kötzing, Germany, 2022
- Bloßfeld M., Rudenko S.: *DGFI-TUM ITRF2020P analysis*. ILRS Analysis Standing Committee meeting, online, 2022
- Bloßfeld M., Seitz M., Glomsda M., Angermann D., Rudenko S., Zeitlhöfler J., Seitz F.: *DTRF2020 - the ITRS 2020 realization of DGFI-TUM*. FGS Review of the Research and Development Programme 2021-2025, Bad Kötzing, Germany, 2022
- Bloßfeld M.: *DGFI-TUM ILRS AC report*. ILRS Analysis Standing Committee meeting, Guadalajara, Spain, 2022
- Cazenave A., Gouzenes Y., Birol, F., Passaro M., Calafat F.M., Leger F., Shaw A., Nino F., Legeais J.F., Benveniste J.: *A new network of altimetry-based virtual stations for measuring sea level along the world coastlines*. OSTST Meeting 2022, Venice, Italy, 2022
- Costa S.M.A., Sánchez L., Piñon D., Tarrío-Mosquera J.A., Guimarães G., Gómez D., Drewes H., et al.: *Status of the SIRGAS reference frame: Recent developments and new challenges*. IAG Reference Frames for Applications in Geosciences Symposium (REFAG2022), Thessaloniki, Greece, 2022
- Cotton P.D., Garcia-Mondejar A., ...Passaro M., Dettmering D., ..., Benveniste J., Restano M.: *Improving SAR Altimeter processing over the coastal zone - the ESA HYDROCOASTAL project*. EGU General Assembly 2022, Vienna, Austria, 2022
- Dettmering D., Schwatke C.: *Long-term stability of ionospheric GIM corrections in satellite altimetry data sets*. OSTST Meeting 2022, Venice, Italy, 2022

- Dodet G., Quilfen Y., Quartly G., Passaro M., Schlembach F., Timmermans B., Accensi M., Arduin F.: *Improved inter-calibration of multi-mission altimeter significant wave heights for climate data record*. OSTST Meeting 2022, Venice, Italy, 2022 (Poster)
- Gille S., Soares S., Chereskin T., Passaro M.: *Coastal-to-open ocean exchange in the California Current System from new altimetry*. OSTST Meeting 2022, Venice, Italy, 2022 (Poster)
- Glomsda M., Seitz M., Angermann D.: *Comparison of simultaneous VGOS and legacy VLBI sessions*. 12th IVS General Meeting, 2022
- Glomsda M., Seitz M., Bloßfeld M., Angermann D. : *Effects of non-tidal loading applied in VLBI reference frames*. IAG Reference Frames for Applications in Geosciences Symposium (REFAG2022), Thessaloniki, Greece, 2022
- González-Haro C., Passaro M., Müller F. L., Oelsmann J., González-Gambau V., Olmedo E., García-Espriu A., Turiel A., Fernández Prieto D., Sabia R., Restano M., Benveniste J.: *Exploring synergies between remote sensing products developed under the framework of ESA Baltic+ initiative: Sea Surface Salinity and Sea Level*. ESA Living Planet Symposium 2022, Bonn, Germany, 2022 (Poster)
- Halicki M., Schwatke C., Niedzielski T.: *The influence of the satellite ground track shift on the accuracy of altimetric measurements on rivers: A case study of the Sentinel-3 altimetry on the Middle Odra River*. Geoinformacja: Nauka - Praktyka - Edukacja, Poznań, Poland, 2022
- Hart-Davis M.: *The importance of ocean tides in sea level research using satellite altimetry*. Deltares Team Hydrodynamics Meeting, The Netherlands, 2022
- Hart-Davis M.: *Studies in Cross-Disciplinary Research using Parcels in the Greater Agulhas System*. Utrecht University Parcels Team Meeting, The Netherlands, 2022
- Hart-Davis M., Dettmering D., Schwatke C., Passaro M., Seitz F. : *EOT20: Improvements made to ocean tide estimations from coastal altimetry*. ESA Living Planet Symposium 2022, Bonn, Germany, 2022 (Poster)
- Hart-Davis M., Sulzbach R., Dettmering D., Thomas M., Schwatke C., Seitz F. : *The assessment of minor tidal constituents in ocean models for optimising the ocean tidal correction*. EGU General Assembly 2022, Vienna, Austria, 2022
- Hart-Davis M.G. : *Turtles: Effects of swimming behaviour and oceanography on sea turtle hatchling dispersal*. Copernicus Biodiversity in Coastal Ecosystems Workshop, online, 2022
- Hart-Davis M.G.: *Coastal Altimetry at DGFI-TUM and Applications in Ocean Tide Modelling*. Nansen-Tutu Workshop, Cape Town, South Africa (online), 2022
- Hart-Davis M.G.: *Regional and Global Ocean Tide Modelling*. Nansen Environmental Remote Sensing Center (NERSC) Seminar, online, 2022
- Hart-Davis M.G.: *Regional EOT developments for improved tidal estimation of major and minor tidal constituents*. Workshop Ocean Dynamics and Global Geodesy, online, 2022
- Hart-Davis M.G., Backeberg B., Johannessen J.A., van Sebille E., Dettmering D.: *Towards understanding surface convergence and divergence processes in the Agulhas Current and its Return by combining data from a surface drifter-pair and World Ocean Circulation data*. World Ocean Circulation User Consultation Meeting, ESA/ESRIN, Frascati, Italy, 2022 (Poster)
- Hart-Davis M.G., Dettmering D., Schwatke C., Passaro M., Seitz F.: *Insights from the global EOT20 ocean tide model*. OSTST Meeting 2022, Venice, Italy, 2022

- Heye S., Krug M., Penven P., Hart-Davis M., Rouault M.: *Kwazulu-Natal Bight Surface Circulation and Its Impact On Marine Protected Area Connectivity*. Southern African Marine Science Symposium (SAMSS), online, 2022
- Juhl M.-C., Passaro M., Dettmering D., Saraceno M.: *Wind as driver of sub-annual sea level anomalies on South Brazil and Patagonian Shelf*. OSTST Meeting 2022, Venice, Italy, 2022
- Krypiak-Gregorczyk A., Milanowska B., Schmidt M., Goss A., Erdogan E., Jarmołowski W., Wielgosz P.: *Comparative analysis of new pre-operational global ionosphere models from UWM and DGFI-TUM*. International Workshop on GNSS Ionosphere (IWGI2022), Neustrelitz, Germany, 2022
- Le Gouvello D., Heye S., Gaspar P., Hart-Davis M., Louro C., Harris L., Nel R.: *Dispersal corridors of neonate turtles in the South Western Indian Ocean*. Western Indian Ocean Marine Science Association (WIOMSA) 12th Scientific Symposium, online, 2022
- Le Henaff M., Kersale M., Meinen C., Perez R., Birol F., Passaro M., Schwatke C., Chidichimo C., Valla D., Piola A., Lamont T., Ansorge A., Speich S.: *Using coastal altimetry to improve Meridional Overturning Circulation estimates in the South Atlantic*. OSTST Meeting 2022, Venice, Italy, 2022
- Le N., Männel B., Natras R., Sakic P., Deng Z., Schuh H.: *Apply noise filters for better forecast performance in Machine Learning*. EGU General Assembly 2022, Vienna, Austria, 2022
- Marcos M., Haigh I.D., Talke S.A., Hart-Davis M., Dettmering D., Woodworth P.L., Hunter J.R. : *The new GESLA-3 tide gauge data set and its quality control for tidal studies*. EGU General Assembly 2022, Vienna, Austria, 2022
- Müller F. L., Paul S., Dettmering D., Hendricks S.: *Monitoring Arctic thin ice: A comparison between Cryosat-2 SAR altimetry data and MODIS thermal-infrared imagery*. ESA Living Planet Symposium 2022, Bonn, Germany, 2022 (Poster)
- Müller F. L., Paul S., Dettmering D., Hendricks S.: *A comparison between Cryosat-2 radar altimetry and MODIS imagery for monitoring thin ice in the Laptev Sea*. 28. Internationale Polartagung 2022, Potsdam, Germany, 2022
- Natras R., Halilovic Dz., Mulic M., Schmidt M.: *Mid-latitude Ionosphere Variability and Modeling including Space Weather Impact on VTEC and PPP*. 13th Annual Days of BHAAAS in Bosnia and Herzegovina, online, 2022
- Natras R., Soja B., Schmidt M.: *Uncertainty Quantification for Ionosphere Forecasting with Machine Learning*. International Workshop on GNSS Ionosphere (IWGI2022), Neustrelitz, Germany, 2022
- Natras R., Soja B., Schmidt M.: *Interpretable Machine Learning for Ionosphere Forecasting with Uncertainty Quantification*. 1st Workshop on Data Science for GNSS Remote Sensing, Potsdam, Germany, 2022
- Natras R., Soja B., Schmidt M.: *Machine Learning Ensemble Approach for Ionosphere and Space Weather Forecasting with Uncertainty Quantification*. 3rd URSI Atlantic / Asia-Pacific Radio Science Conference, Gran Canaria, Spain, 2022
- Natras R., Soja B., Schmidt M., Dominique M., Türkmen A.: *Machine Learning Approach for Forecasting Space Weather Effects in the Ionosphere with Uncertainty Quantification*. EGU General Assembly 2022, Vienna, Austria, 2022

- Oelmann J., Marcos M., Passaro M., Sanchez L., Dettmering D., Seitz F.: *Vertical land motion reconstruction unveils nonlinear effects on relative sea level*. WCRP Sea Level Conference, Singapore, 2022
- Oelmann J., Marcos M., Passaro M., Sanchez L., Dettmering D., Seitz F.: *The impact of continuous space and time-resolving vertical land motion on relative sea level change*. EGU General Assembly 2022, Vienna, Austria, 2022
- Passaro M., Hemer M.A., Quartly G.D., Schwatke C., Dettmering D., Seitz F.: *Global coastal attenuation of wind-waves observed with radar altimetry*. Oceans From Space Symposium 2022, Venice, 2022
- Passaro M., Müller F., Abulaitijang A., Andersen O.B., Chalençon E., Dettmering D., Hart-Davis M., Hoyer J.L., Oelmann J., Ruatiainen L., Ringgaard I.M., Särkkä J., Scarrott R., Schwatke C., Skovgaard Madsen K., Tuomi L., Restano M., Benveniste J.: *Baltic SEAL: new insights into the mean and variability of the sea level in the Satellite Altimetry era*. OSTST Meeting 2022, Venice, Italy, 2022 (Poster)
- Passaro M., Müller F.L., Abulaitijang A., Andersen O.B., Chalençon E., Dettmering D., Hart-Davis M., Hoyer J.L., Oelmann J., Ruatiainen L., Ringgaard I.M., Särkkä J., Scarrott R., Schwatke C., Seitz F., Skovgaard Madsen K., Tuomi L., Restano M., Benveniste J.: *Baltic SEAL: new insights into the mean and variability of the sea level in the Satellite Altimetry era*. ESA Living Planet Symposium 2022, Bonn, Germany, 2022 (Poster)
- Rudenko S., Bloßfeld M., Kehm A., Dettmering D., Zeitlhöfler J., Glomsda M., Angermann D., Seitz M.: *Precise orbit determination of SLR and altimetry satellites using ITRS2020 realizations*. 22nd International Workshop on Laser Ranging, Guadalajara, Spain, 2022
- Rudenko S., Bloßfeld M., Zeitlhöfler J.: *Recent activities on orbit determination for altimetry satellites at DGFI-TUM*. IDS Analysis Working Group Meeting, online, 2022
- Rudenko S., Bloßfeld M., Zeitlhöfler J., Kehm A., Dettmering D., Glomsda M., Angermann D., Seitz M.: *Application of the ITRS2020 realizations for precise orbit determination of SLR and altimetry satellites*. IAG Reference Frames for Applications in Geosciences Symposium (REFAG2022), Thessaloniki, Greece, 2022
- Rudenko S., Dettmering D., Bloßfeld M., Zeitlhöfler J., Alkahal R.: *On the accuracy of contemporary orbits of altimetry satellites in the radial direction*. OSTST Meeting 2022, Venice, Italy, 2022
- Scagliola M., Altiparmaki O., Bercher N., Fenoglio-Marc L., Nielsen K., Passaro M., Restano M., Abis B., Fornari M., Sabatino G. and Benveniste J.: *The Aresys FF-SAR Service for Cryosat-2 at ESA's Altimetry Virtual Lab*. ESA Living Planet Symposium 2022, Bonn, Germany, 2022 (Poster)
- Scherer D., Schwatke C., Dettmering D.: *Estimating Water Surface Slope of Rivers Using ICESat-2 Observations*. EGU General Assembly 2022, Vienna, Austria, 2022
- Schlembach F., Ehlers F., Kleinherenbrink M., Passaro M., Slobbe C.: *Coastal Case Study for Leveraging the Potential of Sentinel-6 MF FF-SAR Altimetry for Significant Wave Height*. OSTST Meeting 2022, Venice, Italy, 2022
- Schlembach F., Passaro M.: *RAW versus RMC: A Coastal Study*. Sentinel-6 Validation Team Meeting 4, 2022

- Schlembach F., Passaro M., Dettmering D., Bidlot J., Seitz F.: *Interference-sensitive Coastal SAR Altimetry Retracker for Measuring Significant Wave Height*. ESA Living Planet Symposium 2022, Bonn, Germany, 2022
- Schmidt M.: *Combination of space-geodetic observation techniques for ionosphere modeling and space weather research*. 13th Annual Days of BHAAAS in Bosnia and Herzegovina, online, 2022
- Schmidt M.: *Echtzeit-Monitoring und Prädiktion der Ionosphäre*. FGS Review of the Research and Development Programme 2021-2025, Bad Kötzing, Germany, 2022
- Schmidt M., Forootan E.: *GGOS Focus Area on Geodetic Space Weather Research: objectives and structure*. 2nd Symposium of IAG Commission 4 Positioning and Applications, Potsdam, Germany, 2022
- Schmidt M., Zeitler L., Corbin A., Vielberg K., Rudenko S., Löcher A., Bloßfeld M., Kusche J.: *A comparison of scale factors for the thermospheric density from Satellite Laser Ranging and accelerometer measurements to LEO satellites*. EGU General Assembly 2022, Vienna, Austria, 2022
- Schmidt M., Zeitler L., Zeithöfler J., Corbin A., Vielberg K., Rudenko S., Bloßfeld M., Löcher A., Kusche J.: *A comparison of scale factors for the thermospheric density from satellite laser ranging and accelerometer measurements*. SPP 1788 Dynamic Earth Final Colloquium, Kühlungsborn, Germany, 2022 (Poster)
- Schmidt M., Zeithöfler J., Zeitler L., Corbin A., Kusche J., Stolle C., Xiong C., Hugentobler U., Bamann C., Rudenko S., Bloßfeld M., Vielberg K., Löcher A.: *Development of high-precision thermosphere models for improving precise orbit determination of Low-Earth-Orbiting satellites (TIPOD) Status Report*. SPP 1788 Dynamic Earth Final Colloquium, Kühlungsborn, Germany, 2022 (Poster)
- Schmidt M., Zeithöfler J., Zeitler L., Corbin A., Vielberg K., Löcher A., Rudenko S., Bloßfeld M., Kusche J.: *A comparison of scale factors for the thermospheric density derived from Satellite Laser Ranging and Accelerometer Measurements to LEO satellites*. 2nd Symposium of IAG Commission 4 Positioning and Applications, Potsdam, Germany, 2022
- Schwatke C.: *EUROLAS Data Center (EDC) – Status Report 2018-2022*. 22nd International Workshop on Laser Ranging, Guadalajara, Spain, 2022 (Poster)
- Schwatke C., Ricklefs R.: *Data Formats and Procedures Standing Committee - Status Report*. ILRS Governing Board Meeting, Guadalajara, Spain, 2022
- Schwatke C., Scherer D., Dettmering D.: *DAHITI - How can satellite-derived hydrological products for monitoring the global water cycle benefit from SWOT?*. SWOT Working Group River Science, online, 2022
- Schwatke C., Scherer D., Dettmering D.: *DAHITI - Deriving hydrological products for inland waters using remote sensing and future integration of SWOT data*. SWOT Science Team Meeting, Chapel Hill, USA and Toulouse, France, 2022
- Schwatke C., Scherer D., Dettmering D.: *DAHITI - How can satellite-derived storage changes for lakes and reservoirs benefit from SWOT?*. SWOT Working Group Global Hydrology, online, 2022
- Schwatke C., Scherer D., Dettmering D.: *DAHITI - Next generation of water level time series of inland waters*. ESA Living Planet Symposium 2022, Bonn, Germany, 2022 (Poster)

- Seitz F.: *Precise positioning, geo-referencing observations, and the quantification of climate change: The International Reference System and the key role of the Geodetic Observatory Wettzell*. 50th Anniversary of the Geodetic Observatory Wettzell, Germany, 2022
- Seitz F.: *FGS Schwerpunkt 3: Produkte, Anwendungen, Internationale Zusammenarbeit*. FGS Review of the Research and Development Programme 2021-2025, Bad Kötzing, Germany, 2022
- Seitz M., Angermann D., Bloßfeld M., Glomsda M., Rudenko S., Zeitlhöfler J.: *DTRF2020: the ITRS 2020 realization of DGFI-TUM*. IAG Reference Frames for Applications in Geosciences Symposium (REFAG2022), Thessaloniki, Greece, 2022
- Seitz M., Angermann D., Bloßfeld M., Glomsda M., Rudenko S., Zeitlhöfler J.: *DTRF2020: first results*. Unified Analysis Workshop 2022, Thessaloniki, Greece, 2022
- Seitz M., Angermann D., Bloßfeld M., Glomsda M., Rudenko S., Zeitlhöfler J.: *DTRF2020: the ITRS 2020 realization of DGFI-TUM*. IDS Workshop, Venice, Italy, 2022
- Seitz M., Angermann D., Bloßfeld M., Glomsda M., Rudenko S., Zeitlhöfler J., Seitz F.: *DTRF2020: the ITRS 2020 realization of DGFI-TUM*. Frontiers of Geodetic Science (FroGS), Essen, Germany, 2022
- Seitz M., Angermann D., Glomsda M., Bloßfeld M., Rudenko S., Zeitlhöfler J.: *The ITRS 2020 realization of DGFI-TUM: DTRF2020*. EGU General Assembly 2022, Vienna, Austria, 2022
- Seitz M., Bloßfeld M., Glomsda M., Angermann D., Rudenko S., Zeitlhöfler J., Seitz F.: *DTRF2020: the ITRS 2020 realization of DGFI-TUM*. 22nd International Workshop on Laser Ranging, Guadalajara, Spain, 2022
- Seitz M., Bloßfeld M., Glomsda M., Angermann D., Rudenko S., Zeitlhöfler J., Seitz F.: *DTRF2020: the ITRS 2020 realization of DGFI-TUM*. AGU Fall Meeting 2022, Chicago, USA
- Seitz M., Glaser S.: *P9: Novel clock technologies for combination on ground and in space: real data and simulation*. DFG review of Research Unit 5456 Clock Metrology: A Novel Approach to TIME in Geodesy, Bad Kötzing, Germany, 2022
- Sulzbach R., Mayer-Gurr T., Dobslaw H., Dahle C., Öhlinge F., Balidakis K., Hart-Davis M., Dettmering D.: *Proposition for updated conventions for the gravity potential induced by ocean tides*. COST-G meeting, 2022
- Sánchez L.: *International Height Reference System: Definition, Realisation, Status*. SIRGAS Workshop on Physical Heights and Gravity, online, 2022
- Sánchez L.: *Importance of the incorporation of SIRGAS stations into the global network of the International GNSS Service (IGS)*. SIRGAS Workshop on Geodetic Reference Stations, online, 2022
- Sánchez L.: *International Height Reference System*. Webinar Unified Height System, Santiago de Chile, Chile, 2022
- Sánchez L., Barzaghi R.: *Report of the GGOS Focus Area Unified Height System*. GGOS Coordinating Board Meeting, online, 2022
- Sánchez L., Barzaghi R.: *Reference Systems and Frames in Physical Geodesy*. Unified Analysis Workshop 2022, Thessaloniki, Greece, 2022

- Sánchez L., Drewes H., Kehm A., Seitz M.: *SIRGAS2022: Reference frame solution based on the homogeneous reprocessing of the SIRGAS historical data since January 2000*. Symposium SIRGAS2022, Santiago de Chile, Chile, 2022
- Sánchez L., Huang J., Barzaghi R., Vergos G.S.: *Towards an international standard for the precise determination of physical heights*. EGU General Assembly 2022, Vienna, Austria, 2022
- Sánchez L., Huang J., Barzaghi R., Vergos G.S., Ågren J., Mäkinen J., Véronneau M., et al.: *Status of the International Height Reference Frame*. GGHS2022: Gravity, Geoid, and Height Systems 2022 Symposium, Austin, USA, 2022
- Sánchez L., Huang J., Barzaghi R., Vergos G., Ågren J., Mäkinen J., Véronneau M., et al.: *Advances in the determination of a global unified reference frame for physical heights*. IAG Reference Frames for Applications in Geosciences Symposium (REFAG2022), Thessaloniki, Greece, 2022
- Sánchez L., Kehm A., Drewes H., Seitz M.: *SIRGAS Reference Frame Analysis at DGFI-TUM*. Symposium SIRGAS2022, Santiago de Chile, Chile, 2022
- Veng T., Müller F. L., Dettmering D., Seitz F., Andersen O.: *Detecting Arctic sea ice openings with Cryosat-2 InSAR observations as a basis for improved ocean surface circulation monitoring*. ESA Living Planet Symposium 2022, Bonn, Germany, 2022 (Poster)
- Wang N., Liu A., Dettmering D., Li Z., Schmidt M.: *Using Near-Real-Time DORIS Data for Validating Real-Time GNSS Ionospheric Maps*. IDS Workshop 2022, Venice, Italy, 2022
- Wang N., Liu A., Dettmering D., Li Z., Schmidt M.: *Using DORIS Data for Validating Real-Time GNSS Ionospheric Maps*. International Workshop on GNSS Ionosphere (IWGI2022), Neustrelitz, Germany, 2022
- Wang N., Liu A., Dettmering D., Li Z., Schmidt M.: *Using Near-Real-Time DORIS Data for Validating Real-Time GNSS Ionospheric Maps*. 2nd Symposium of IAG Commission 4 Positioning and Applications, Potsdam, Germany, 2022
- Woo J., Schwatke C., Blevins S., B.P. Michael: *ILRS Data Centers: Overview, Current Status, and Future Work*. 22nd International Workshop on Laser Ranging, 2022 (Poster)
- Wziontek H., Sulzbach R., Hart-Davis M., Dobsław H., Scherneck H., Van Camp M., Omang O., Antokoletz E., Voigt C., Dettmering D., Thomas M.: *Data-Unconstrained Modeling and Detection of 9 Individual Partial Ocean Tides of Third-Degree by Terrestrial Gravimetry*. EGU General Assembly 2022, Vienna, Austria, 2022
- Zeithöfler J., Bloßfeld M.: *A comparison of different ocean tides models*. 22nd International Workshop on Laser Ranging, Guadalajara, Spain, 2022
- Zeithöfler J., Bloßfeld M., Rudenko S., Dettmering D., Seitz F.: *Station-dependent satellite laser ranging measurement corrections for TOPEX/Poseidon*. Frontiers of Geodetic Science (FroGS), Essen, Germany, 2022
- Zeithöfler J., Bloßfeld M., Rudenko S., Dettmering D., Seitz F.: *Station-dependent satellite laser ranging measurement corrections for TOPEX/Poseidon*. 22nd International Workshop on Laser Ranging, Guadalajara, Spain and online, 2022
- Zeithöfler J., Schmidt M., Liu S.: *Development of an empirical thermospheric density model to improve the precise orbit determination of low-Earth-orbiting satellites*. Frontiers of Geodetic Science (FroGS), Essen, Germany, 2022

4.4 Participation in Meetings, Symposia, Conferences

- 2022-01-18 : **ESA HYDROCOASTAL progress meeting 6, online**
Dettmering D.
- 2022-01-27 : **SWOT Working Group River Science, online**
Scherer D., Schwatke C.
- 2022-01-28 : **ESA Sea Level Climate Change Initiative progress meeting, online**
Passaro M., Oelsmann J.
- 2022-02-15/16 : **IAG Second Earth Orientation Parameters Prediction Comparison Campaign (2nd EOP PCC) Workshop, online**
Kehm A.
- 2022-03-01/02 : **GlobalCDA status meeting, Potsdam, Germany**
Dettmering D., Scherer D., Schwatke C.
- 2022-03-02/03 : **GlobalCDA ECR gender equality workshop on 'Work-Life-Balance and Resilience', Potsdam, Germany**
Scherer D.
- 2022-03-03/04 : **Sentinel-3 Next Generation Topography MAG, online**
Passaro M.
- 2022-03-03/04 : **NERO GRAV status meeting, online**
Dettmering D., Hart-Davis M.
- 2022-03-04 : **EGU Campfire Geodesy, online**
Passaro M.
- 2022-03-07/10 : **ISSI meeting 'Understanding the Connection Between Coastal Sea Level and Open Ocean Variability Through Space Observations', Bern, Switzerland**
Passaro M., Oelsmann J.
- 2022-03-08 : **OSTST Mini-POD splinter meeting, online**
Rudenko S.
- 2022-03-15 : **Spring meeting of DGK Section Geodesy, online**
Seitz F.
- 2022-03-17 : **FGS Board meeting, online**
Schmidt M., Seitz F.
- 2022-03-21/22 : **Ocean Surface Topography Science Team (OSTST) Meeting, online**
Dettmering D., Rudenko S.
- 2022-03-22/25 : **4th IVS VLBI Training School, online**
Glomsda M.
- 2022-03-23/24 : **Retreat of the TUM SoED Department Aerospace and Geodesy, Hohenkammer, Germany**
Seitz F.

- 2022-03-28/04-01 : **12th IVS General Meeting, online**
Glomsda M.
- 2022-03-31 : **SWOT Working Group River Science, online**
Scherer D., Schwatke C.
- 2022-04-07 : **ESA HYDROCOASTAL Inland Water Initial Validation Results review meeting, online**
Dettmering D., Scherer D.
- 2022-04-14 : **ILRS Governing Board meeting, online**
Schwatke C.
- 2022-04-20/21 : **ESA HYDROCOASTAL Mid Term Review, Barcelona, Spain**
Dettmering D., Passaro M., Scherer D.
- 2022-04-26 : **SWOT Working Group Global Hydrology, online**
Schwatke C.
- 2022-05-01/05 : **28. Internationale Polartagung 2022, Potsdam, Germany**
Müller F.L.
- 2022-05-19 : **SWOT Working Group River Science, online**
Scherer D., Schwatke C.
- 2022-05-19 : **ILRS Networks and Engineering Standing Committee meeting, online**
Schwatke C.
- 2022-05-19/20 : **DFG Round table discussion ‘GGOS-DACH’, Munich, Germany**
Angermann D., Bloßfeld D., Seitz F.
- 2022-05-23/27 : **ESA Living Planet Symposium, Bonn, Germany**
Müller F. L., Schlembach F., Schwatke C.
- 2022-05-23/27 : **EGU General Assembly 2022, Vienna, Austria**
Angermann D., Bloßfeld M., Hart-Davis M., Natras R., Oelsmann J., Rudenko S., Sánchez L., Scherer D., Schmidt M., Seitz F., Seitz M.
- 2022-05-29/06-03 : **URSI Atlantic/Asia-Pacific Radio Sci. Meeting, Gran Canaria, Spain**
Natras R.
- 2022-05-31/06-02 : **SPP 1788 Dynamic Earth, final colloquium, Kühlungsborn, Germany**
Schmidt M., Zeitlhöfler J.
- 2022-06-01 : **ESA S6-JTEX progress meeting 3, online**
Dettmering D., Passaro M., Schlembach F.
- 2022-06-09 : **ESA Sea State Climate Change Initiative final meeting, online**
Passaro M.
- 2022-06-09/10 : **NFDI4Earth 1st plenary meeting, Dresden, Germany**
Seitz F.
- 2022-06-13/15 : **1st Workshop on Data Science for GNSS Remote Sensing, Potsdam, Germany**
Natras R.

- 2022-06-14 : **IDS Analysis Working Group meeting, online**
Rudenko S., Zeithöfler J.
- 2022-06-20 : **IAG Inter-Commission Committee on Geodesy on Theory (ICCT) Joint Study Group T.29 Machine Learning in Geodesy, 3rd meeting, online**
Natras R.
- 2022-06-20 : **ESA HYDROCOASTAL Inland Water Product Validation Review, online**
Dettmering D., Scherer D.
- 2022-06-24 : **13th Annual Days of BHAAAS in Bosnia and Herzegovina, Sarajevo**
Natras R., Schmidt M.
- 2022-06-27/30 : **SWOT Science Team meeting, Chapel Hill, USA and Toulouse, France**
Dettmering D., Hart-Davis M., Scherer D., Schwatke C.
- 2022-07-01/05 : **Sentinel-3 New Generation Preliminary Concept Review, ESA/ESTEC, The Netherlands**
Passaro M.
- 2022-07-08 : **IDS Government Board meeting, online**
Dettmering D.
- 2022-07-11 : **ESA HYDROCOASTAL progress meeting 7, online**
Dettmering D., Scherer D.
- 2022-07-11/13 : **Sentinel-6 Validation Team meeting 4, online**
Dettmering D., Schlembach F., Schwatke C.
- 2022-09-05/08 : **IAG Commission 4 Symposium, Potsdam, Germany**
Schmidt M.
- 2022-09-19/21 : **D-A-CH meeting of DGK, ÖGK, SGK, Innsbruck, Austria**
Seitz F.
- 2022-09-26/28 : **International Workshop on GNSS Ionosphere (IWGI2022), Neustrelitz, Germany**
Schmidt M., Natras R.
- 2022-09-27 : **DFG review of Research Unit 5456 Clock Metrology: A Novel Approach to TIME in Geodesy, Bad Kötzing, Germany**
Bloßfeld M., Seitz M.
- 2022-10-04 : **Sentinel-3 Next Generation Topography MAG, online**
Passaro M.
- 2022-10-06 : **50th anniversary of the Geodetic Observatory Wettzell, Germany**
Angermann D., Bloßfeld M., Seitz F., Seitz M.
- 2022-10-06 : **ESA Sea Level Climate Change Initiative+, Phase 2 kick off, online**
Oelsmann J., Passaro M.
- 2022-10-06/07 : **GlobalCDA status meeting, Bonn, Germany**
Dettmering D., Schwatke C.
- 2022-10-10/12 : **World Ocean Circulation User Consultation 2022, Frascati, Italy (online)**
Hart-Davis M.G.

- 2022-10-11 : **ESA S6-JTEX progress meeting 4, online**
Schlembach F., Passaro M., Dettmering D.
- 2022-10-11/12 : **Copernicus Biodiversity in Coastal Ecosystems, online**
Hart-Davis M.G.
- 2022-10-12/14 : **FGS Review of the Research and Development Programme 2021-2025, Bad Kötzing, Germany**
Angermann D., Bloßfeld M., Dettmering D., Schmidt M., Seitz F.
- 2022-10-17/20 : **IAG International Symposium on Reference Frames for Applications in Geosciences (REFAG 2022), Thessaloniki, Greece**
Angermann D., Glomsda M., Rudenko S., Sánchez L.
- 2022-10-18/20 : **Sentinel-3 Validation Team meeting 7, online**
Dettmering D.
- 2022-10-19/20 : **Frontiers of Geodetic Science, Essen, Germany**
Seitz F., Bloßfeld M., Zeitlhöfler J.
- 2022-10-21/23 : **IERS/GGOS Unified Analysis Workshop (UAW) 2022, Thessaloniki, Greece**
Angermann D., Glomsda M., Sánchez L., Seitz M.
- 2022-10-24/28 : **Oceans From Space Symposium, Venice, Italy**
Passaro M.
- 2022-10-31/11-01 : **IDS workshop, Venice, Italy**
Dettmering D., Rudenko S.
- 2022-10-31/11-04 : **Ocean Surface Topography Science Team (OSTST) Meeting 2022, Venice, Italy**
Hart-Davis M.G., Dettmering D., Rudenko S., Schlembach F., Juhl M.C.
- 2022-11-02 : **IDS Governing Board meeting, Venice, Italy**
Dettmering D.
- 2022-11-06 : **ILRS Governing Board meeting, Guadalajara, Spain**
Bloßfeld M., Schwatke C.
- 2022-11-06 : **ILRS Analysis Standing Committee meeting, Guadalajara, Spain**
Bloßfeld M., Schwatke C.
- 2022-11-06/11 : **International Workshop on Laser Ranging, Guadalajara, Spain**
Bloßfeld M., Schwatke C., Zeitlhöfler J., Rudenko S.
- 2022-11-07 : **ILRS Data Formats & Procedures Standing Committee meeting, Guadalajara, Spain**
Bloßfeld M., Schwatke C.
- 2022-11-10 : **SWOT Science Virtual Town Hall, online**
Dettmering D.
- 2022-11-14/15 : **GGOS Days 2022, Munich, Germany**
Angermann D., Sanchez L., Schmidt M., Seitz F., Seitz M., Rudenko S., Kehm A., Müller F.

- 2022-11-15 : **Nansen-Tutu Center workshop, Cape Town, South Africa (online)**
Hart-Davis M.G.
- 2022-11-17/18 : **Ocean Dynamics and Global Geodesy Workshop, Potsdam, Germany**
Hart-Davis M.G.
- 2022-11-21 : **Autumn meeting of DGK Section Geodesy, online**
Seitz F.
- 2022-11-25/26 : **100 years Astronomical Institute of the University of Bern (AIUB), Switzerland**
Seitz F., Seitz M.
- 2022-12-07 : **ESA HYDROCOASTAL progress meeting 9, online**
Dettmering D.
- 2022-12-12/16 : **AGU Fall Meeting, Chicago, USA**
Bloßfeld M.

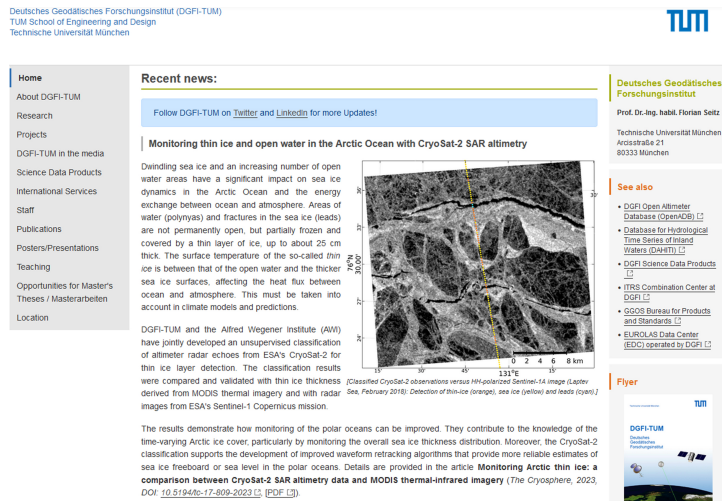
4.5 Guests

- 2022-01-01/12-31 : Dr. Stephan Paul, AWI, Bremerhaven, Germany
- 2022-01-25 : Prof. Dr. Andreas Güntner, Section Hydrology, German Research Centre for Geosciences (GFZ), Potsdam, Germany
- 2022-03-24/12-31 : Dr. Yuliia Semenova, Institute of Geophysics, National Academy of Sciences of Ukraine
- 2022-04-25/29 : Roman Sulzbach, Section Earth System Modelling, German Research Center for Geosciences (GFZ), Potsdam, Germany
- 2022-05-30/31 : Prof. Dr. Martin Saraceno, Department of Marine and Atmospheric Sciences, Universidad de Buenos Aires, Argentina
- 2022-06-03/09-26 : Michal Halicki, Department of Geoinformatics and Cartography, University of Wroclaw, Poland
- 2022-06-13/15 : Dr. Ernst Lexen, German Space Situational Awareness Centre (GSSAC), Uedem, Germany

4.6 Internet Portals

For the exchange of scientific knowledge, results and data with national and international partners, interested parties and the public, DGFI-TUM maintains the following internet portals and public databases:

Deutsches Geodätisches Forschungsinstitut der Technischen Universität München (DGFI-TUM)



The DGFI-TUM website at www.dgfi.tum.de highlights the latest research results and provides information on the structure and research of the institute. It presents the national and international projects as well as the institute's involvement in various international scientific organizations. The website contains complete lists of publications, reports and presentations since 1994 and provides the scientific data products of DGFI-TUM. It has a media section and presents information on teaching.



For contact with the public, the scientific community and students, DGFI-TUM is represented on social media channels. Among others, on Twitter (twitter.com/dgfitum), Facebook (facebook.com/dgfitum), and LinkedIn (linkedin.com/company/dgfi-tum), current results, job offers, and opportunities for scientific work are published. Posts are met with considerable response and reach several hundred followers.

Open Altimeter Database (OpenADB): Ocean science data from space

OpenADB (openadb.dgfi.tum.de) is the DGFI-TUM platform for the dissemination of multi-mission altimetry data and derived high-level science products of oceanic and atmospheric quantities. It serves scientists across disciplines as well as users in research and practice. OpenADB data are widely used for the study of ocean and climate processes, for monitoring purposes, or for the creation and validation of new products, models, and algorithms.

Currently, OpenADB provides the following data:

- Sea Surface Heights (SSH)
- Sea Level Anomalies (SLA)
- Adaptive Leading Edge Subwaveform (ALES) Retracker heights
- Instantaneous Dynamic Ocean Topography Profiles (iDOT)
- Empirical Ocean Tide Model (EOT)
- Vertical Total Electron Content (VTEC)

All altimetry data are provided free of charge to registered users in standard data formats. The data in OpenADB are preprocessed and already corrected with the latest geophysical models. In addition, data from all missions have been carefully harmonized and cross-calibrated so that observation data from different missions can be combined and analyzed jointly.

Open Altimeter Database (OpenADB)
Deutsches Geodätisches Forschungsinstitut
Technische Universität München




OpenADB

- Products +
- Mean Sea Level +
- Missions +
- Pass Locator +
- Documentation +
- Data Access

OpenADB

Open Altimeter Database (OpenADB)



WELCOME TO OPENADB ...

OpenADB is a database for satellite altimetry data and derived high-level products. It shall serve users with little experience in satellite altimetry and scientific users evaluating data, generating new products, models and algorithms.

The following products are available via OpenADB:

- Sea Surface Heights (SSH)
- Sea Level Anomalies (SLA)
- Instantaneous Dynamic Ocean Topography Profiles (iDOT)
- Empirical Ocean Tide Model (EOT)
- Vertical Total Electron Content (VTEC)
- Adaptive Leading Edge Subwaveform (ALES) Retracker

All products are provided along-track in a sequential data structure following the usual hierarchy mission-cycle-pass with cycles identifying (in general) a repeat period after which the ground track pattern repeats itself and passes are decomposed into ascending and descending portions of the ground track.

Contact

Christian Schwatke
christian.schwatke@tum.de

80333 München
Arcisstr.21
Tel. +49 89 23031-1109
Fax +49 89 23031-1240

Database for Hydrological Time Series of Inland Waters (DAHITI)

DAHITI (dahiti.dgfi.tum.de) is the DGFI-TUM database for satellite-based hydrological parameters. In 2022, a new milestone was reached with now 10,000 distributed virtual monitoring stations at lakes, reservoirs, rivers and wetlands. For all of these targets, DAHITI provides water level time series from multi-mission satellite altimetry.

In addition, time series of surface water extent (based on Landsat and Sentinel-2 optical imagery), inferred bathymetry, and water occurrence masks are available for a number of lakes and reservoirs. Changes in water storage (volume changes) from a combination of satellite altimetry and optical imagery are also provided. In 2022, DGFI-TUM expanded the availability of river discharge time series (Section 2.3). With several thousand registered users and more than two hundred thousand downloads in recent years, DAHITI is a widely used data source for numerous applications in science and practice. The Global Climate Observing System (GCOS) lists the database as an openly accessible data source for the Essential Climate Variable (ECV) 'Lakes'. To date, DAHITI provides water level and water extent for more than 1400 lakes and reservoirs, continuously and automatically updated with the latest satellite information.

EUROLAS Data Center (EDC)

The EUROLAS Data Center (EDC) is, along with NASA's CDDIS, one of two global Data Centers of the International Laser Ranging Service (ILRS). The EDC has been operated by DGFI-TUM since 1998. The website edc.dgfi.tum.de provides the ILRS community with access to all SLR original observations and derived results. In addition, the EDC website provides information about real-time data management in the ILRS Operations Center (OC) at EDC and about the Data Center's data holding.

GGOS Focus Area Unified Height System

DGFI-TUM has chaired the GGOS Focus Area *Unified Height System* since 2015. Its main objective is the implementation of a global vertical reference system in accordance with the International Association of Geodesy (IAG) Resolution No. 1, 2015 for the definition and realization of an International Height Reference System (IHR). The Focus Area website (ihrs.dgfi.tum.de), maintained by DGFI-TUM, summarizes the actions, plans, and recent achievements, and provides an inventory of work documents, relevant publications, and presentations.

Geocentric Reference System for the Americas (SIRGAS)

DGFI-TUM has been involved in SIRGAS research activities since the establishment of SIRGAS in 1993. The institute coordinated the 1995 and 2000 SIRGAS GPS campaigns and acted as an analysis center for both campaigns, contributing to the final solutions SIRGAS95 and SIRGAS2000. In June 1996, DGFI-TUM, in agreement with the International GNSS Service (IGS), established the IGS Regional Network Associate Analysis Center for SIRGAS (IGS RNAAC SIRGAS) and assumed responsibility for the weekly processing of the continuously operating SIRGAS network. This also includes the computation of cumulative (multi-year) solutions and surface velocity models (known as VEMOS) to monitor the kinematics of the SIRGAS reference frame. Since 2008, DGFI-TUM has focused on the computation of the SIRGAS core network and on the combination of this network with the solutions provided by the Latin American data centers for national SIRGAS densification. DGFI-TUM also plays a central role in the determination of SIRGAS reference frame multi-year solutions and surface deformation models. DGFI-TUM's SIRGAS website www.sirgas.org presents analysis strategies, research results and data products generated by DGFI-TUM as SIRGAS Processing and Combination Center and as IGS RNAAC SIRGAS.

SIRGAS Analysis Centre at DGFI-TUM
Deutsches Geodätisches Forschungsinstitut
Technische Universität München



- Home
- About SIRGAS
- Realizations +
- Stations +
- Data processing
- Data combination +
- Weekly solutions +
- Multi-year solutions
- VEMOS velocity model +
- Publications
- Presentations
- Updates

Contact

Dr.-Ing. Laura Sanchez

lm.sanchez@tum.de

80333 München
Arcisstr.21
Tel. +49 89 23031-1295
Fax +49 89 23031-1240

SIRGAS Analysis Centre at DGFI-TUM

The **Deutsches Geodätisches Forschungsinstitut der Technische Universität München (DGFI-TUM)** has been involved in the SIRGAS research activities since the establishment of SIRGAS in 1993. DGFI-TUM coordinated the SIRGAS GPS campaigns of 1995 and 2000 and acted as an analysis centre of both campaigns contributing to the final solutions known as **SIRGAS95** and **SIRGAS2000**. In June 1996, DGFI-TUM established in agreement with the International GNSS Service (IGS) the **IGS Regional Network Associate Analysis Centre for SIRGAS (IGS RNAAC SIRGAS)** and assumed the responsibility of processing the **SIRGAS continuously operating network** in a weekly basis. This responsibility also includes the computation of **cumulative (multi-year) solutions** and **surface velocity models for SIRGAS** (known as VEMOS) to monitor the kinematics of the SIRGAS reference frame. Since 2008, with the creation of different SIRGAS analysis centres under the responsibility of Latin American agencies, DGFI-TUM concentrates on the computation of the SIRGAS core network and on the combination of this network with the solutions delivered by the Latin American analysis centres for the SIRGAS national densifications. The computation of multi-year solutions and surface deformation models continues being a main contribution of DGFI-TUM to SIRGAS.

5 Projects

A large part of DGFI-TUM's research activities is financed through third-party funds from various sources. Funding of the following projects is gratefully acknowledged (in alphabetic order):

- AROCCIE** Arctic Ocean surface circulation in a changing climate and its possible impact on Europe (IGSSE)
- CIEROT** Combination of space geodetic observations for the determination of mass transports in the cryosphere and their impact on Earth rotation (DFG)
- CIRCOS** Circulation from In-situ and Remote Sensing Data in Coastal and Shelf Ocean (DFG)
- CPOD** Copernicus Sentinels Precise Orbit Determination (ESA)
- FOR 2630, ARISAS** Advances in remote sensing of inland waters by satellite altimetry with special focus on SWOT (DFG)
- FOR 2630, WALESA** Refined estimates of absolute water levels for inland waters from multi-mission satellite altimetry (DFG)
- FOR 2736, TIDUS** Improved tidal dynamics and uncertainty estimation for satellite gravimetry (DFG)
- FOR 2736, TIDUS-2** Improved tidal dynamics and uncertainty estimation for satellite gravimetry (DFG)
- Geo-H** Enhanced geopotential field modelling as basis for the establishment of precise height systems (DFG)
- Hydrocoastal** Sentinel-3 and Cryosat SAR/SARIn radar altimetry for coastal zone and inland waters (ESA)
- MEPODAS** Mitigation of the current errors in precise orbit determination of altimetry satellites (DFG)
- ML-IonoCast** Machine learning for forecasting the ionospheric total electron content (DAAD)
- PSD-ITRS** Analysis, approximation and interpretation of post-seismic deformations determined at GNSS observing stations for the improvement of the ITRS realisation (TUM Institute of Advanced Study, IAS)
- S6-JTEX** Sentinel-6 Michael Freilich and Jason-3 tandem flight exploitation (ESA)
- SPP 1788, MuSE** Multi-satellite reconstruction of the electron density in ionosphere and plasmasphere (DFG)
- SPP 1788, TIPOD** Development of high-precision thermosphere models for improving precise orbit determination of Low-Earth-Orbiting satellites (DFG)
- SL-CCI Plus** Sea Level Climate Change Initiative Plus (ESA)
- SS-CCI Plus** Sea State Climate Change Initiative Plus (ESA)
- VLAD** Vertical land motion by satellite altimetry and tide gauge difference (DFG)

6 Personnel

6.1 Lectures and Courses at Universities

- Angermann D.:** Lecture ‘Satellite Geodesy: Global Geodata for Society and Politics’,
TUM, SS 2022
- Bloßfeld M.:** Lecture ‘Realization and Application of Global Geodetic Reference Systems’,
TUM, SS 2022
- Bloßfeld M.:** Lecture ‘Geokinematics’,
TUM, WS 2021/22 and WS 2022/23
- Dettmering D.:** Lecture ‘Hydrogeodesy: Monitoring Surface Waters from Space’,
TUM, WS 2021/22 and WS 2022/23
- Passaro M.:** Lecture ‘Satellite Altimetry and Physical Oceanography’,
TUM, WS 2021/22 and WS 2022/23
- Passaro M.:** Lecture ‘Numerical Modeling’,
TUM, WS 2021/22
- Sánchez L.:** Lecture ‘Advanced Aspects of Height Systems’,
TUM, WS 2021/22 and WS 2022/23
- Schmidt M.:** Lecture ‘Numerical Modeling’,
TUM, WS 2022/23
- Schmidt M.:** Lecture ‘Numerical Methods in Satellite Geodesy’,
TUM, SS 2022
- Schmidt M.:** Lecture ‘Ionosphere Monitoring and Modeling’,
TUM, WS 2021/22 and WS 2022/23
- Schmidt M., Seitz F., Müller F., Glomsda M.:** Lecture ‘Numerical Methods’,
TUM, WS 2021/22 and WS 2022/23
- Seitz F.:** Lecture ‘Seminar ESPACE’,
TUM, SS 2022
- Seitz F.:** Lecture ‘Earth Rotation’,
TUM, WS 2021/22 and WS 2022/23
- Seitz F.:** Lecture ‘Satellite Geodesy for Earth System Applications’,
TUM, WS 2022/23
- Seitz F.:** Lecture ‘Climate Change and Agriculture’,
TUM, WS 2021/22 and WS 2022/23
- Seitz F.:** Lecture ‘Introduction to Geodesy and Geoinformation’,
TUM, WS 2022/23
- Seitz F.:** Seminar for Doctoral Candidates at DGFI-TUM,
TUM, WS 2021/22, SS 2022 and WS 2022/23

6.2 Academic Program Coordination and Study Advice

- Müller F.:** Master and Bachelor programmes ‘Geodesy and Geoinformation’

6.3 Lectures at Seminars, Schools, and Public Relations

Oelsmann J.: 'Coastal relative sea level changes from altimetry, tide gauge and GNSS observations'. National Oceanography Centre, Southampton, England, 2022-04-19

Natras R.: 'Investigation of PROBA2 LYRA data for predicting the Vertical Total Electron Content (VTEC) of the ionosphere with machine learning'. Solar-Terrestrial Center of Excellence (STCE) Seminar, Royal Observatory of Belgium, Brussels, 2022-05-05

Seitz F.: 'The International Reference System and the key role of the Geodetic Observatory Wettzell'. 50th Anniversary of the Geodetic Observatory Wettzell, Germany, 2022-10-06

Angermann D.: 'Geodäsie und Geoinformation'. Unitag, Technische Universität München, Germany, 2022-10-28

6.4 Thesis Supervision

Bachelor theses

Müller F., Seitz F.: Thesis Kistler C., TUM: Verwendung von ICESat-2 Laser-Altmetrie zur Bestimmung des Meeresspiegels im Arktischen Ozean. 2022-07-11

Master theses

Schlembach F., Seitz F.: Thesis Falkenstein A., TUM: Detecting extreme sea states in satellite altimetry data. 2022-02-11

Bloßfeld M., Seitz F.: Thesis Heinze K., TUM: SLR long-term mean range biases for LEO satellites. 2022-03-30

Schmidt M., Zeitlhöfler J.: Thesis Liu S., TUM: Transformation of global thermospheric density grids from the NRLMSISE-00 model into a multi-dimensional B-spline representation. 2022-10-11

Schmidt M.: Thesis Qiu F., TUM: Estimation of electron density key parameters using the multi-layer Chapman Model considering inequality constraints from ionospheric radio occultation measurements. 2022-10-19

Dettmering D., Schwatke C., Seitz F.: Thesis Kumar D., TUM: Inland water levels from Sentinel-6: How can SAR altimetry improve the height estimation of rivers and lakes? 2022-12-14

Doctoral theses

Schmidt M. (supervisor): Thesis Liu Q., TUM: Regional gravity field refinement for geoid height modeling based on the combination of data from various observation techniques. 2022-11-16

Seitz F. (supervisor): Thesis Kehm A., TUM: Strategies for the realisation of geocentric regional Epoch Reference Frames. 2022-11-18

Schmidt M. (supervisor): Thesis Lalgudi Gopalakrishnan G., TUM: Ionosphere electron density modelling using a constrained optimization approach. 2022-12-19

Habilitation

Seitz F. (supervisor): Habilitation Passaro M., TUM: Improvement of the global precision of sea level and sea state estimates from radar altimetry. 2022-04-07

6.5 Conferral of Doctorates

Liu Q.: Regional gravity field refinement for geoid height modeling based on the combination of data from various observation techniques.

Supervisors: Prof. Dr.-Ing. M. Schmidt (TUM), Prof. Dr.techn. R. Pail (TUM), Prof. Dr.-Ing. A. Eicker (HafenCity Universität Hamburg, Germany).

Day of defense: 2022-11-16

Institution: TUM

Kehm A.: Strategies for the realisation of geocentric regional Epoch Reference Frames.

Supervisors: Prof. Dr.-Ing. F. Seitz (TUM), Prof. Dr. U. Hugentobler (TUM), Dr. R. Gross (Jet Propulsion Laboratory/California Institute of Technology (Caltech), USA),

Day of defense: 2022-11-18

Institution: TUM

Lalgudi Gopalakrishnan G.: Ionosphere electron density modelling using a constrained optimization approach.

Supervisors: Prof. Dr.-Ing. M. Schmidt (TUM), Prof. Dr. U. Hugentobler (TUM), Prof. Dr. M. Hernández-Pajares (Universitat Politècnica de Catalunya, Spain).

Day of defense: 2022-12-19

Institution: TUM

6.6 Conferral of Venia Legendi

Passaro M.: Improvement of the global precision of sea level and sea state estimates from radar altimetry.

Supervisors: Prof. Dr.-Ing. F. Seitz (TUM), Prof. Dr. J. Gómez-Enri (Universidad de Cádiz, Spain), Prof. Dr. I. Haigh (University of Southampton, United Kingdom).

Institution: TUM

6.7 International Research Stays

Hart-Davis M.: Deltares: Hydrodynamics and Forecasting department, Netherlands

Duration: 2022-05-29 until 2022-07-09

Supervisors: Prof. Dr. Martin Verlaan, Dr. Björn Backeberg

Natras R.: Royal Observatory of Belgium (ROB), Brussels, Belgium

Duration: 2022-04-20/05-06 and 2022-11-07/18

Supervisor: Dr. Marie Dominique

Natras R.: Universitat Politècnica de Catalunya, Spain

Duration: 2022-09-01/10-31

Supervisor: Prof. Dr. Manuel Hernández-Pajares

6.8 Awards

Natras R.: *Young Scientist Award,*

International Union of Radio Science (URSI), Commission G 'Ionospheric Radio and Propagation'

Oelsmann J.: *Outstanding Student and PhD candidate Presentation (OSPP) Award,*

European Geosciences Union (EGU), Division 'Climate: Past, Present and Future'